CHAPTER 4

The Effectiveness of Steel Reinforcing Netting As Reinforcement for Hot-Mix Asphalt

4.1 ABSTRACT

This chapter investigates the effectiveness of steel reinforcing netting for use in the hot-mix asphalt (HMA) layers of new flexible pavement systems. For this study, two sections of the Virginia Smart Road were instrumented and constructed incorporating three different types of steel reinforcement. Detailed documentation of the interlayer system installation is presented, with recommendations about improving and facilitating future installations. Evaluation of steel reinforcement effectiveness was investigated, based on Falling Weight Deflectometer (FWD) deflection measurements. Instrument responses to vehicular loading, combined with finite element (FE) modeling, were used to evaluate the effectiveness of steel reinforcement in enhancing flexible pavement performance and resisting pavement distresses, such as fatigue cracking at the bottom of the HMA layers. Results of this study indicated that installation of the interlayer system was successful and that previous installation difficulties appear to have been solved. The reinforcing mesh can be affixed to the supporting layer using either of two approaches: nailing or slurry sealing. In general, based on reviewed literature and the experience developed as a result of this project, applying an intermediate slurry seal layer has proven more reliable than nailing. Additionally, FWD testing results and finite element simulations suggest that for the considered pavement structures, the contribution of steel reinforcement to the surface vertical deflections is minimal. However, FWD testing could be used to evaluate the contribution of steel reinforcement to weak pavement structures. To simulate the pavement designs in Virginia Smart Road sections I and L, finite element models were successfully developed. After these models were calibrated

based on instrument responses to vehicular loading, a comparison was established between reinforced and unreinforced cases. In Section L, the fatigue performance of the considered pavement structure improved between 6 and 55% in the transverse direction, and between 25 and 82% in the longitudinal direction. In Section I, the range of improvement for the pavement structure was between 15 and 257% in the transverse direction, and between 12 and 261% in the longitudinal direction. It is important to emphasize that because steel reinforcement was used in two different pavement designs and different locations in the pavement system, no comparison was established between the two types of steel reinforcement. The contribution of steel reinforcement to the structure is believed to be of the utmost importance after crack initiation.

4.2 INTRODUCTION

In pavement systems, the term *reinforcement* refers to the ability of an interlayer to better distribute the applied load over a larger area and to compensate for the lack of tensile strength within structural materials. As with any reinforcement applications, the interlayer should be stiffer than the material to be strengthened (Rigo 1993). In such pavement applications, reinforcements involving either (1) subgrade and granular layers or (2) HMA layers and overlays have achieved particular success.

To increase HMA's resistance to cracking and rutting, interest has recently grown in repeating the very successful example of steel-reinforced Portland cement concrete (PCC). Since both HMA and PCC are strong in compression but weak in tension, reinforcement should provide needed resistance to tensile stresses. Although a similar contributing mechanism may be expected in both applications, clear differences should be recognized, such as the viscoelastic nature of HMA, the multi-layer system analysis of flexible pavements, and mechanisms for carrying the load.

Some design practices suggest that the use of reinforcing interlayer systems provides substantial savings in HMA thickness, increases the number of load repetitions to failure, or reduces permanent deformation in flexible pavement systems (Kennepohl et al. 1985). Unfortunately, because several of the proposed design practices have been introduced by the industry and are not supported by theoretical explanation, they rely primarily on empirical and arbitrary rules—in other words, chance. This fact has led to the reporting of contradictory results or experiences, which in turn has escalated doubt among pavement agencies as to the actual benefits proffered by such materials. The idea that interlayer systems will result in better long-term pavement performance presents too simple a view of a very complex situation.

Therefore, the key objective of this chapter is to investigate how effectively steel reinforcing nettings can be used to enhance pavement performance. While being successfully evaluated in several projects in Europe, especially Belgium, such a technique has never been studied on any roads or bridges in the United States prior to its installation at the Virginia Smart Road pavement test facility. Detailed monitoring of the

installation procedure was, therefore, essential for discovering construction difficulties that could impact future projects.

4.3 STEEL REINFORCEMENT

One of the oldest interface systems used in flexible pavement is steel reinforcement. The technique, which appeared in the early 1950s, was abandoned in the early 1970s after tremendous installation difficulties were encountered. Based on a field evaluation in Toronto, after five years of service, steel-reinforcement had significantly reduced the appearance of reflection cracking (Brownridge et al. 1964). Conclusions from other field evaluations, such as Tons et al (1960), confirmed these findings: "The cost of a 75 mm reinforced overlay was no greater than a 95 mm unreinforced overlay. However, the 95 mm unreinforced has a transverse crack incidence five times greater than the 75-mm reinforced." Appendix A provides more details on earlier experiences with welded wire.

Twenty years later, the technique reappeared in Europe but used a new class of steel reinforcement products. In this case, many of the earlier problems associated with the product appeared to have been solved, and satisfactory experiences with the new class of steel reinforcement were reported (Vanelstraete and Francken 2000). Steel mesh is now coated for protection against corrosion, and the product configuration and geometry have been redesigned. In addition, its installation techniques have been modified. Table 4-1 illustrates a general comparison between the original steel mesh and the new product.

Configuration of the current steel mesh product consists of a double-twist, hexagonal mesh with variable dimensions, which is transversally reinforced at regular intervals with steel wires (either circular or torsioned flat-shaped) inserted in the double twist, as shown in Figures 4-1(a) and (b). No welding is used in the new generation of steel reinforcement.

Table 4-1. Comparison between the Original Wire Mesh and the Current Steel Mesh

Criterion	Original Mesh (1950-1970)	New Mesh (1980-2000)
Product	Welded wire	Coated woven wire mesh
Product Shape	Rectangular	Hexagonal
Sensitivity to Rust	Yes	No
Installation	Rigid	Allows horizontal movement
Unrolling Process	Manually	Using a roller
Creeping of the Mesh	Installed loose	Wire tension may be relieved during construction
Fixation	Hog rings	Nails or other pertinent method (slurry seal)
Cost ($/m^2)*	0.20-0.70	3.5-6.0

* No inflation rate was used

(a)

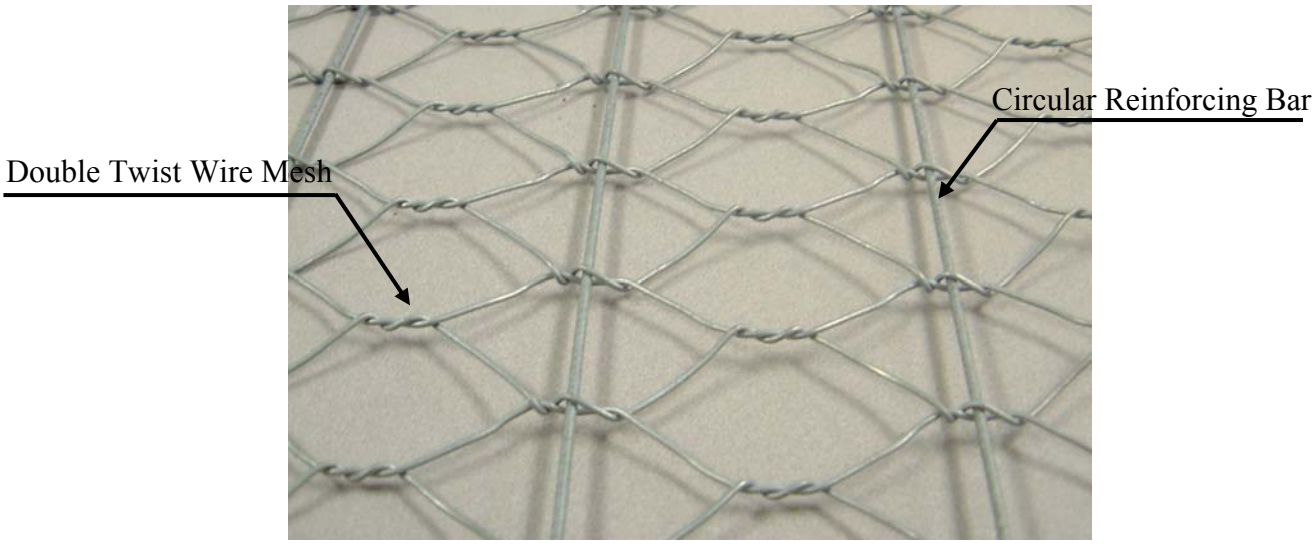

(b)

Figure 4-1. General Configuration of Two Types of Steel Reinforcement Nettings

4.4 STEEL REINFORCEMENT INSTALLATION

The installation process for steel mesh greatly affects its reinforcement effectiveness. For successful installation, the mesh should be laid perfectly flat, and any folds or wrinkles should be avoided. A loader or a pneumatic compactor can be driven on top of the mesh to remove any existing tension, as well as reduce the natural curvature of the roll. The mesh can then be fixed easily by nails and/or an appropriate intermediate layer (e.g. slurry seals).

When a slurry seal is used, the imprint of the mesh should be visible through it; in other words, a thinner slurry layer is better than a thicker one, which might cause "bleeding" of the seal. An application rate of 17 kg/m² of polymer-modified slurry seal is usually recommended. Other than avoiding folds or wrinkles during installation, steel mesh does not need any stretching or tensioning operations; however, one of the installation techniques suggests pretensioning, a technique used successfully in a project in Atlanta, GA (2002). Beyond these requirements, traffic may run on the slurry seal-mesh interlayer at a maximum speed of 40 km/hr.

The first installation of the new class of steel reinforcement in the US was at the Virginia Smart Road. Installation was carefully monitored to ensure that previous difficulties had been solved. At the Virginia Smart Road, three types of steel reinforcement were installed in two different sections (see Table 4-2):

- **Section I**: Two types of steel reinforcement were installed underneath 100mm of base mix (BM-25.0).
- **Section L**: A third type of steel reinforcement was installed underneath 150-mm-thick BM-25.0 HMA base, followed by a 38-mm stone-matrix asphalt (SMA-12.5) layer.

Table 4-2. Specifications of the Steel Reinforcement Installed at the Virginia Smart Road

Designation	Mesh 1 (L)	Mesh 2 (S)	Mesh 3 (III)
Section at the Virginia Smart Road	I	I (Instrumented)	L
Wire Diameter (mm)	2.40	2.70	2.45
Corrosion Resistance Coating	Zinc	Zinc	Bezinal Coating (Zn + Al)
Reinforcing Wire Dimensions (mm)	$\phi = 4.40$	$\phi = 4.90$	7 x 3.00
Longitudinal Tensile Strength (kN/m)	40	40	40
Transverse Tensile Strength (kN/m)	50	50	50
Modulus of Elasticity (kN/mm^2)	200	200	200

4.4.1 Section I

In Section I, steel reinforcing netting was installed on top of the SM-9.5A layer and below the BM-25.0 layer (see Figure 4-2). Instrumentation and construction of this section was completed in mid-November 1999. A detailed description of instrument specifications and calibrations is included in Appendix A.

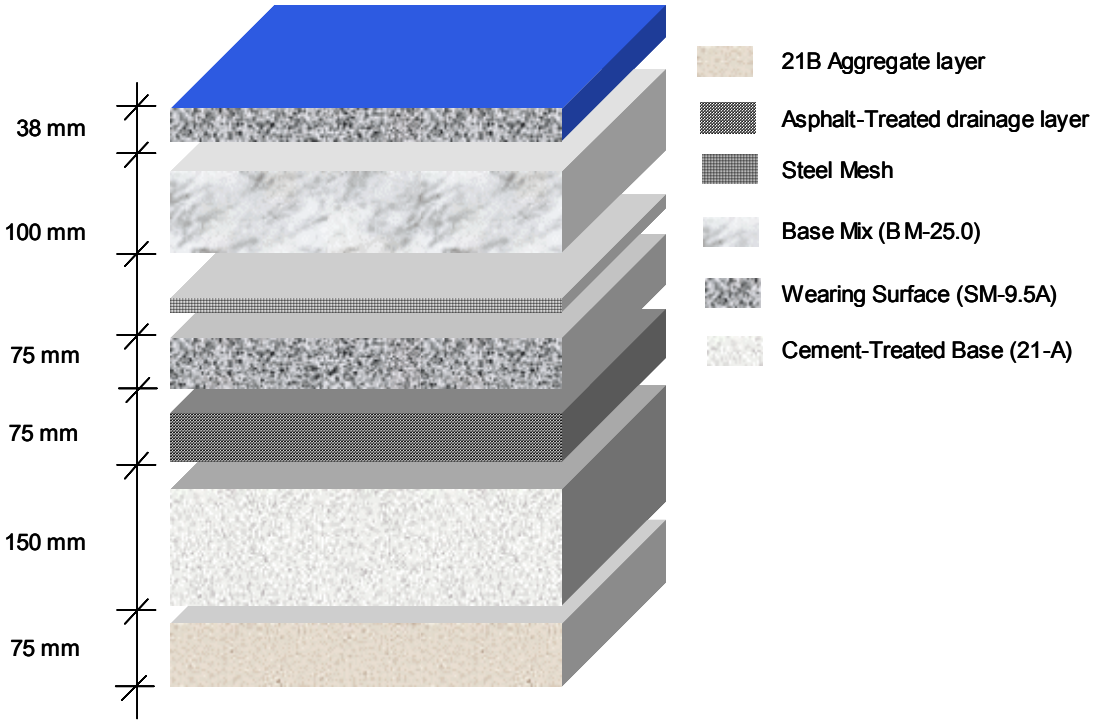

Figure 4-2. Pavement Design in Section I

The day of the steel mesh installation in Section I (Friday September 24th 1999) was sunny, with an average temperature of 24°C. Prior to the steel reinforcement installation, the instruments were installed in pre-dug ditches under 100mm of BM-25.0. Wires beneath the mesh also ran along these ditches. Three pressure cells and two Dynatest strain gauges were installed under the steel mesh, while three other Dynatest strain gauges were installed on top of it. Pressure cells were placed in this section so that the bottom side was leveled with the SM-9.5A. A hole was dug to accommodate the fluid-housing unit of the pressure cell, and then the cell was then leveled in its position. A

small piece of geosynthetic was nailed beneath the sensitive side to protect it against angular aggregates. The connection between the wire and the fluid-housing unit also was protected carefully with Petrotac® geosynthetic to prevent bending of the wires or any other form of damage. Adequate support of the sensitive side was checked, and any gap was adjusted repetitively until acceptable measures of leveling and support were reached. After the pressure cells were tested for static and dynamic response, the wires were covered with a layer of geosynthetic. Figure 4-3 illustrates the product resulting from the pressure cells installation.

Figure 4-3. Pressure Cell Installation Covered by Steel Mesh

Installation of the Dynatest strain gauges—the most expensive instruments involved in this project, noted for their accuracy—was a delicate operation. One of the major concerns with strain gauges is their durability, both during installation and in service. When gauges are installed in a HMA layer, as in this project, they could be subjected to very large strains during compaction of the pavement layer. After installation, the major problem involves damage caused by moisture. Also, the gauges may suffer from fatigue before the HMA does. In order to prevent potential damage, gauges are protected by a coating of 27 layers. The effectiveness of this method is proven: this type of gauge has been previously tested for more than two years and subjected to more than one million large strain repetitions without incurring major damage (Ullidtz 1987).

In this segment of the project, a small hole was dug in the SM-9.5A layer to accommodate such gauges, two of which were placed at the bottom of the steel mesh. Each strain gauge was then surrounded by a small quantity of slurry seal (sand and PG 64-22 binder) that allowed the instrument to rest without generating stresses on itself. The slurry seal covers the strain gauge measuring bar fully and the flanges partially, which allows the upper part of the gauge to engage with the upper HMA layer. It was also imperative to ensure the correct alignment of each gauge, a task accomplished by using two nails to define directions. A wire was then pulled between these two nails, directing the installer to the correct alignment of the gauge. Figure 4-4 illustrates a strain gauge under mesh during installation.

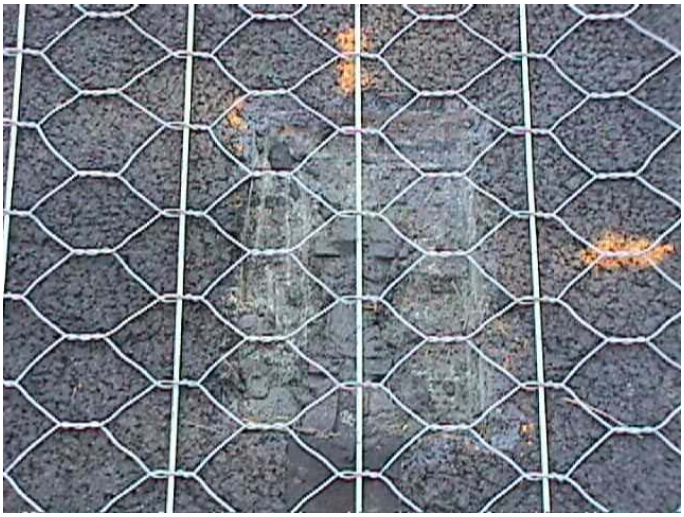

Figure 4-4. Dynatest Strain Gauge underneath the Steel Mesh during Installation

Four thermocouples were installed in this layer, two of them beneath the steel mesh and two on top of it. Of major concern in the installation of thermocouples is protection of the wire. Prior to placing the steel mesh, instrument wires were placed in small ditches and then covered with geosynthetic all the way to the outlet.

Two different types of steel reinforcement were installed in this section (see Table 4-2). The first type was located on the instrumentation area and extended 48m in the section (Type S). The remaining part of this section (50m) was covered with a second type of mesh (Type L). The SM-9.5A surface was appropriate for the installation of steel

reinforcement: it is stiff, relatively smooth, and most often used for wearing surfaces. Steel reinforcing netting was delivered in 4m-wide by 50m-long rolls. Steel reinforcement was planed to cover the driving (instrumented) lane (3.6m), extending 150mm in the other lane and 250mm in the shoulder. A loader was used to place the steel mesh. After placement, the loader was driven on the steel mesh several times to remove any existing tensions and to help level it with the existing surface (see Figure 4-5). During this phase, it was necessary to cut the edge wire every 5m, which may have otherwise resulted in steel mesh bumps or wrinkles.

Figure 4-5. Passage of a Roller on Top of the Steel Mesh to Relieve the Natural Curvature of the Roll

The second steel mesh type, Type S, was unrolled in the passing lane, then pulled manually into the driving lane, a process vital for protecting the instrumentation already installed there. Since each type of steel reinforcement is studied separately, no overlap was made between them. The three strain gauges that were installed on top of the steel

mesh were carefully passed through the layer and placed in their protection boxes to await installation later that day (see Figure 4-6). Steel reinforcement was then fixed to the SM-9.5A layer to avoid any possible distortion or shoving during the paving process. 70mm passivated steel nails were used in accordance with the manufacturer recommendations (see Figure 4-7).

Figure 4-6. Passing the Strain Gauge to the Top of the Steel Reinforcement

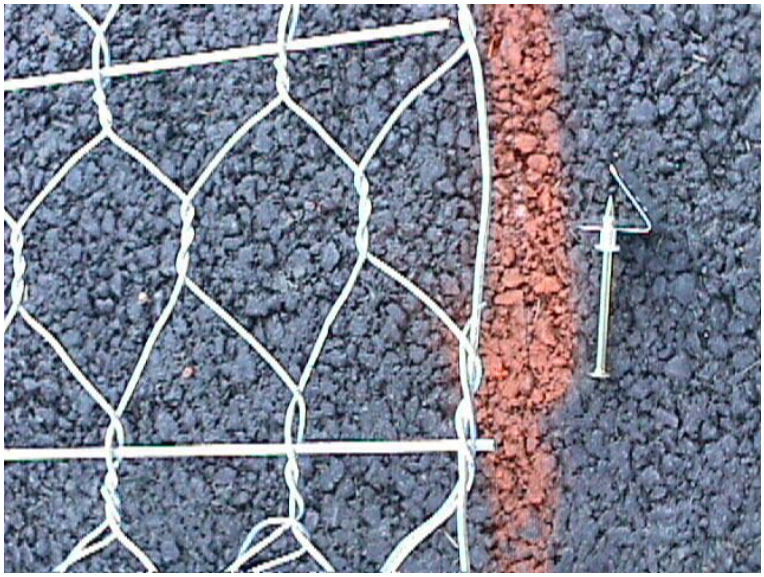

Figure 4-7. Steel Nails Used to Fix the Steel Mesh

The manufacturer recommended that the fixing point should be done by a clip, which permits hooking the material by means of the single wire mesh (neither the double twist nor the reinforcing bars have to be fixed). This pattern was changed significantly, and far fewer nails were used in most of the areas. As indicated by a subsequent ground penetrating radar (GPR) survey, this modification caused no problems during paving. Instrument locations under the SM-9.5A were marked so they could be avoided during the nailing process, and 50mm nails were used. In general, nails successfully stabilized the steel mesh. Based on the installation procedure followed in this project, the following recommendations were made to the manufacturer:

- The pattern of nailing and number of nails per area may need to be revised.
- The gun used by the sponsor does not have appropriate filling cartridges available in the US.

To ensure the successful installation of the steel mesh without major bumps during paving, ground penetrating radar (see Chapter 2 for more details on the theory of operation) was used during the construction phase. Both GPR types (i.e. ground-coupled and air-coupled) used in this project confirmed that the steel mesh installation was successful, and the final product was a leveled mesh with only minor distortions. As presented in Figure 4-8, the survey of the ground-coupled system—although affected by the common reverberation phenomenon caused by the steel nature of the mesh—indicated only minor distortions in the surface. Also, the 1GHz air-coupled GPR system, which has a greater resolution than the 900MHz ground-coupled GPR, verified a successful installation. Figure 4-9 illustrates a scan performed by this system over the steel mesh.

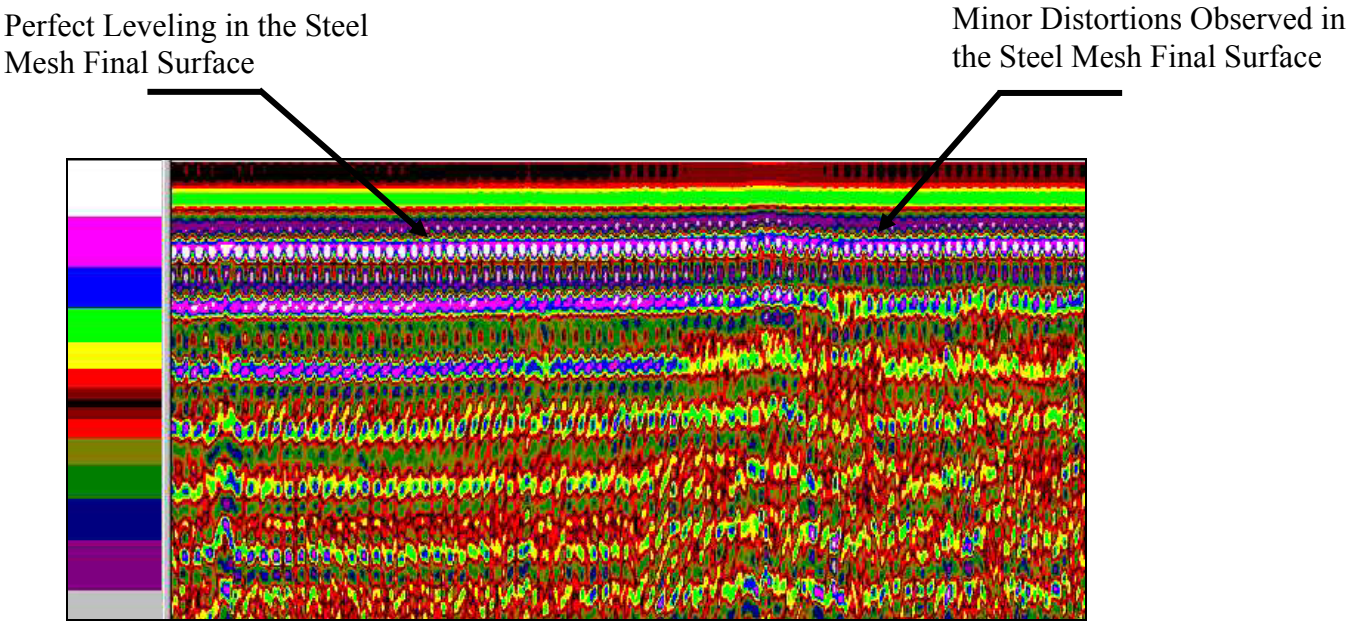

Figure 4-8. Ground-Coupled GPR (900MHz) Survey Indicating the Steel Mesh Leveling after the BM-25.0 Installation

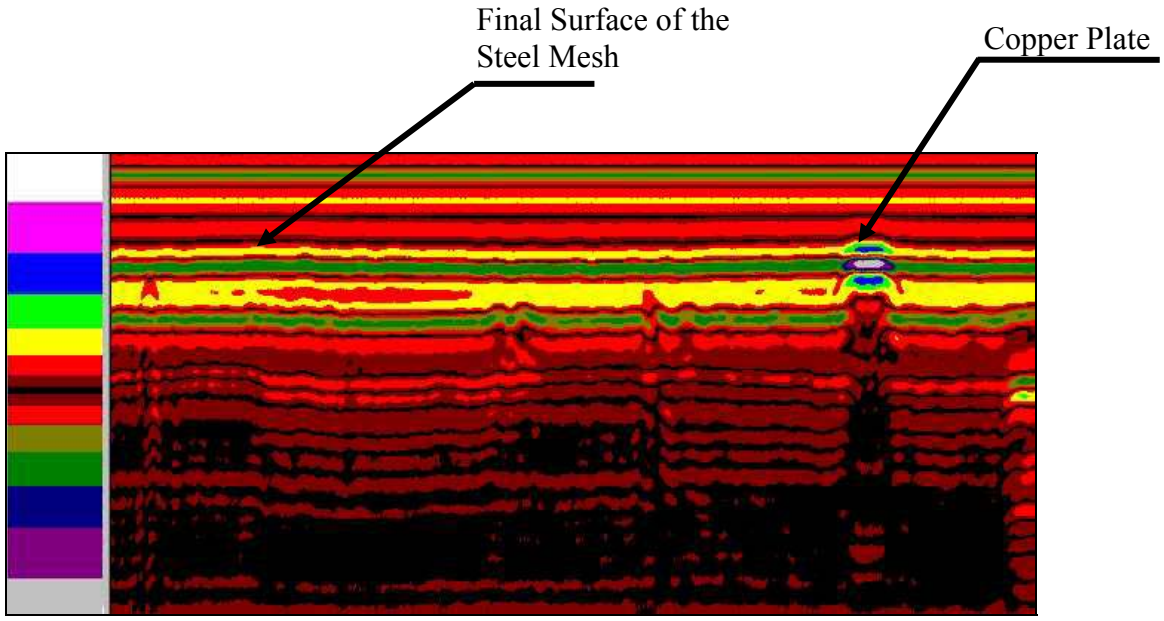

Figure 4-9. Air-coupled GPR (1GHz) Survey Indicating the Steel Mesh Leveling after the BM-25.0 Installation

To evaluate the bonding between the steel mesh and the surrounding HMA layers, core samples were extracted from Section I (see Figure 4-10). These cores confirmed strong adhesion between the mesh and surrounding materials, which—since the effectiveness of the procedure depends on transferring HMA tensile stress to the steel reinforcement—provides the key to proper installation and performance. Extracted cores clearly showed that the steel mesh was completely embedded in the BM-25.0 layer, and that bonding at the interface should be considered between the steel reinforcement and the two HMA layers.

Figure 4-10. Extracted Core from Section I

4.4.2 Section L

In Section L, mesh reinforcement was installed on top of 75mm of cement-stabilized open graded drainage layer (OGDL) and below 150mm of BM-25.0 layer (see Figure 4-11). Instrumentation and construction of this section was completed in mid November 1999, and the steel reinforcement was installed on Thursday, 23 September 1999, a sunny day with an average temperature of 21°C. Instrument installation procedures in this section were similar to those adopted for Section I. Figures 4-12(a) and (b) show the pressure cells and thermocouples installed in this section.

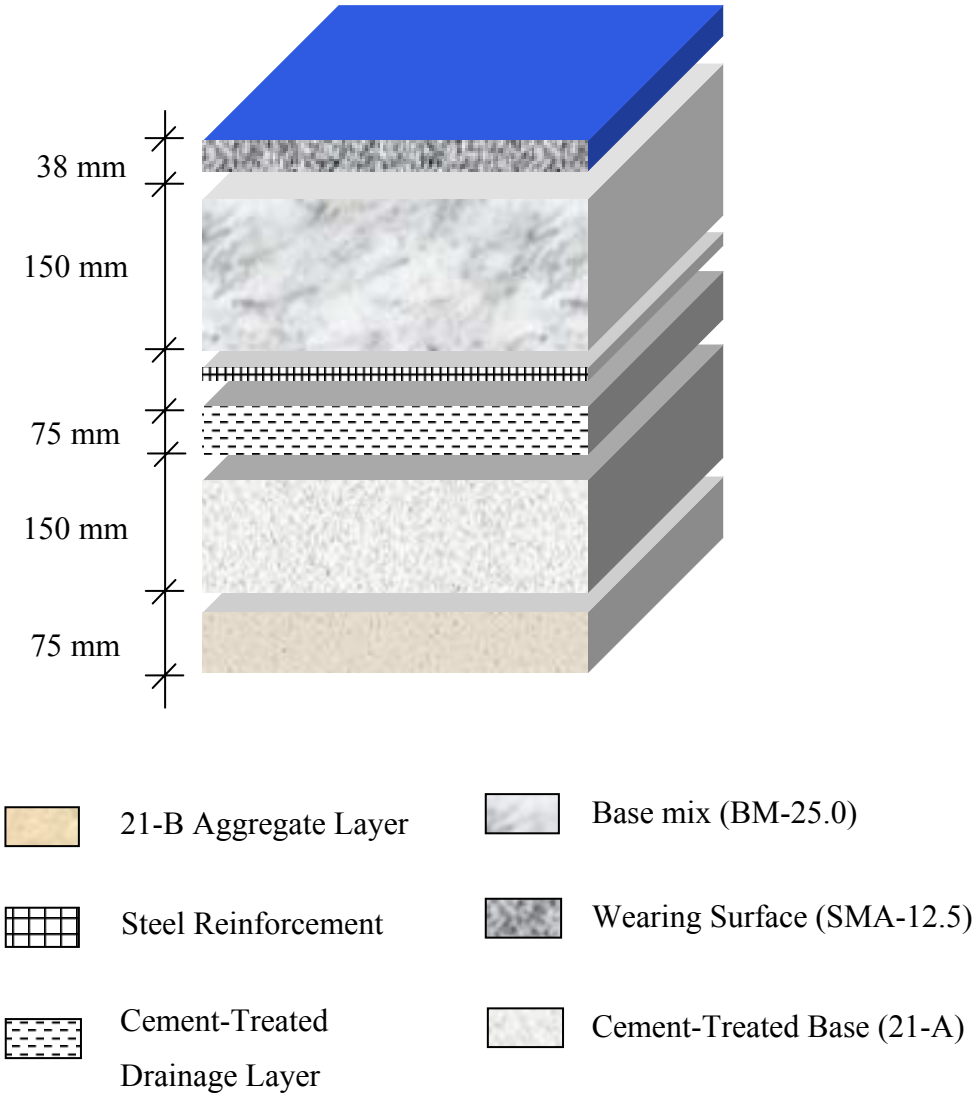

Figure 4-11. Pavement Design in Section L

The major difference between the installations in sections I and L involves placement of steel reinforcement in the latter on top of a cement-treated drainage layer. Due to problems that arose during the design and placement of this layer, the mechanical resistance of the material was very poor. As in Section I, steel nails were to be shot into the material using appropriate cartridges and fixing tools. Due to the poor mechanical resistance of the underneath layer, this method was discovered to be unsuitable in most areas.

(a)

(b)

Figure 4-12. Installed (a) Pressure Cells and (b) Thermocouples Covered by Steel Reinforcement

As an alternative, epoxy replaced the nailing but also was found to be largely inappropriate. The final alternative involved manual installation of 150mm nails into the reinforcing bars by means of clips that were manually cut. Although this operation has proven to be tedious, it was the only possible way to fix the steel mesh. The nailing pattern was reduced significantly and, due to the initial unsuccessful nailing process, far fewer nails were used in most areas. Instrument locations underneath the OGDL were

marked so they could be avoided during nailing, and to further ensure instrument safety, 50mm nails were used. In general, bonding of the steel mesh did not appear to be affected by the reduced nailing pattern. However, the evenness of the mesh appeared to be affected in some areas during placement of the upper layer. Based on the installation procedure followed in this project, the following recommendation was made to the manufacturer:

- The original nailing technique appeared unsuitable for weak foundations, and manual insertion of 150mm nails into a strong foundation proved a tedious task. In future applications, where the underneath layer has a poor mechanical resistance, placement of a slurry seal appears a suitable solution. However, such a solution is not recommended in projects, such as this one, when the underlying layer must be kept clear of clogs, as slurry seals tend to adversely affect drainage.

As in Section I, GPR was used during construction to ensure successful installation of the steel mesh. The ground-coupled system showed some distortions in the mesh surface, particularly in the instrumented area (see Figure 4-13).

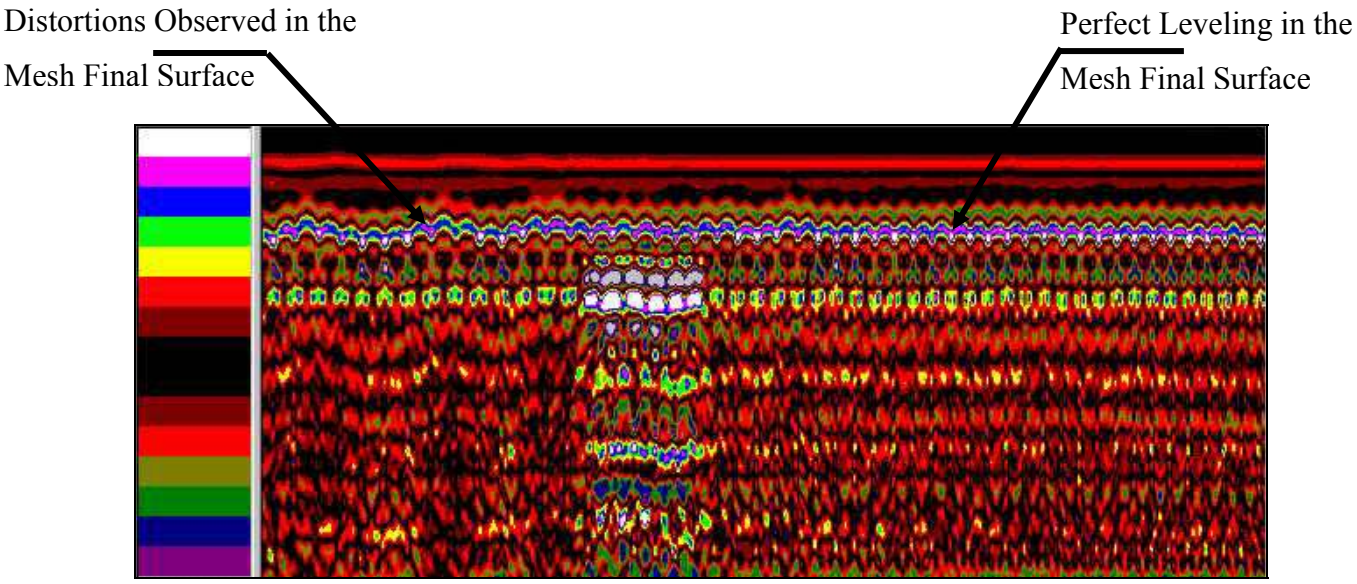

Figure 4-13. Ground-Coupled GPR (900MHz) Survey Indicating the Steel Reinforcement Leveling after the BM-25.0 Installation

To evaluate bonding between the steel mesh and surrounding HMA layers, cores were extracted from Section L (see Figure 4-14). These cores confirmed strong bonding between the steel mesh and the BM-25.0 layer. Extracted cores clearly showed that the steel mesh was completely embedded in the BM-25.0 layer.

Figure 4-14. Extracted Core from Section L

4.5 EFFECTIVENESS OF STEEL REINFORCEMENT BASED ON FALLING WEIGHT DEFLECTOMETER

4.5.1 Background

The Falling Weight Deflectometer conducts a deflection test, in which a weight is dropped on a specially-designed set of springs in order to apply a force pulse to the pavement system. This test produces an impact load with duration of 25-30msec, which corresponds to a wheel speed of 80km/hr on the upper layer (Ullidtz 1987). Surface deflections are measured and recorded by seven (or more) geophones at various distances from the loading point, as shown in Figure 4-15.

Figure 4-15. Falling Weight Deflectometer System

A number of deflection basin parameters—including radius of curvature, spreadability, and deflection ratio—which are functions of deflection values at one or more sensors, were introduced to check the structural integrity of in-service pavements. Most of these parameters reflect one simple idea: the greater the deflection(s), the weaker the pavement system. Currently, this system is widely used in the US to diagnose the structural integrity of in-service pavement. A more sophisticated analysis can be accomplished using the resulting deflection basin, which consists of (1) backcalculating the layer moduli using the multi-layer elastic theory—giving the thickness and Poisson's ratio of each layer. A composite modulus, known as the *surface modulus*, can also be used to evaluate the entire pavement structure. This modulus, which represents overall pavement stiffness, is defined as follows (Rada et al. 1994):

$$E_{comp} = \frac{p\, a_c^{\,2}(1-\mu^2)\, C}{def\ r} \qquad (4.1)$$

where

E_{comp} = modulus of the composite pavement structure;

p = contact pressure applied by the FWD;

μ = Poisson's ratio;

def = measured deflection at a given radial distance r;

a_c = loading plate radius; and

C = a deflection constant defined as follows:

$$C = 1.1 \log\left(\frac{r}{a_c}\right) + 1.15 \tag{4.2}$$

4.5.2 Section I

The Falling Weight Deflectometer test was conducted before and after installation of the steel mesh and periodically afterwards. Four points were originally selected to evaluate the effectiveness of the mesh for this particular section. Four more points were then added to improve the measurements' repeatability (see Figure 4-16). Starting in spring 2000, bimonthly FWD measurements were also performed on all sections. Such increased testing helps reduce the effects of spatial variability in the measurements. Four sets of data were utilized in this study. Each test consists of a minimum of two drops at the target load, bracketed by three drops each at ±20kN from the target load.

As previously mentioned, FWD measurements are regularly used to evaluate the structural capacity of different pavement layers in a process known as backcalculation of layer moduli. In the context of this study, FWD measurements were used to investigate the structural contribution of steel reinforcing netting to the pavement system. Figure 4-17 illustrates the measured deflections in four different locations (points 9105 vs. 9205 and points 9106 vs. 9206). For deflection measurements, the classic approach assumes the less deflection, the stronger the pavement. As noticed from these figures, in one case the reinforced area resulted in less deflection than the unreinforced area; in a second, vice-versa.

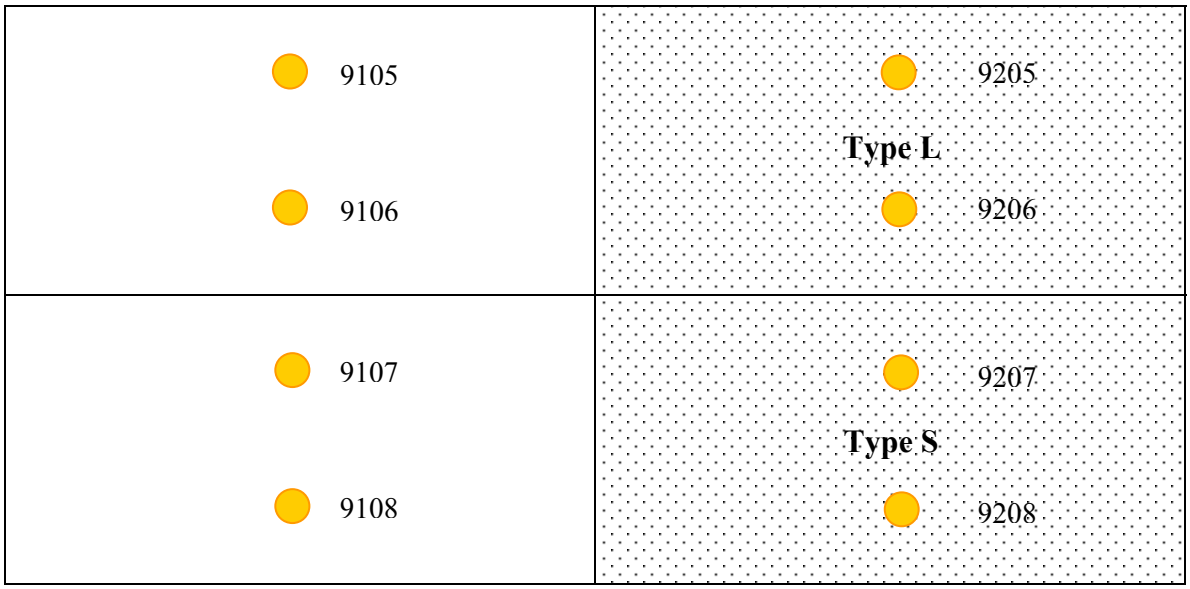

Section I

Figure 4-16. Point Selection for FWD Evaluation

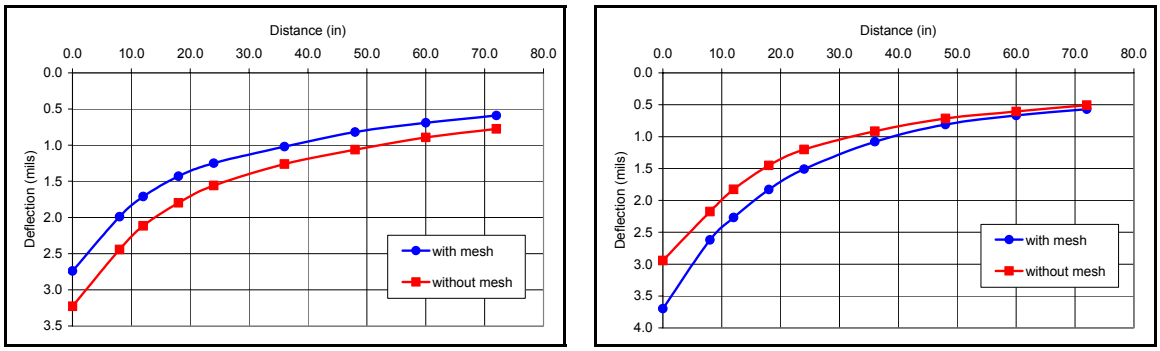

9106 vs. 9206 9105 vs. 9205

Figure 4-17. Effect of the Steel Mesh on FWD Measurements

When comparing field measurements, we must recognize that different factors, such as temperature and moisture, can affect results. Before considering the effect of steel reinforcement, we must address all such factors. For example, as presented in Figure 4-17, the difference in the far sensors (e.g. sensor 7) should not be considered in relation to the mesh, primarily because the mesh is at shallow depths and could not in any way affect the subgrade bearing capacity. Any difference could be related to the subgrade

strength between the two chosen locations. This requires enough repeatability in the measurements.

To investigate the steel mesh effects on FWD measurements, a statistical analysis of variance (ANOVA) was performed based on deflection measurements taken every 10m. This analysis was performed separately for each type of mesh and for each sensor. Table 4-3 illustrates the results of this analysis for one set of data (21st of August 2000) for Mesh 1 (Type L). Results of the analysis for all measurements are presented in Appendix B. As these results indicate, the contribution of Mesh 1 to vertical deflection is statistically significant for the first three sensors (i.e. distance 0.0, 8.0, and 12.0). On the other hand, contribution of the mesh to other sensors is insignificant, due mainly to spatial variability within the section. Based on the analysis of all FWD measurements, the following observations were made:

- Mesh 1 contributes to the HMA structural capacity at high temperatures (measurements made August 21st and May 30th). At high temperatures, HMA is compliant and exhibits a viscous-like behavior, which emphasizes the importance of the mesh when the pavement is compliant.
- The contribution of Mesh 1 to the vertical deflection at low and intermediate temperatures is insignificant (measurements made January 16th and April 4th). At such temperatures, HMA is stiff and exhibits an elastic-like behavior, which minimizes the contribution of the mesh to the pavement system.
- The contribution of Mesh 2 (Type S) to the vertical deflection is statistically insignificant at all temperatures.
- Both mesh types did not contribute to the subgrade structural capacity at any temperature. Since the mesh is installed at shallow depths, this result was expected.
- It has to be noted that the mesh contribution can not be accurately detected when FWD is used on stiff pavements (small surface deflections). More pronounced contribution to the surface deflections may be perceived in compliant pavements.

Table 4-3. ANOVA Analysis for Mesh 1 in Section I (August 21st 2000)

Sensor Distance=0.0

ANOVA: Single Factor

SUMMARY

Groups	*Count*	*Sum*	*Average*	*Variance*
With Mesh	4	9.78	2.44	0.071
Without Mesh	4	12.55	3.13	0.143

ANOVA

Source of Variation	*SS*	*dof*	*MS*	*F*	*P-value*	*F crit.*
Between Groups	0.954	1	0.954	8.87	0.024	5.98
Within Groups	0.645	6	0.107			
Total	1.600	7				

Sensor Distance=8.0

ANOVA: Single Factor

SUMMARY

Groups	*Count*	*Sum*	*Average*	*Variance*
With Mesh	4	6.46	1.61	0.028
Without Mesh	4	7.64	1.91	0.008

ANOVA

Source of Variation	*SS*	*dof*	*MS*	*F*	*P-value*	*F crit*
Between Groups	0.174	1	0.174	9.34	0.022	5.98
Within Groups	0.111	6	0.018			
Total	0.286	7				

Sensor Distance=12.0

ANOVA: Single Factor

SUMMARY

Groups	*Count*	*Sum*	*Average*	*Variance*
With Mesh	4	5.22	1.30	0.020
Without Mesh	4	6.07	1.51	0.006

ANOVA

Source of Variation	*SS*	*dof*	*MS*	*F*	*P-value*	*F crit*
Between Groups	0.088	1	0.088	6.52	0.043	5.98
Within Groups	0.081	6	0.013			
Total	0.169	7				

Sensor Distance=18.0

ANOVA: Single Factor

SUMMARY

Groups	*Count*	*Sum*	*Average*	*Variance*
With Mesh	4	4.28	1.07	0.022
Without Mesh	4	4.88	1.22	0.009

ANOVA

Source of Variation	*SS*	*dof*	*MS*	*F*	*P-value*	*F crit*
Between Groups	0.045	1	0.045	2.86	0.141	5.98
Within Groups	0.095	6	0.015			
Total	0.140	7				

Sensor Distance=24.0

ANOVA: Single Factor

SUMMARY

Groups	*Count*	*Sum*	*Average*	*Variance*
With Mesh	4	3.66	0.92	0.015
Without Mesh	4	4.03	1.00	0.020

ANOVA

Source of Variation	*SS*	*dof*	*MS*	*F*	*P-value*	*F crit*
Between Groups	0.017	1	0.017	0.94	0.367	5.98
Within Groups	0.107	6	0.017			
Total	0.124	7				

Sensor Distance=36.0

ANOVA: Single Factor

SUMMARY

Groups	*Count*	*Sum*	*Average*	*Variance*
With Mesh	4	2.83	0.70	0.011
Without Mesh	4	2.98	0.74	0.033

ANOVA

Source of Variation	*SS*	*dof*	*MS*	*F*	*P-value*	*F crit*
Between Groups	0.003	1	0.003	0.14	0.714	5.98
Within Groups	0.133	6	0.022			
Total	0.136	7				

Sensor Distance=48.0

ANOVA: Single Factor

SUMMARY

Groups	*Count*	*Sum*	*Average*	*Variance*
With Mesh	4	2.22	0.55	0.007
Without Mesh	4	2.39	0.59	0.028

ANOVA

Source of Variation	*SS*	*dof*	*MS*	*F*	*P-value*	*F crit*
Between Groups	0.003	1	0.003	0.19	0.670	5.98
Within Groups	0.108	6	0.018			
Total	0.111	7				

Sensor Distance=60.0

ANOVA: Single Factor

SUMMARY

Groups	*Count*	*Sum*	*Average*	*Variance*
With Mesh	4	1.88	0.47	0.006
Without Mesh	4	1.99	0.49	0.022

ANOVA

Source of Variation	*SS*	*dof*	*MS*	*F*	*P-value*	*F crit*
Between Groups	0.001	1	0.001651	0.11	0.746	5.98
Within Groups	0.086	6	0.014368			
Total	0.087	7				

Sensor Distance=72.0

ANOVA: Single Factor

SUMMARY

Groups	*Count*	*Sum*	*Average*	*Variance*
With Mesh	4	1.58	0.39	0.005
Without Mesh	4	1.71	0.42	0.020

ANOVA

Source of Variation	*SS*	*dof*	*MS*	*F*	*P-value*	*F crit*
Between Groups	0.002	1	0.002	0.16	0.700	5.98
Within Groups	0.076	6	0.012			
Total	0.079	7				

4.5.3 Section L

To evaluate the effectiveness of the steel mesh, two points were originally selected for this particular section. Two more points were then added to improve the repeatability of the measurements (see Figure 4-18). As with Section I, four sets of data were used in this study (April 4th 2000, May 30th 2000, August 21st 2000, and January 16th 2001).

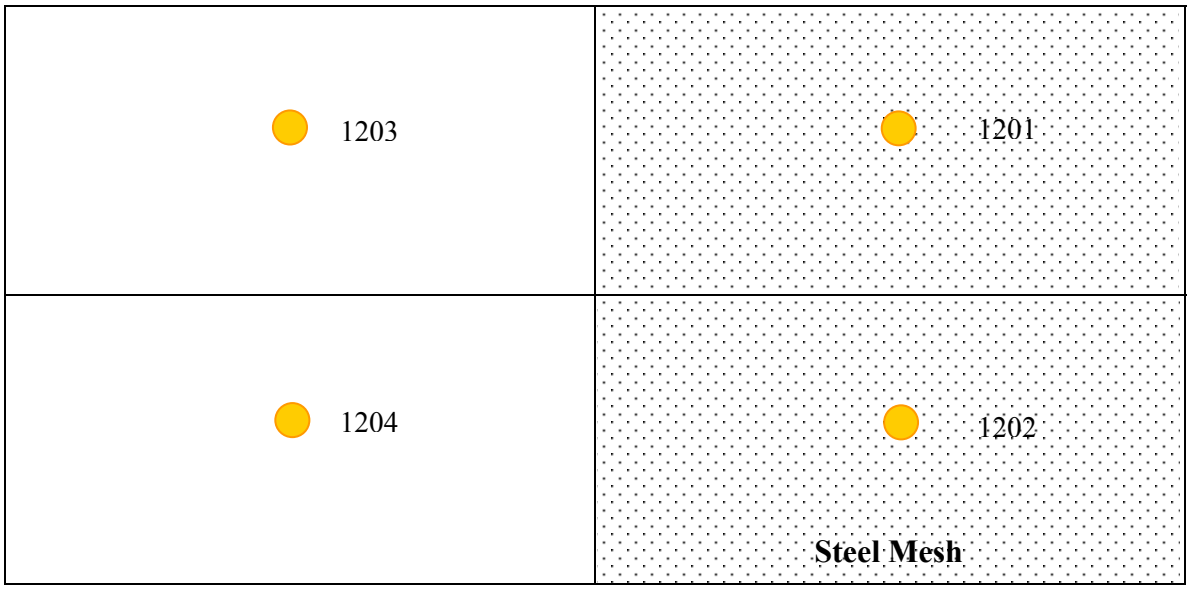

Section L

Figure 4-18. Point Selection for FWD Evaluation

Similar to the procedure used in Section I, Figure 4-19 illustrates the measured deflections in four different locations (points 1202 vs. 1204 and points 1201 vs. 1203). As with Section I, in one case the reinforced area resulted in less deflection; in a second case, the converse occurred.

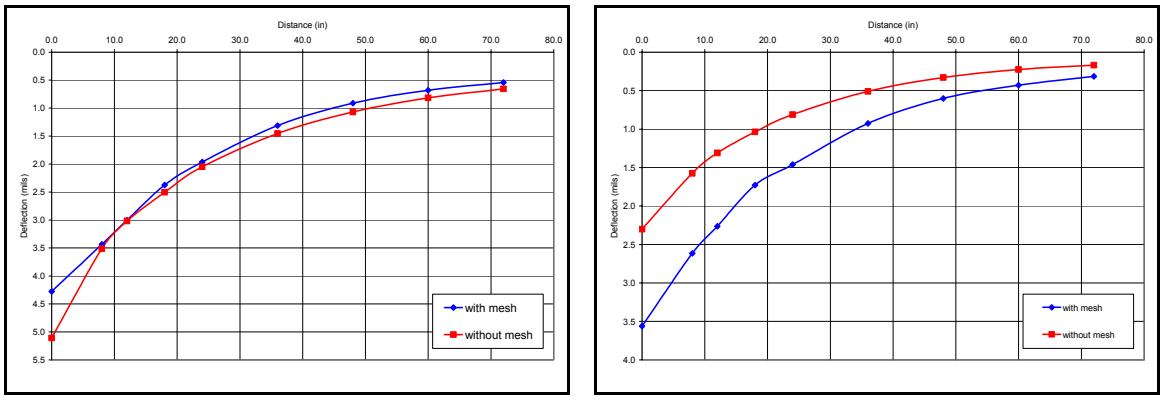

1202 vs. 1204 1201 vs. 1203

Figure 4-19. Effect of the Steel Reinforcement on FWD Measurements

To investigate the steel reinforcement effects on FWD measurements, a statistical analysis (ANOVA) was performed based on the deflection measurements taken every 10m. This analysis was performed separately for each sensor. Table 4-4 illustrates the results of this analysis for one set of data (21st of August 2000). Results of the analysis for all measurements are presented in Appendix B. Based on the analysis of all FWD measurements, the following observations were made:

- The installed steel reinforcement in this section did not prove statistically to influence the vertical deflection for all the sensors at all temperatures.
- The variability in the deflection measurements is due primarily to spatial variability within the section.
- Within this section, the subgrade bearing capacity remained relatively constant (variance for the last sensor = 0.076 microns).

To further investigate the steel mesh contribution to the vertical deflection, a theoretical FE model was formulated to simulate FWD testing. Results of this model are presented in the following sections.

Table 4-4. ANOVA Analysis for the Steel Reinforcement in Section L (August 21st 2000)

Sensor Distance=0.0

ANOVA: Single Factor

SUMMARY

Groups	*Count*	*Sum*	*Average*	*Variance*
With Mesh	4	14.99	3.74	0.004
Without Mesh	4	14.49	3.62	0.173

ANOVA

Source of Variation	*SS*	*dof*	*MS*	*F*	*P-value*	*F crit*
Between Groups	0.031	1	0.031	0.35	0.571	5.98
Within Groups	0.533	6	0.088			
Total	0.565	7				

Sensor Distance=8.0

ANOVA: Single Factor

SUMMARY

Groups	*Count*	*Sum*	*Average*	*Variance*
With Mesh	4	9.58	2.39	0.011
Without Mesh	4	9.32	2.33	0.177

ANOVA

Source of Variation	*SS*	*dof*	*MS*	*F*	*P-value*	*F crit*
Between Groups	0.008	1	0.008	0.09	0.771	5.98
Within Groups	0.569	6	0.094			
Total	0.578	7				

Sensor Distance=12.0

ANOVA: Single Factor

SUMMARY

Groups	*Count*	*Sum*	*Average*	*Variance*
With Mesh	4	7.68	1.92	0.003
Without Mesh	4	7.67	1.91	0.116

ANOVA

Source of Variation	*SS*	*dof*	*MS*	*F*	*P-value*	*F crit*
Between Groups	1.5E-05	1	1.5E-05	0.0002	0.987	5.98
Within Groups	0.359	6	0.059			
Total	0.359	7				

Sensor Distance=18.0

ANOVA: Single Factor

SUMMARY

Groups	*Count*	*Sum*	*Average*	*Variance*
With Mesh	4	6.14	1.53	0.007
Without Mesh	4	6.00	1.50	0.043

ANOVA

Source of Variation	*SS*	*dof*	*MS*	*F*	*P-value*	*F crit*
Between Groups	0.002	1	0.002	0.09	0.768	5.98
Within Groups	0.154	6	0.025			
Total	0.157	7				

Sensor Distance=24.0

ANOVA: Single Factor

SUMMARY

Groups	*Count*	*Sum*	*Average*	*Variance*
With Mesh	4	4.90	1.22	0.035
Without Mesh	4	4.76	1.19	0.032

ANOVA

Source of Variation	*SS*	*dof*	*MS*	*F*	*P-value*	*F crit*
Between Groups	0.002	1	0.002	0.07	0.795	5.98
Within Groups	0.201	6	0.033			
Total	0.204	7				

Sensor Distance=36.0

ANOVA: Single Factor

SUMMARY

Groups	*Count*	*Sum*	*Average*	*Variance*
With Mesh	4	3.13	0.78	0.007
Without Mesh	4	3.21	0.80	0.011

ANOVA

Source of Variation	*SS*	*dof*	*MS*	*F*	*P-value*	*F crit*
Between Groups	0.0008	1	0.0008	0.09	0.772	5.98
Within Groups	0.0562	6	0.0093			
Total	0.0570	7				

Sensor Distance=48.0

ANOVA: Single Factor

SUMMARY

Groups	*Count*	*Sum*	*Average*	*Variance*
With Mesh	4	2.27	0.56	0.019
Without Mesh	4	2.16	0.54	0.008

ANOVA

Source of Variation	*SS*	*dof*	*MS*	*F*	*P-value*	*F crit*
Between Groups	0.001	1	0.001	0.09	0.765	5.98
Within Groups	0.085	6	0.014			
Total	0.086	7				

Sensor Distance=60.0

ANOVA: Single Factor

SUMMARY

Groups	*Count*	*Sum*	*Average*	*Variance*
With Mesh	4	1.62	0.40	0.005
Without Mesh	4	1.58	0.39	0.003

ANOVA

Source of Variation	*SS*	*dof*	*MS*	*F*	*P-value*	*F crit*
Between Groups	0.0001	1	0.0001	0.03	0.854	5.98
Within Groups	0.0282	6	0.0047			
Total	0.0284	7				

Sensor Distance=72.0

ANOVA: Single Factor

SUMMARY

Groups	*Count*	*Sum*	*Average*	*Variance*
With Mesh	4	1.37	0.34	0.013
Without Mesh	4	1.17	0.29	0.003

ANOVA

Source of Variation	*SS*	*dof*	*MS*	*F*	*P-value*	*F crit*
Between Groups	0.005	1	0.005	0.62	0.458	5.98
Within Groups	0.050	6	0.008			
Total	0.055	7				

4.6 EFFECTIVENESS OF STEEL REINFORCEMENT BASED ON ANALYTICAL METHODS

In the past, the multi-layer elastic theory has proven the classic means for predicting flexible pavement response to vehicular loading. Although this approach is usually thought to acceptably describe regular pavement structures, the analytical consideration of a non-homogeneous interlayer system such as steel reinforcing netting (interlayer with openings) cannot be accomplished without approximations. To overcome such limitations, engineers recently have paid considerable attention to the use of FE techniques for simulating different pavement problems that could not be simulated using the traditional multi-layer elastic theory (Zaghloul and White 1993; Huang et al. 2001). The following section provides a quick overview of the multi-layer elastic theory and the FE method.

4.6.1 The Layered System Theory

The oldest method for simulating flexible pavement response to vehicular loading was developed by Boussinesq in 1885 (Boussinesq 1885). This method provides a closed-form solution for calculating stresses, strains, and deflections for a homogeneous, isotropic, linear elastic semi-infinite space under a point load. Based on this approach, the vertical stress at the centerline of the load is defined as follows (Ullidtz 1987):

$$\sigma_z = \frac{3P}{2\pi z^2} \tag{4.4}$$

where

P = point load; and

z = vertical depth of the point of interest.

A similar solution may be obtained if the point load is changed to a distributed load by integration of Equation (4.4), resulting in the following closed form solution (Huang 1993):

$$\sigma_z = q\left\{1 - \frac{z^3}{\left[a^2 + z^2\right]^{3/2}}\right\} \tag{4.5}$$

where

q = normal stress on the surface (uniform pressure applied over a circular area of radius a); and

a = flexible plate radius.

It should be noted that vertical stress and other stress components are independent of the material stiffness (Young's modulus). Likewise, similar equations are available for other straining actions. Although it is the oldest, Boussinesq's approach is still widely used for characterization of a subgrade material, usually assumed as a semi-infinite space.

In 1943, Burmister developed a closed-form solution for a two-layered linearly elastic half-space problem (Burmister 1943), which was later extended to a three-layer system (Burmister 1945). Since then, a large number of computer software programs have been developed for calculating stresses, strains, and deflections of layered elastic systems. The major assumptions of Burmister's theory are that (Huang 1993):

- Each layer is assumed homogeneous, isotropic, and linear elastic.
- All materials are weightless (no inertia effect is considered).
- Pavement systems are loaded statically over a uniform circular area.
- The subgrade is assumed to be a semi-infinite layer with a constant modulus.
- The compatibility of strains and stresses is assumed to be satisfied at all layer interfaces.

The layered theory is based on the classical theory of elasticity, which assumes that a stress function (Airy Function), which satisfies the governing differential equation (compatibility conditions), may describe the considered problem:

$$\nabla^4 \varphi = 0 \tag{4.6}$$

where

φ = an assumed stress function.

If the three-dimensional pavement structure is mathematically reduced to a two-dimensional one by assuming constant properties in all horizontal planes (axisymmetric stress distribution), it can be shown that stresses and displacements can be determined by means of the assumed stress function, as follows (Huang 1993):

$$\sigma_z = \frac{\partial}{\partial z}\left[(2-\nu)\nabla^2 \varphi - \frac{\partial^2 \varphi}{\partial z^2}\right] \tag{4.7}$$

$$w = \frac{1+\nu}{E}\left((1-2\nu)\nabla^2 \varphi + \frac{\partial^2 \varphi}{\partial r^2} + \frac{1}{r}\frac{\partial \varphi}{\partial r}\right) \tag{4.8}$$

where

r (radius) and z (depth) = cylindrical coordinates; and

ν = Poisson's ratio.

Based on the boundary and continuity (compatibility of stresses and strains) conditions, it can be shown that the following stress function satisfies Equation (4.6):

$$\varphi_i = \frac{H^3 J_0(m\rho)}{m^2}\left[A_i e^{-m(\lambda_i-\lambda)} - B_i e^{-m(\lambda-\lambda_{i-1})} + C_i m\lambda e^{-m(\lambda_i-\lambda)} - D_i m\lambda e^{-(\lambda-\lambda_{i-1})}\right] \quad (4.9)$$

where

A_i, B_i, C_i, and D_i = constants of integrations for layer i (from boundary and continuity conditions);

H = distance from the surface to the upper boundary of the lowest layer;

ρ = equal to r/H;

λ = equal to z/H;

m = a parameter; and

J_0 = Bessel function of the first kind of order 0.

Substituting from Equation (4.9) into Equations (4.7) and (4.8), and following an iteration approach by changing the value of m until convergence occurs, one may calculate the different straining actions—stresses, strains and displacements—of the layered system. Two things about this process are clear: (1) it is somewhat involved and not easily evaluated, and (2) to be efficient it requires the use of computer software. The most effective software programs for solving a layered system problem are the following:

- **VESYS** (1977-1988): This software, which is based on Burmister's layered theory, was originally designed to solve a three-layer system subjected to a single-axle load. Since the first version, several modifications have been introduced to consider linear viscoelastic properties of HMA (curve fit the creep compliances with a Dirichlet series), as well as seasonal variations in base and subgrade properties. A damage model was also recently introduced to predict rutting, fatigue, and roughness performances (Brademeyer 1988).

- **ILLI-PAVE** (1980): This software considers the pavement as an axisymmetric FE model (Raad and Figueroa 1980). In this case, displacements are assumed to occur only in the radial and axial directions (no circumferential displacements are allowed). The major disadvantage of this software is that it can handle only a single load, and only static analysis is allowed. However, stress-dependent materials can be accurately modeled using the Mohr-Coulomb failure criterion.
- **ELSYM5** (1985): This program is a linear elastic layer software that can handle up to five layers (Kopperman et al. 1986). Using the superposition theorem, the pavement may be loaded with one or more identical uniform circular vertical loads. This software considers the validity of the five layered theory assumptions: static loading, elastic homogeneous material, compatibility of stresses and strains, no inertia effects, and semi-infinite subgrade.
- **KENLAYER** (1993): This software is based on the solution of an elastic multi-layer system under a circular loaded area (Huang 1993). Using the Correspondence Principle, several modifications have been introduced to the original layered theory allowing for nonlinear elastic and viscoelastic materials. This software also allows for damage analysis, as well as dynamic stationary analysis. It should be emphasized that a stationary load is different from a moving load because the former changes only in magnitude, not position. In the case of a dynamic stationary load, the principal axis directions do not change; they do, however, in the case of a real moving load. Bonding between different layers can also be adjusted by assigning a single number, where 0 means unbonded and 1 means fully-bonded.
- **CIRCLY4** (1994): This software presents a new and more sophisticated approach for pavement analysis and design (Wardle and Rodway 1998). Unlike most of the available computer software for pavement analysis, this software is Windows-based. It is able to calculate stresses, strains, and displacements based on the layered elastic theory, and then uses the calculated straining actions to perform design calculations. The user can specify all design inputs, including nonlinear material properties, as well as each material's performance criterion.

- **BISAR** (1973-1998): This software, developed by Shell, uses the multi-layer elastic theory to calculate pavement responses to both vertical and horizontal loading (De Jong et al. 1973). The latest version of this software (BISAR 3.0) is Windows-based, and can calculate the principal stresses and strains at any location in pavement. In addition, different pavement interface conditions may be defined using shear spring compliance between the layers. The main disadvantage of this software is that only elastic material properties can be defined.
- **VEROAD** (1993-1999): This software consists of a set of computer modules for linear viscoelastic analysis of flexible layered pavement systems (Nilsson 1999). For the first time, this software considers both the viscoelastic nature of HMA materials using a Burgers' model and the movement of the wheel load. As a result, both the variation of the principal axis directions and the time-dependent responses of the materials may be obtained. In addition, dissipated energy and permanent deformations can be calculated.

Although the layered theory involves several assumptions that may be questionable, the simplicity of the multi-layer analysis is usually thought to overcome any uncertainty in results (Zaghloul and White 1993). However, it is clear that this method is incapable of reflecting the "exact" responses of pavements subjected to dynamic traffic loading. The exact responses of a system are rather complex and depend on the interactions between different factors usually neglected in the layered theory (OECD 1992):

- The magnitude, frequency, contact conditions, speed, and rest period between loads.
- The environmental conditions (temperature, moisture, etc.).
- The material property of each layer (viscoelastic, stress-dependent behavior, etc.).
- The load induced by a tire in both the vertical and lateral (longitudinal and transverse) directions.
- The impact on performance created by interface conditions between the different layers. It has recently been shown that the interface condition dramatically

changes the strain field in the wearing surface and base layers and could increase the vertical strains on top of the subgrade by up to 20% (Romanoschi and Metcalf 2001).

4.6.2 The Finite Element Method

As opposed to the relatively simple layered theory, the FE method can be a complex and costly analysis tool; it is thus employed only when a more precise simulation of pavement problems and the most accurate results are required. This method can include almost all controlling parameters: dynamic loading, discontinuities such as cracks and shoulder joints, viscoelastic and nonlinear elastic behavior, infinite and stiff foundations, system damping, quasi-static analysis, and crack propagation, among others. Although this technique still requires strong engineering knowledge, its flexibility and accuracy allow greater insight into more complicated systems such as reinforced flexible pavements.

During the last decade, FE techniques have been used successfully to simulate different pavement problems that could not be recreated using the simpler multi-layer elastic theory. In 1993, for example, Zaghloul and White effectively employed three-dimensional (3D) dynamic finite elements to investigate the effect of load speed and HMA properties on the resulting rut depth (Zaghloul and White 1993). In 1994, Uddin et al. used FE techniques to investigate the effect of discontinuities on pavement response (Uddin et al. 1994). The following section presents a brief but insightful overview of the FE formulation process.

4.6.2.1 The Finite Element Formulation

The FE method approximates the behavior of a continuum by an assembly of finite elements (Holzer 1985). Formulation and application of the finite element method are divided into eight basic steps (Desai 1979):

1. **Discretize the Structure into a Suitable Number of Small 'Elements,'** called finite elements.

2. **Select Approximation Models for the Unknown Quantities**, which can be displacements, stresses, or temperatures in heat flow problems.

3. **Define the Stress-Strain Constitutive Equations**, which describe the responses (strain and displacement) of a system to the applied force.

4. **Define the Element Behavior Equations**, which can be derived using energy methods as follows:

$$[k] \{q\} = \{Q\} \tag{4.10}$$

where
[k] = element stiffness matrix, with size n x n, where n is the number of the degree of freedoms of the formulated problem;
{q} = a vector of nodal displacements; and
{Q} = a vector of nodal forces.

5. **Assemble Element Equations and Introduce Boundary Conditions**, from which the equations describing the behavior of the entire problem can be obtained.

6. **Solve for the Nodal Displacements**, by solving the set of linear simultaneous equations presented by Equation (4.10).

7. **Calculate other Functions of Interests from Nodal Displacements**, such as stresses, moments, and shear forces based on the assumed constitutive equations.

8. **Interpret Results and Mesh Refinement**, from which the problem output is evaluated and mesh refinement is decided (if necessary) to obtain the required level of accuracy.

It is important to realize that in the FE method, the level of accuracy obtained depends on different factors, including the degree of refinement of the mesh (element dimensions), the order of the elements (higher order elements usually improve the accuracy), and location of the evaluation (results are more accurate at the Gauss points). Appropriate selection of the boundary conditions and the load discretization process also directly affect the model accuracy. In general, since displacement calculations involve an integration process, while stress calculations involve a differentiation process, the results of the former are always more accurate than those of the latter.

4.6.2.2 Application of the FE to Pavement Engineering

Three different approaches have been used for FE modeling of a pavement structure: plane-strain (2D), axisymmetric, and three-dimensional (3D) formulation. Each approach possesses clear advantages and disadvantages in pavement application. In this study, highlighted advantages and disadvantages are based on the commercial software program ABAQUS, version 5-8.1 (ABAQUS 1998).

Plane-Strain Approach: This formulation assumes that the third dimension of a pavement structure (Y-Direction) has no effect on pavement responses to traffic loading. Typical plane-strain assumptions are assumed valid:

$$\varepsilon_{yy} = \varepsilon_{xy} = \varepsilon_{zy} = 0 \tag{4.11}$$

Unfortunately, field measurements suggest that the longitudinal strain (ε_{yy}) is significant and thus cannot be neglected. Moreover, previous researchers have concluded that plane-strain models could not accurately simulate pavement responses to actual traffic loadings (Cho et al. 1996). The only advantage of this approach is that it requires little computational time and memory. Minimizing the computational time in favor of inaccurate results was, however, not justified in this study.

Axisymmetric Approach: This formulation considers that the 3D pavement structure is mathematically reduced to a 2D one by assuming constant properties in all horizontal planes. Although it is assumed that the traffic load is applied over a circular area, this model still provides a 3D solution based on a 2D formulation using cylindrical coordinates (radius r and depth z). In this case, displacements are postulated to occur in the radial and axial directions only (no circumferential displacements are allowed). The axisymmetric formulation is presented in Figure 4-20.

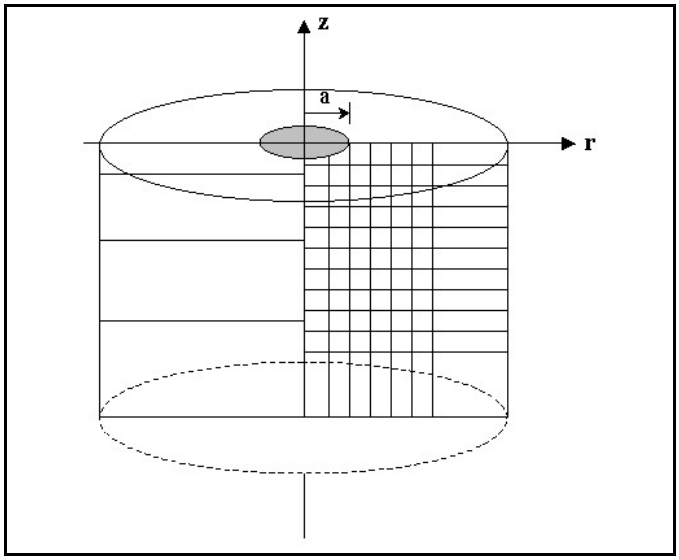

Figure 4-20. Axisymmetric Finite Element Formulation

At the Virginia Smart Road, a preliminary axisymmetric model was formulated for a regular pavement structure (Section B). To verify the correctness of the FE discretization, the assumed boundary conditions, and the applied load, a hypothetical model with one type of material was formulated. Results of this model were then compared against Boussinesq's exact form solution (see Equation 4.4). This comparison, shown in Figure 4-21, suggested the suitability of the FE model.

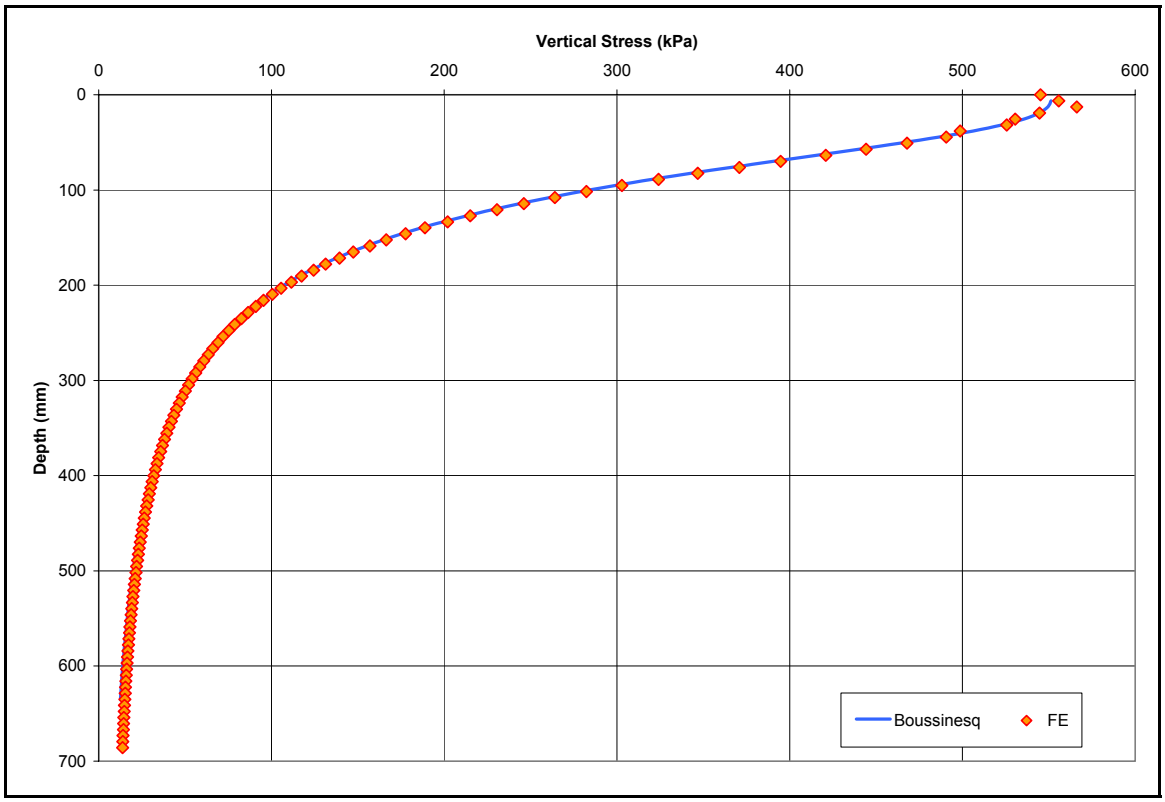

Figure 4-21. Comparison of the Axisymmetric FE Approach to Boussinesq's Closed Form Solution

The calculated vertical stresses were compared to the measured values in a typical section at the Virginia Smart Road for the steering axle during a test conducted at an 8km/hr speed. Figure 4-22 illustrates the comparison between the measured and computed vertical stresses at different depths for section B. As shown in this figure, field-measured and calculated stresses show general agreement. However, the developed model was found to grossly underestimate the measured strain, a failure which might be due to the assumed linear elastic behavior of all materials, the static nature of the load, and/or the inaccuracy of the layer moduli.

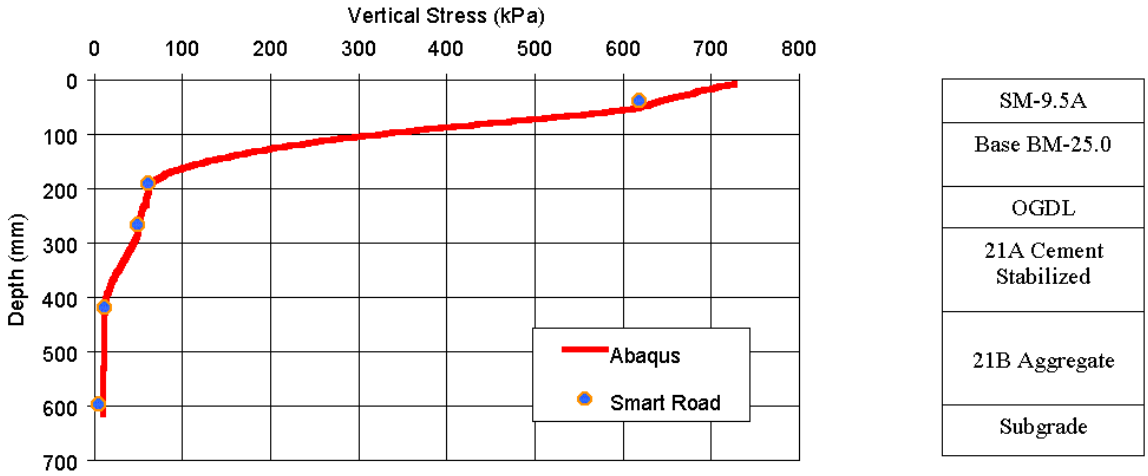

Figure 4-22. Computed and Measured Vertical Stresses at Different Depths in Section B at the Virginia Smart Road

Observations of this study and a review of pertinent literature (Cho et al. 1996) indicated the accuracy of the axisymmetric approach in simulating regular pavement problems. However, in pavement sections I and L, which represent a steel-reinforced pavement system, the axisymmetric formulation is for the following reasons deemed inappropriate:

- Steel reinforcing netting is a non-homogeneous interlayer with openings. Under the axisymmetric model, the only method available for formulating such a layer assumes a system as a homogeneous layer with an equivalent modulus of elasticity. This does not simulate its actual mechanism in pavement and thus could lead to unacceptable errors and inaccurate results.
- Factors such as the effects of the opening sizes or the diameter of the rods might not be accurately determined.

Three-Dimensional Approach: This approach can simulate the pavement structure accurately, including almost all controlling parameters (dynamic loading, discontinuities, infinite and stiff foundations, among others). Although several advantages are offered by 3D modeling of a pavement structure, the technique requires much more computational time and data storage memory. The consideration of the third dimension usually results

in gross approximation in the model geometry, and, therefore, unacceptable results may be obtained. Model preparation is also much more labor intensive; therefore, the use of a graphical user interface (GUI) for preprocessing is highly recommended. The GUI program utilized in this study was MSC/PATRAN (1996).

4.6.3 Modeling Process

The following sections present the major assumptions of the developed models. Most of the results and observations indicated are valid exclusively for the 3D model developed to simulate vehicular loading on steel-reinforced sections. Although most of the rules and findings highlighted in these sections were implemented in other models, some modifications were required due to special circumstances. These modifications were identified in their corresponding sections.

4.6.3.1 Element Types

Selection of element types is an important step in the modeling process. ABAQUS 5.8-1 provides an extensive element library that assures a powerful, flexible modeling capacity. Most of the elements commonly used for stress analysis follow a specific mathematical theory that accurately describes their behavior. For example, a beam element assumes that a three-dimensional continuum may be described by a one-dimensional approximation (i.e. member's behavior can be estimated entirely from variables that are functions of position along the beam axis only). Therefore, a key issue in the selection of an element library is assurance that the assumed mathematical theory can be applied to the problem under consideration. Due to the potential complexity of the pavement problem—and since the behavior of a layered system might not be approximated using truss, beam or shell elements—solid (continuum) stress/displacement elements were selected to simulate the considered problem.

The continuum element library includes first-order or linear interpolation elements and second-order or quadratic interpolation elements in one, two, or three

dimensions. Triangles and quadrilaterals are available in two dimensions; and tetrahedrals, triangular prisms, and hexahedra ("bricks") are provided in three dimensions. In general, when compared to quadratics, triangular elements have very poor convergence rates. With the use of continuum elements, a choice must also be made between full or reduced integration elements. Reduced integration usually means that the scheme used to integrate the element's stiffness involves one order less than the full scheme (ABAQUS 1998). Although one might assume that reduced integration elements would provide a less accurate solution than full integration elements, their rate of convergence is actually much faster. Moreover, reduced integration elements do not suffer from volumetric or shear locking (Hua 2000).

Given their successful implementation in previous pavement research studies (Zaghloul and White 1993; Hua 2000), the eight-node, first-order brick element with reduced integration (C3D8R) was selected for use in this study.

4.6.3.2 Infinite Elements

A pavement structure is defined in unbounded domains—e.g., in the horizontal and vertical directions to some extent, if a bedrock layer is far enough to be considered—where the region of interest is small compared with the surrounding medium. Three alternatives may be used to model an unbounded domain (Kim and Hjelmstad 2000; ABAQUS 1998):

- Treat the domain as a semi-infinite space, as followed in the multi-layer elastic theory (Burmister 1943). This approach is not directly applicable to the FE method.
- Extend the FE mesh to a far distance, where the influence of the surrounding medium on the region of interest is considered small enough to be negligible. The major disadvantage of this approach is that a huge number of finite elements are required to model accurately the infinite domain.

- Simulate the region of interest using ordinary finite elements, and simulate the far-field region using infinite elements. Infinite elements can capture the decay of field variables with respect to the distance from the pole (the center of loading). The formulation of an infinite element's behavior is exactly the same as that of ordinary elements.

In this study, infinite elements (CIN3D8 and CINPE5R) were used in all models to simulate the far-field region in the horizontal directions. CIN3D8 is an 8-node 3D linear infinite element, while CINPE5R is a 5-node 2D quadratic infinite element. Elastic element foundations were used to simulate the support provided by the subgrade without fixation of the nodes at the bottom of the model.

4.6.3.3 Boundary Conditions and Contact Modeling

Proper choice of boundary conditions significantly impacts the model response. Since the proposed model simulates an entire pavement structure, it was not realistic to impose any fixation to the model, except in the case of simulating bedrock. Instead, infinite elements were used to simulate the far-field region in the longitudinal and transverse directions. In addition, using the symmetry in loading and geometry, only half the model was simulated. This required imposing a boundary on the axe of symmetry in the X-direction (see Figure 4-23).

Elastic element foundations were used to simulate the subgrade's support of the pavement structure. These elements, which act as nonlinear springs to the ground, provide a simple way of including the stiffness effects of the subgrade without fixation of nodes at the bottom of the model.

Since no direct measurement of the foundation stiffness (plate loading test) was feasible at the Virginia Smart Road, the assumed value was back calculated for each section to reflect the resistance provided by the subgrade and, eventually, a stiff layer of bedrock. A proposed guideline for the foundation stiffness was followed, where 65, 135, and 270 N/cm^3 represent low, medium, and high levels, respectively (White 1998).

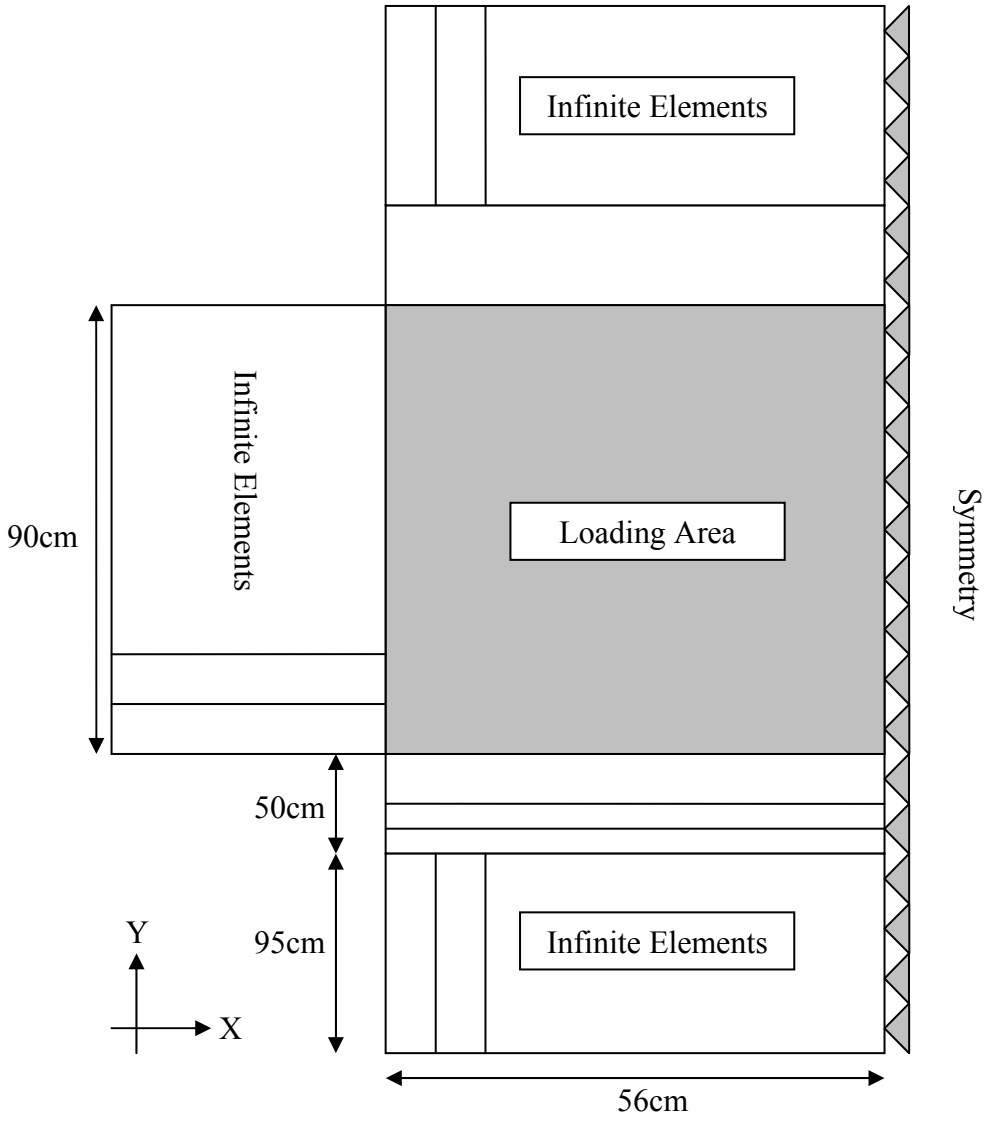

Figure 4-23. Plan View of the Model Dimensions and Boundary Conditions

Contact between the wearing surface and the base HMA layers, as well as between the base HMA and the drainage layers, was assumed to be of a friction type (Mohr-Coulomb theory), with a friction angle of 45°C. Friction-type contact was also modeled between the 21-A cement-treated subbase and the 21-B granular subbase.

4.6.3.4 Loading Area and Model

To accurately simulate pavement response to vehicular loading, one must determine the exact area of contact between tire and pavement. In the layered theory, due to its use of axisymmetric formulation, it is assumed that each tire has a circular contact area. The tire-pavement contact area is not circular; in fact, a square shape seems more realistic. With regular tires, the actual contact area assumes a generally rectangular shape with a constant ratio between the width and the length (0.68; Huang 1993). Within the context of this study, an equivalent rectangular contact area was assumed (see Figure 4-24). However, it should be understood that a tire's type and its inflation pressure, along with the magnitude of the load, will affect the shape of the footprint. These dimensions were selected to automatically fit in the formulated FE mesh, where geometries were dictated by the steel reinforcement geometry.

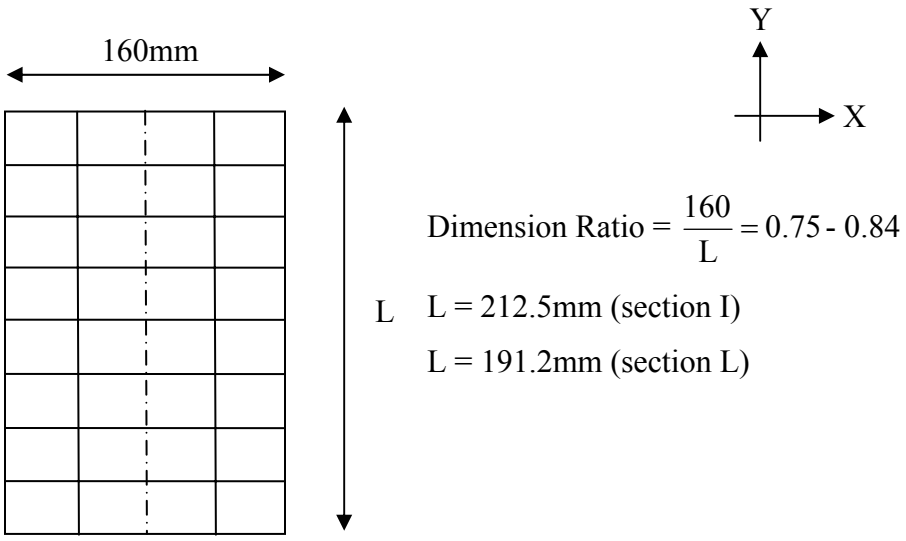

Figure 4-24. Dimensions of Tire Contact Area

On the other hand, contact stress was assumed to be uniformly distributed over the area. Although in actual pavement structure, load is transferred through the tread ribs, measurements using a Vehicle-Road Surface Pressure Transducer Array (VRSPTA) have shown that vertical contact stress is relatively uniform over the contact area (Nilsson 1999). However, this assumption is valid only for normal inflation pressure. When low

pressure is involved, maximum contact stress would be at the tire's edges; high pressure, at the tire's center. It has to be noted that tire treads also affect pressure distribution.

In the FE, a load is applied to the top surfaces, then discretized over the nodes. To accurately simulate the movement of the tire over the loading area, vertical stress measurements at the Virginia Smart Road involving the bottom of the wearing surface (depth = 38.1mm) were discretized into small rectangular shapes. For the simulated speed (8km/hr), measured vertical stress was considered, being first normalized with respect to the maximum-recorded value (Loulizi et al. 2002). The normalized vertical stress was then multiplied by the average tire pressure expected during movement (724kPa). In total, up to 18 different steps (locations of the load) were required to achieve one full passage of the tire over the entire model (see Figure 4-25). It should be noted that the loading time was found to increase with depth and that considering the loading time at a depth of 38.1mm representative of the surface loading time may involve some approximations.

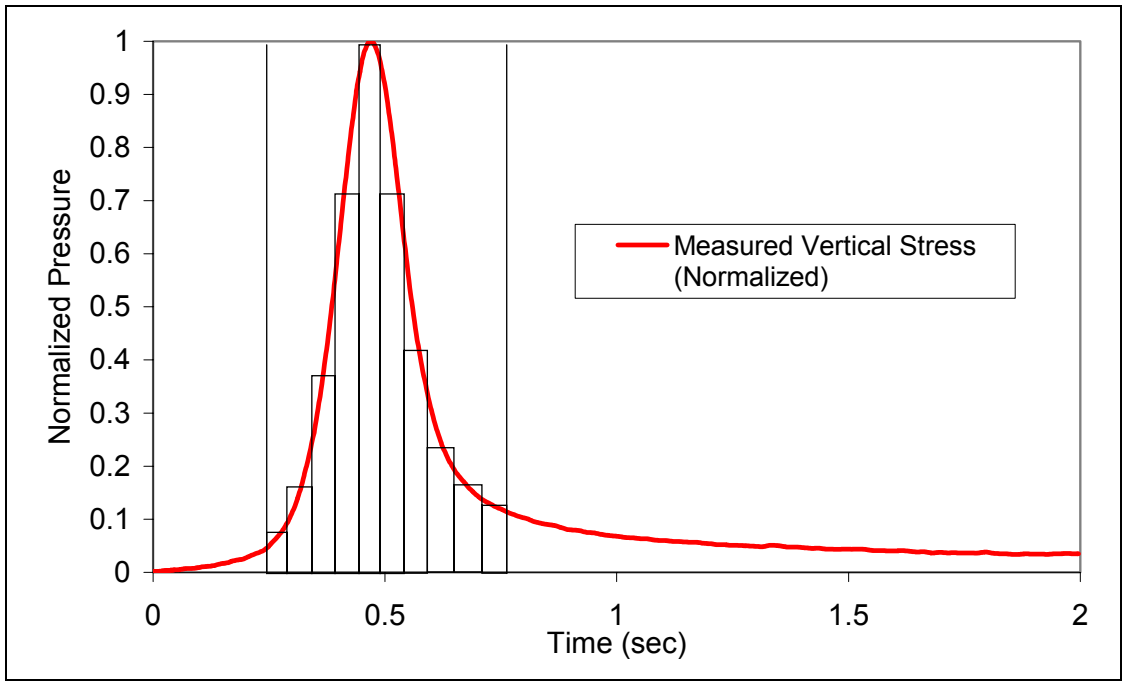

Figure 4-25. Load Amplitude Function

4.6.4 Sensitivity Analysis

When evaluating the results of any FE model, two criteria must be checked (Holzer 1985):

- The FE solution has to converge to the continuum model solution. To ensure this criterion, a regular mesh refinement process can be used as long as the finest mesh contains all previous meshes. The FE solution is then checked against a simplified solution. For a static loading case, this study used the layered theory solution.
- The accuracy of the FE model has to be acceptable within the context of the application. Bathe's criterion states that FE mesh is sufficiently fine when jumps in stresses across inter-element boundaries become negligible (Bathe 1990). The jump in stresses can be considered within the same plane or at the interfaces between different layers.

To ensure the accuracy of the results, several aspects of the FE model were analyzed and refined until specific criteria were met. When dealing with 3D FE modeling, three dimensions (a, b, and c) need to be carefully selected as they all directly affect the level of accuracy obtained from the model (see Figure 4-26). To ensure continuity of the nodes between the different layers (including the mesh) in the considered problem—which involved a steel-reinforced flexible pavement structure—the in-plane dimensions (a and b) were directly dictated by the steel reinforcing mesh geometry and by selecting an acceptable moving distance for the load during the step. Therefore, the in-plane dimension (a) was selected between 25.0mm and 19.1mm depending on the steel mesh geometry. Also, the in-plane dimension (b) was chosen to be 17.5mm in order to capture pavement responses to the movement of the load on top of the point of interest. These dimensions were adequate to reduce jumps across inter-element boundaries within the same XY plane.

Selecting element thickness (dimension c) proved to be a more complicated task. Each layer of elements represents an additional 3360 degrees of freedom to the model, which represents a significant increase in computational time and data storage space

requirements. However, at the interface between the layers, the continuity of stresses is highly affected by the selected element thickness. For example, assuming a 25.4mm element depth resulted in an unacceptable jump in the vertical stress at the surface mix–base mix interface of 50kPa. Therefore, a detailed sensitivity analyses of this variable was performed.

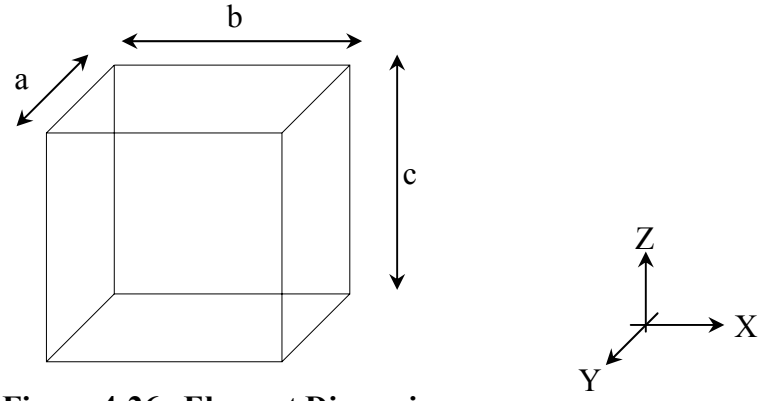

Figure 4-26. Element Dimensions

Table 4-5 illustrates the geometric properties of each investigated case. All cases simulate the pavement design in Section I without steel reinforcement, assuming a static loading. The element thickness specified in Table 4-5 was used to model the wearing surface HMA, the base HMA, and the intermediate HMA (SM-9.5A) layers. For bottom layers drainage and 21-A, a constant element thickness of 12.7 mm was used; 21-B, was modeled as a single-element layer. As mentioned earlier, infinite elements were used to simulate the far field region horizontally in the model.

Table 4-5. Sensitivity Analysis

Case ID	Element Thickness (mm)	Model Size (dof)	Number of Elements
A	L*	87,222	22,259
B	50.8	92,430	23,855
C	25.4	100,242	26,249
D	12.7	118,470	31,835
E	6.35	157,530	43,805
F	3.175	235,650	67,745

* L = Layer Thickness

Due to the symmetry of loading and geometry, only half the pavement structure was modeled. Figure 4-27 illustrates the general layout of the FE model (Case A).

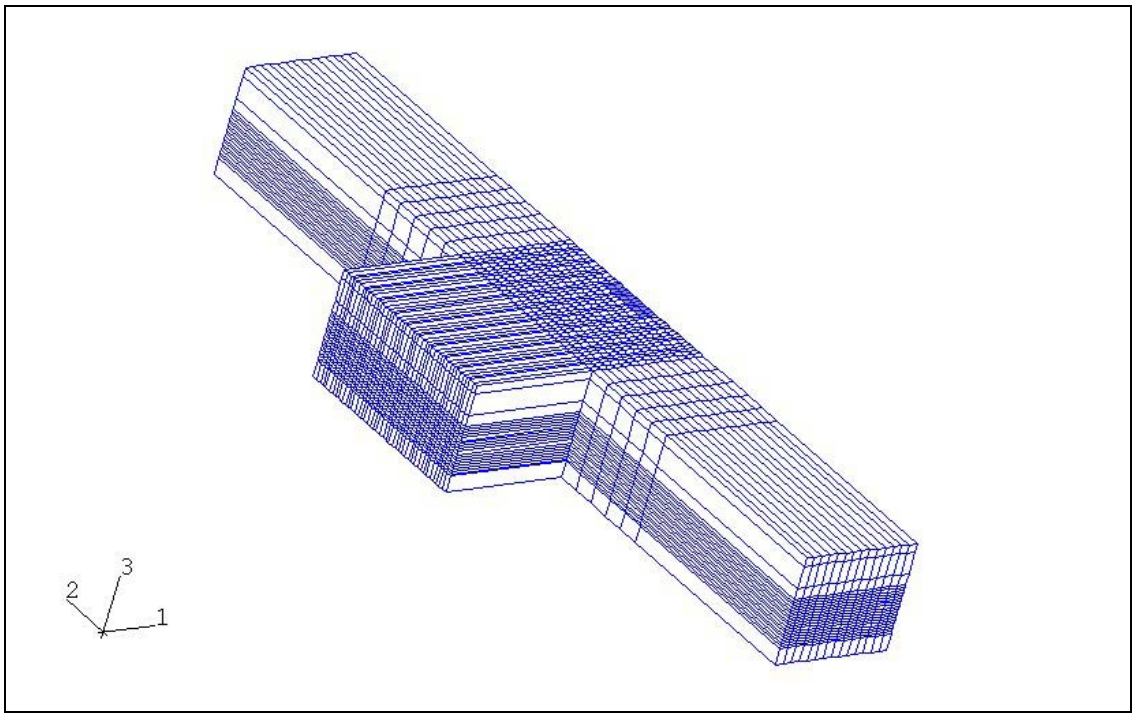

Figure 4-27. General Layout of the Finite Element Model

The first criterion used to evaluate the different cases is determining the jump in vertical stresses that can occur at the critical interfaces: surface mix – BM-25.0, BM-25.0 – SM-9.5A, and SM-9.5A – drainage layer. For a continuum model, no jumps in vertical stresses should occur at the interface between the layers. Figure 4-28 illustrates the difference in vertical stresses at different interfaces within the pavement model. As this figure illustrates, the problem of jumps in vertical stresses can be significantly minimized by appropriate refinement of the mesh. It appears also that only Cases E and F provide an acceptable level of accuracy.

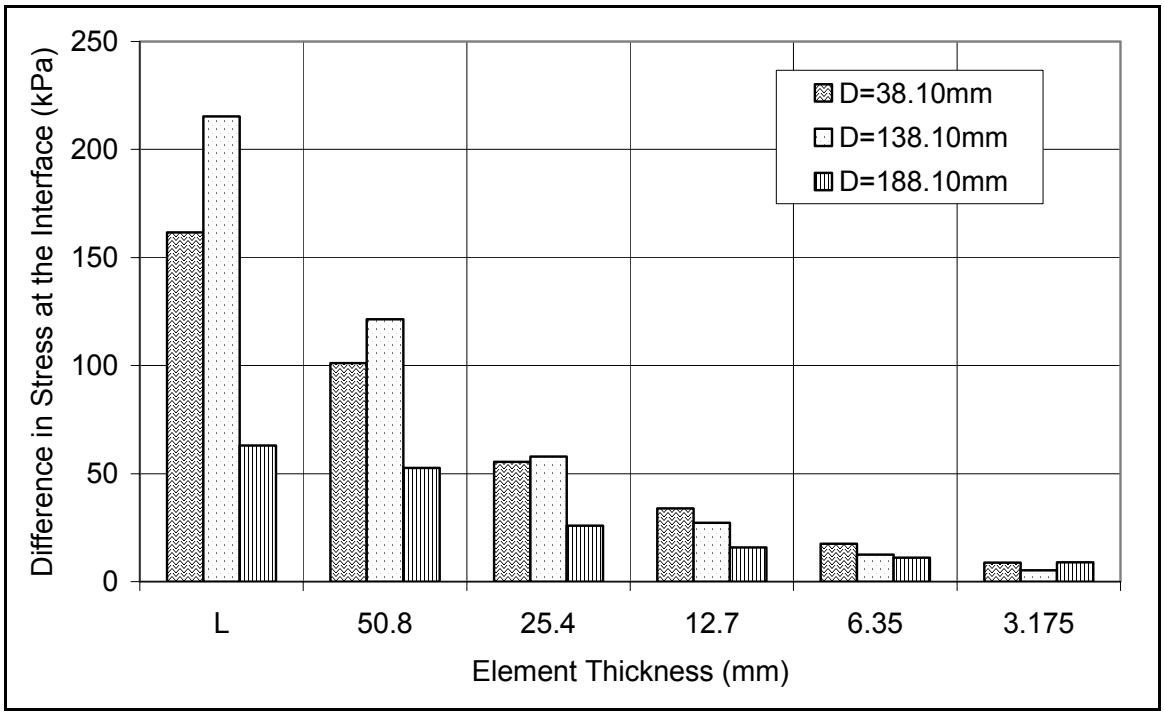

Figure 4-28. Jumps in Vertical Stresses at the Critical Interfaces

To further evaluate the accuracy of each case, similar models were developed for the same loading and material conditions using KENLAYER and BISAR 3.0. Although the two programs are based on the same approach, the iterative nature of the solution results in some discrepancies between the two programs; see Equation (4.8). In fact, it was found that the KENLAYER software failed to converge to a realistic solution at a shallow depth, a situation dependent on several factors, including loading area and material properties. Results presented in Figures 4-29(a) and (b) show convergence of the vertical stresses with mesh refinement. However, results of these models do not appear to converge to the BISAR's solution as the mesh is refined, although they are assumed to be close. Moreover, the level of accuracy is not constant for all critical depths. Based on these observations, two models were considered for further investigations: Cases E and F.

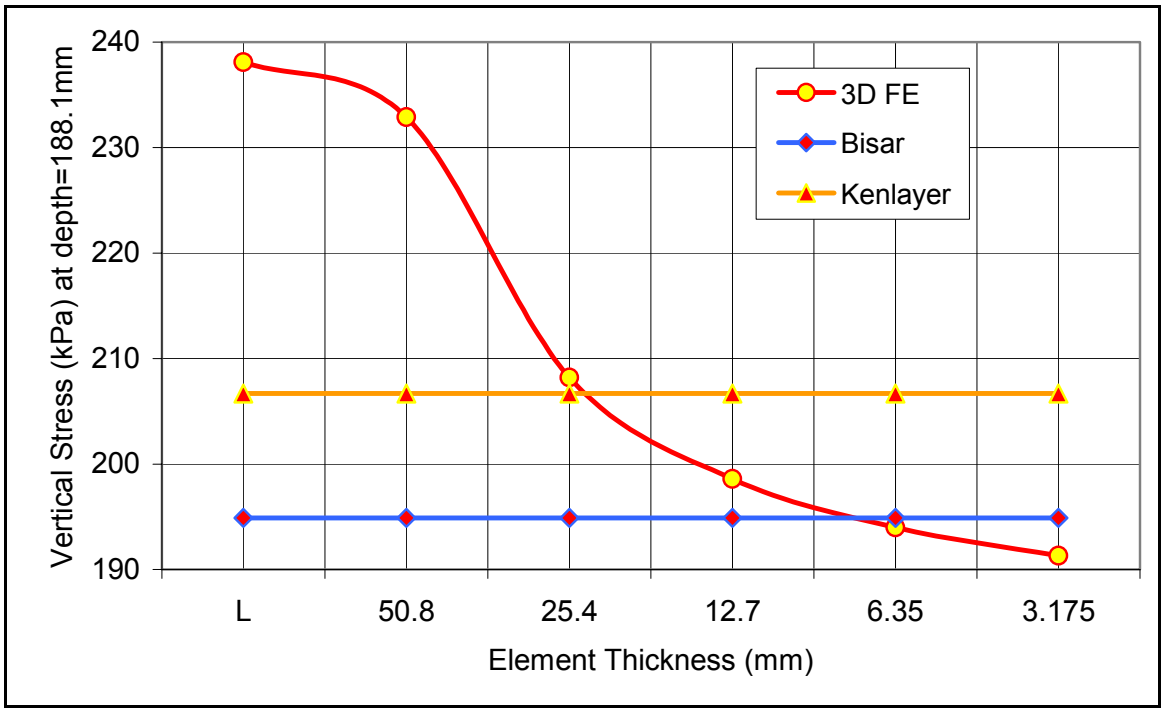

(a)

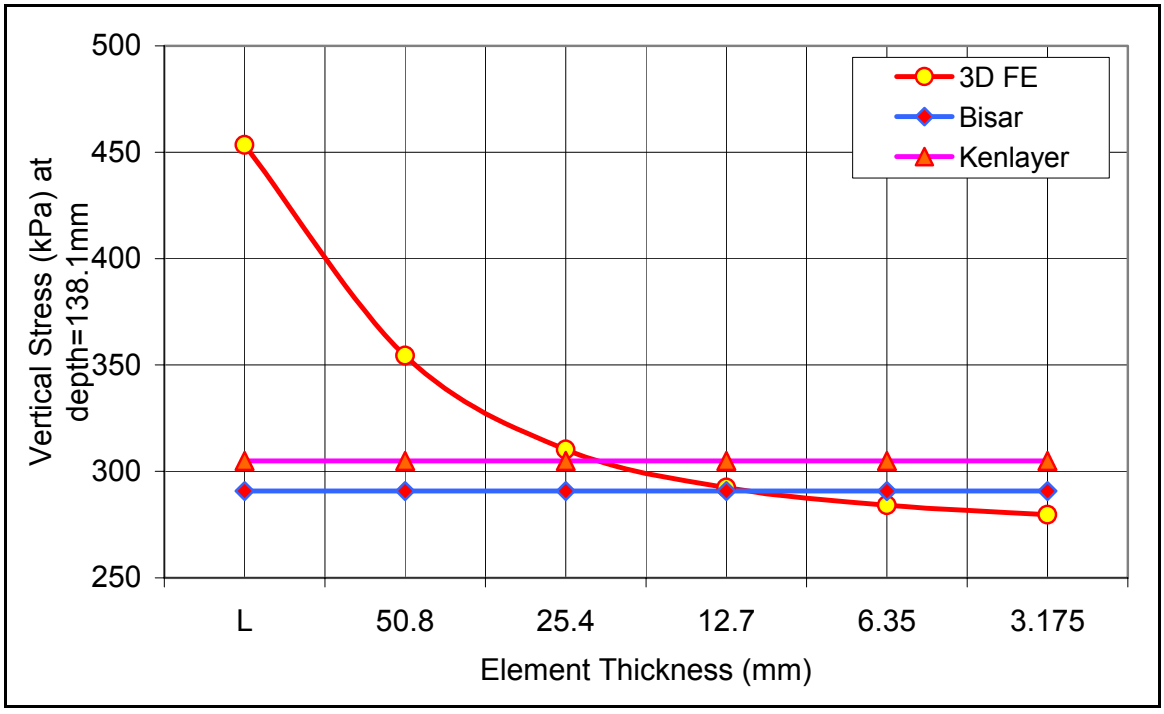

(b)

Figure 4-29. Convergence of the Vertical Stresses with Mesh Refinement

Figure 4-30 illustrates the calculated vertical stresses in Case E using FE, BISAR, and KENLAYER. The percentage of difference between the calculated vertical stresses using FE and those using BISAR were always less than ± 5%, and less than ± 7% using KENLAYER. This correspondence between the FE and the layered theory solutions for this simplified static case establishes the adequacy of the geometry, mesh, and boundary conditions in the FE model.

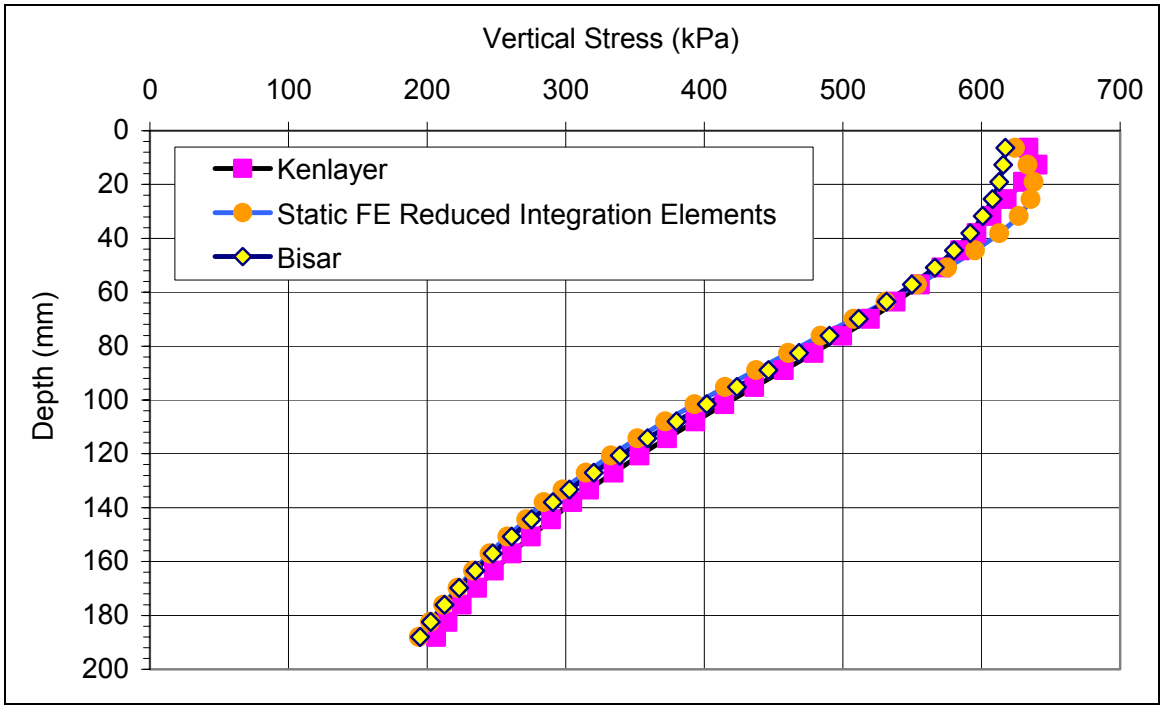

Figure 4-30. Calculated Vertical Stresses Based on the FE Model, the KENLAYER and the BISAR's Solution

Given (a) that the two FE models, Case E and Case F, provide a comparable level of accuracy and (b) that the computational time required for running Case F is more than twice that of running Case E, it was determined that Case E element dimensions would be used for all 3D models in this study. For the three different approaches—BISAR, 3D FE Case E, and KENLAYER—Figure 4-31 illustrates variation in the vertical deflections with the distance from the load. A useful observation regarding vertical deflections is that the calculated displacements did not significantly change with mesh refinement.

This fact allows use of a coarse mesh in the backcalculation process without jeopardizing the level of accuracy. Since a regular backcalculation process requires at least 20 iterations to obtain an acceptable match between measured and calculated deflections, this potentiality proves highly convenient.

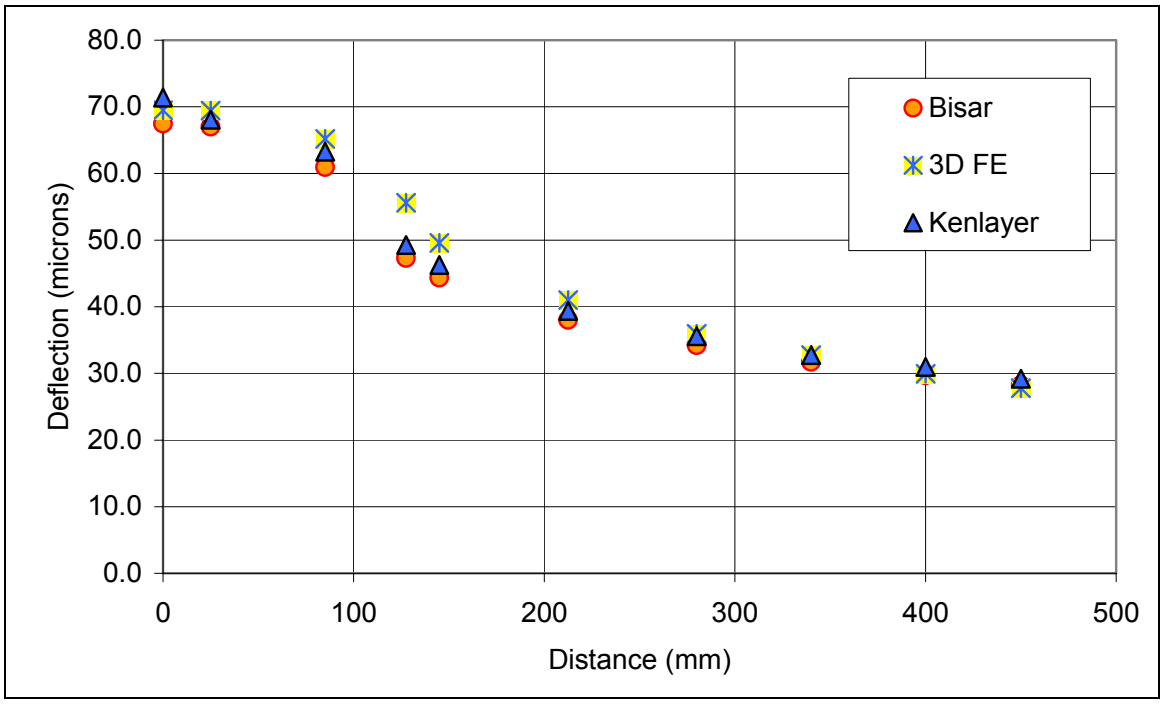

Figure 4-31. Variation of the Vertical Deflections with the Distance from the Load

Finally, Figure 4-32 compares the 3D FE solution (Case E; assuming a single modulus of elasticity for all layers) with Boussinesq's closed form solution; see Equation (4-4). The level of agreement illustrated in Figure 4-32 validates the accuracy of the developed FE model.

4.6.5 Material Characterization

Different materials were used in the pavement structures of sections I and L (see Figures 4-2 and 4-11). To adequately simulate pavement responses to different vehicular loadings, it is essential to characterize the properties of all relevant construction

materials. Material characterization was accomplished using field (backcalculation) and laboratory testing.

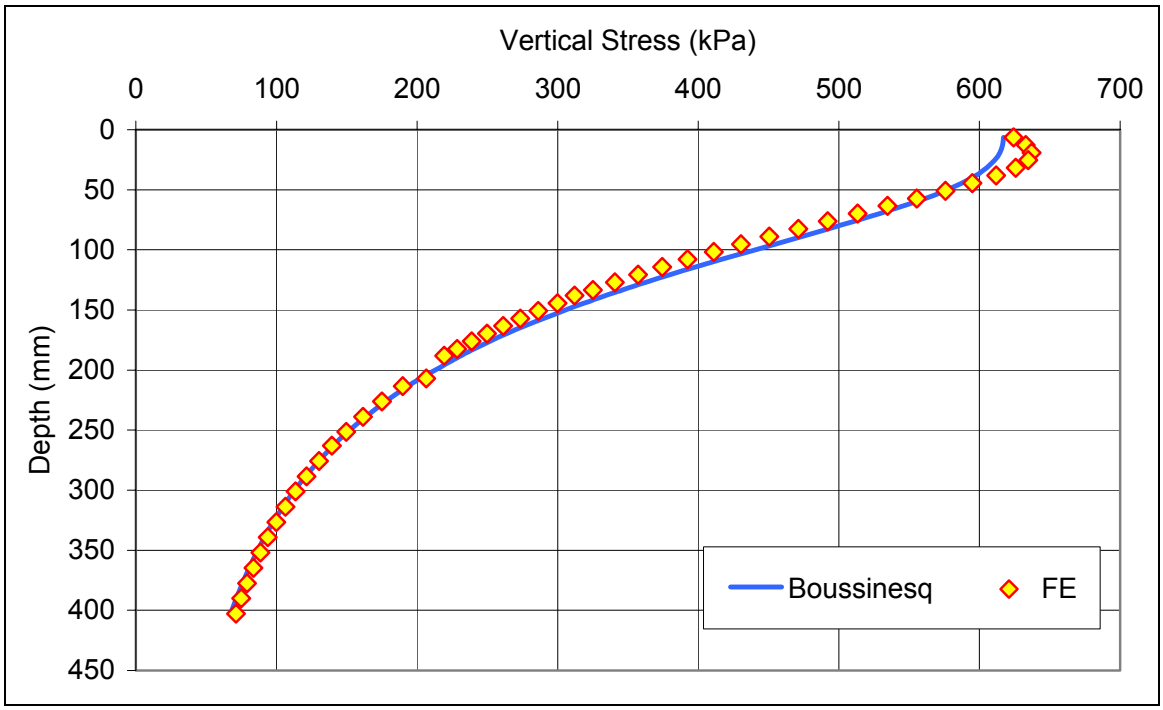

Figure 4-32. Comparison of the 3D FE Approach to Boussinesq's Closed Form Solution

The main objective of this part of the study is neither to compare the two approaches nor to suggest solutions for the discrepancies between them, but rather to select the most appropriate properties for use in FE models. To adequately describe real pavement materials, some properties were assumed for each layer based on the observed responses and the availability of laboratory results. Table 4-6 illustrates the assumed constitutive model for each material, as well as the source of information. The strategy used in the material characterization process consists of the following steps:

- Adoption of the laboratory results for the HMA at the three different temperatures of interest (5, 25, and 40°C).

- Evaluation of the remaining layer moduli (i.e. drainage, base, and subbase layers, and subgrade) based on field backcalculation. Since an elastic constitutive model was assumed for these materials, their behavior was not expected to change with temperature or loading time.
- Evaluation of the HMA layer moduli from field backcalculation in order to validate the accuracy of the backcalculation iterative process.

Table 4-6. Assumed Behaviors in the Developed FE Models

Layer	Actual Behavior	Material Model	Source of Information
Surface Mix (SM)	Elastic Viscoelastic Visco-Elasto-Plastic	Elastic Viscoelastic	Lab
Base Mix (BM-25.0)	Elastic Viscoelastic Visco-Elasto-Plastic	Viscoelastic	Lab
Base Mix (Surface Mix)	Elastic Viscoelastic Visco-Elasto-Plastic	Viscoelastic	Lab
Drainage Layer (OGDL)	Elastoplastic	Elastic*	Field
Cement-Treated Base (21-A)	Elastoplastic	Elastic*	Field
Granular Subbase (21-B)	Elastoplastic	Elastic*	Field
Subgrade	Elastoplastic	Elastic*	Field

* Restrained by availability of laboratory information.

The following sections provide a brief description of each material characteristic. These results eventually were used to provide guidelines for the backcalculation procedure. In this project, the subgrade consists of two types: (a) a limestone large size (>50mm) aggregate fill in sections A through G, and (b) sandy silt cut in sections H through L. Characterization of the subgrade relied mainly on field evaluation performed using

Falling Weight Deflectometer (FWD) deflection measurement directly on top of the subgrade, as well as after construction was completed. Three methods were used for subgrade field evaluation: Boussinesq's approach, MICHBACK backcalculation software, and FE.

The first method, which relied on an exact solution based on Boussinesq's equation for a point load, showed that deflections obtained using this equation are, for practical purposes, equivalent to those obtained for a distributed load involving distances r larger than twice the radius from the center (Ullidtz 1987). The subgrade modulus can be estimated as follows:

$$E = \frac{P(1-\mu^2)}{[\pi r d_o(r)]} \tag{4.12}$$

where

E = subgrade modulus (MPa);

P = applied load (N);

μ = Poison's ratio (assumed 0.4 for the subgrade);

r = distance from the center of the load; and

$d_o(r)$ = surface deflection at distance r.

Using deflections away from the center, a more confident subgrade modulus can be obtained by reducing the uncertainty to the assigned Poisson's ratio value, which normally ranges from 0.3 to 0.45. Evaluating the subgrade moduli using different deflections also serves as confirmation of the assumption that the subgrade is a linear, elastic, semi-infinite space. If this assumption holds true, the estimated moduli at a different distance r from the load must be identical. Otherwise, a stiff layer should be included in the analysis, or a non-linear subgrade modulus should be considered (stress-dependent moduli). Figure 4-33 illustrates the calculated subgrade moduli for Section L, using Equation (4.12) for both the small (radius=150mm) and large plates (radius=228mm). As shown in this figure, the assumption that the subgrade is a linear

elastic semi-infinite space holds true for this section, as the estimated subgrade modulus was relatively constant with the distance from the load. This finding indicates that the presence of a stiff layer in this section is negligible, and the assumed foundation stiffness in the FE model should reflect a low level of resistance.

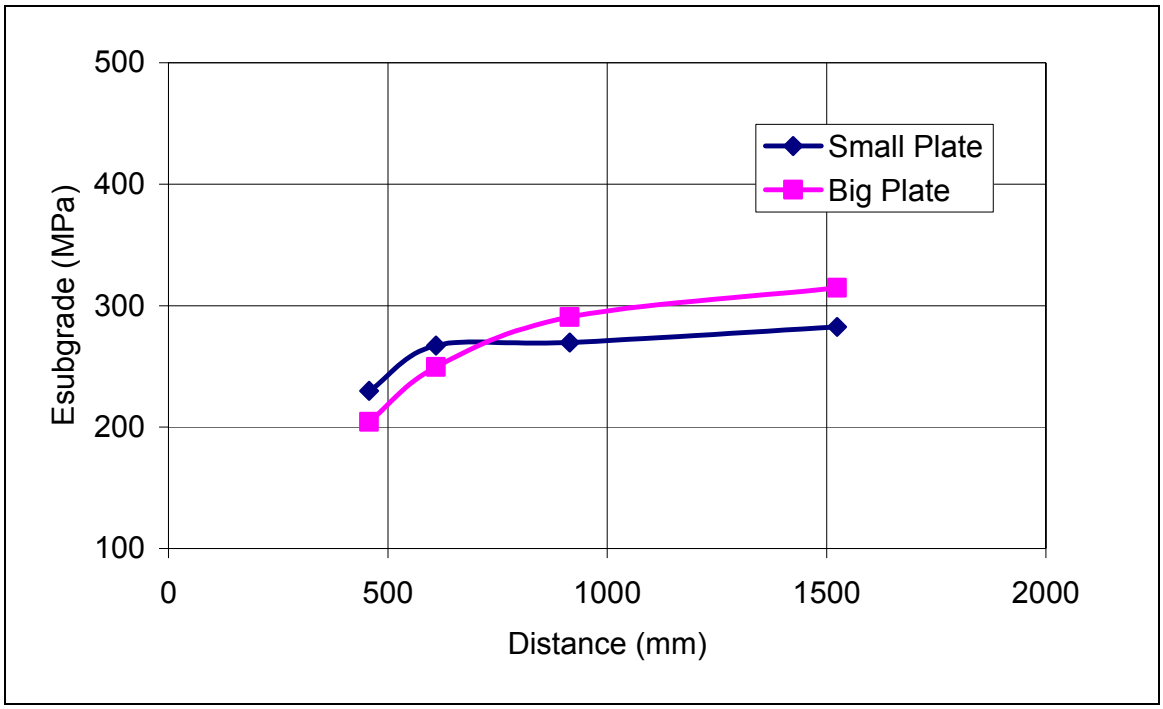

Figure 4-33. Estimated Subgrade Moduli using Boussinesq's Approach for Section L

In contrast, Figure 4-34 shows the calculated subgrade moduli for Section I. As shown in this figure, the assumption that the subgrade is a linear elastic semi-infinite space does not hold true for this section, as the estimated subgrade modulus decreased more than two orders of magnitude between the closest and furthest valid sensors to the load. This indicates the necessity of considering the influence of bedrock on the deflection measurements obtained from atop the upper layers.

The second method relied on the backcalculation analysis: it estimated the subgrade modulus as part of the unknown moduli using MICHBACK, version 1.0

(Harichandran et al. 1994). In this method, a rigid layer can be included in the analysis to realistically simulate the actual situation.

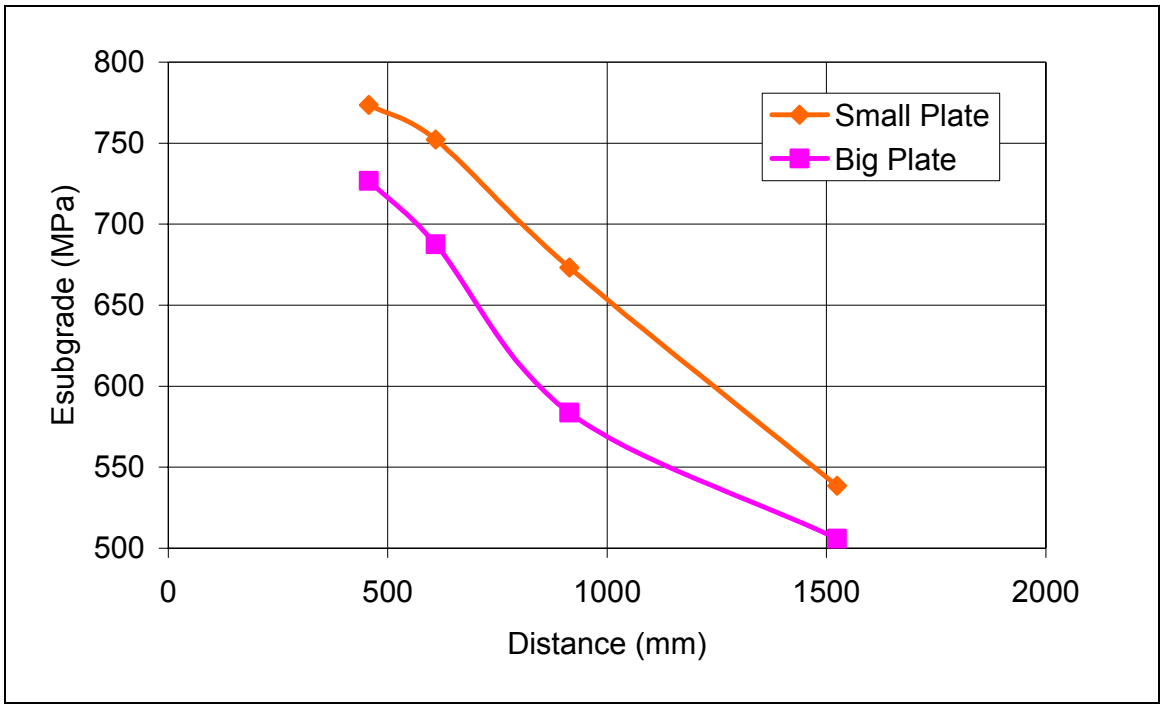

Figure 4-34. Estimated Subgrade Moduli using Boussinesq's Approach for Section I

Figure 4-35 compares the two methods for sections I and L, with the number in parentheses indicating the estimated depth (m) of the stiff layer. As shown in this figure, the depth of the stiff layer in Section L was 18.2m, high enough that it should not influence the estimated modulus. As this figure indicates, the two methods agreed in this section due to the absence of a significant stiff layer.

The third method relied on backcalculating the pavement structure using FE, which will be explained in more detail in the following sections. Based on the results of the three methods, a subgrade modulus of 310MPa was chosen for Section I and one of 260MPa for Section L.

Based on the AASHTO classification, the 21-B granular material is classified as A-1-a, which corresponds to GP-GM in the United Classification System and describes a material consisting predominantly of stone fragments or gravel. Laboratory evaluation of the modulus of resilience (M_r) was performed.

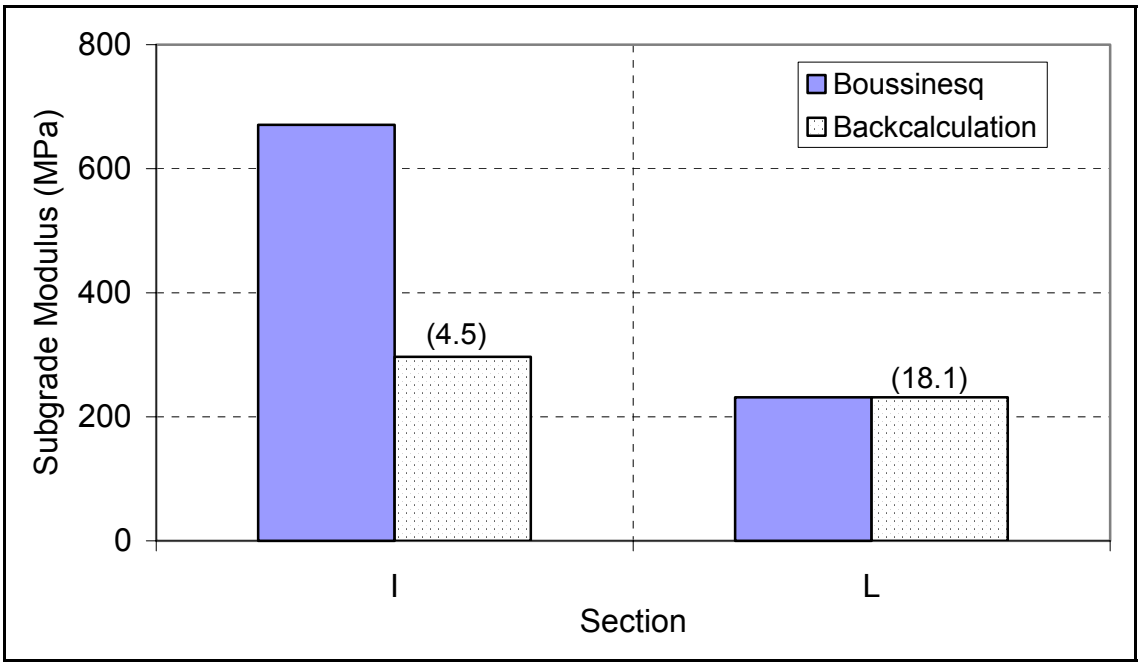

Figure 4-35. Comparison between Boussinesq's Approach and the Backcalculated Moduli

For this test, a specimen of 21-B aggregate is placed in a triaxial cell and an initial confining pressure is applied. The specimen is then subjected to 100 cycles of cyclic deviator stress, and the test is repeated for several combinations of confining pressure and cyclic deviator stress. Such combinations simulate the load conditions on a typical road under regular traffic. Based on testing, it was found that this layer is better represented by a stress-dependent behavior with a relation between the modulus of resilience and its stress invariant:

$$M_R = 7304\ \theta^{0.6} \tag{4.13}$$

where

M_R = modulus of resilience in kPa; and

θ = stress invariant obtained by

$$\theta = \sigma_1 + \sigma_2 + \sigma_3 = \sigma_1 + 2\sigma_3 \tag{4.14}$$

For the standard FWD load (40kN), an approximate stress invariant of 965kPa can be easily calculated, resulting in a modulus of resilience of 210MPa. To describe the 21B aggregate layer using an elastoplastic model, it is necessary to perform triaxial testing to failure, which was not done in this study.

The 21-A cement-treated base consists of the 21-A aggregate mixed with 3.5 percent cement. The key to strength development in the stabilized subbase mixture is in the matrix used to bind the aggregate particles. This mix results in a strong material that exhibits a behavior close to plain concrete, in that it gains strength with time and proves highly susceptible to shrinkage cracking. Samples from the 21-A cement stabilized base were obtained during installation and placed in plastic cylindrical molds (101mm x 202mm). Specimens were tested in compression after 1, 3, 10, 14, 21, 28, and 50 days in two replicates. Based on the correlation charts between the unconfined 7-day compressive strength and the resilient modulus (Huang 1993), an approximate value of 3585MPa was estimated for the modulus of resilience based on laboratory testing. However, it should be emphasized that this material—which is cement-treated—gains strength with time, similar to Portland cement concrete.

Drainage layers are usually designed to meet specified permeability, strength, and construction stability. Generally, these mixes contain very little or no fine aggregate. An asphalt-treated drainage layer and a cement-treated drainage layer were installed in sections I and L, respectively. No laboratory results were available for this type of material.

A base mix (BM), sometimes called a binder course, is the layer located immediately beneath the surface mix. This type of mix is preferred over a regular surface mix for several reasons. First, it proves more economical: it uses an aggregate source of less quality than the one used for the surface mix. It also better meets construction specifications that the surface mix not be too thick to be placed and compacted in a single layer. In addition, a mix with large aggregate usually provides more resistance to rutting, but is characterized by its rough surface. The mix design for the BM-25.0 is presented in Table 4-7. Laboratory testing for this mix will be explained in more detail in the following sections.

Table 4-7. Mix Design for BM-25.0

Sieves	% Passing	Specification Range
37.5mm	100	100
25mm	97.6	90-100
19mm	89.9	Max 90
2.36mm	32.8	19-45
0.075mm	6.5	1-7
Asphalt Content	5.1	Min 4.0

The surface mix is the top course of a flexible pavement structure, also called the wearing surface. It is the only layer that comes in direct contact with the traffic; therefore, the use of adequate and dense-graded design mixes is common practice. The mix-designs for SM-9.5A* (high compaction), SM-9.5A, and SMA-12.5 are presented in Table 4-8.

Table 4-8. Mix Design for the Surface Mix Used in Sections I and L

Sieves	SM-9.5A	SM-9.5A*	SMA-12.5
19.0mm	(100)	(100)	(100)
12.5mm	(100)	(100)	(88-98)
9.5mm	(86-94)	(86-94)	(65-75)
4.75mm	(52-60)	(52-60)	(23-29)
2.36mm	(30-38)	(30-38)	(17-23)
0.6mm	----	----	(12-18)
0.075mm	(5-7)	(5-7)	(8-12)
Asphalt Content	5.4 (5.3-5.9)	5.2 (4.5-5.1)	6.8 (6.90-7.50)

4.6.5.1 Laboratory Characterization of Hot-Mix Asphalt

Hot-mix asphalt (HMA) is a visco-elasto-plastic material characterized by a certain level of rigidity in its elastic solid body, but, at the same time, it dissipates energy by frictional losses as a viscous fluid. As with any viscoelastic materials, HMA's response to stress is dependent on both temperature and loading time. At high temperatures or under slow

moving loads, HMA may exhibit close to pure viscous flow and is best simulated as a nonlinear visco-elasto-plastic material. However, at low service temperatures or rapid applied loading, HMA behaves as a linear elastic or viscoelastic material. Elastic and plastic properties of HMA may be characterized using the modulus of resilience test (ASTM D4123-82) and the creep compliance test, respectively. A brief description of each test, the governing equations, and how the results of each test may be incorporated into the FE models follow.

The resilient modulus test is used to determine the elastic properties of HMA (modulus of elasticity [E] and Poisson's ratio [ν]) at different loading times and temperatures. For HMA, the diametral indirect tensile test is considered one of the most popular and reliable means of evaluating these properties (Hugo and Schreuder 1993). This test consists of subjecting a cylindrical specimen to a compressive haversine loading in durations of 0.1sec, with rest periods of 0.9sec. With this loading pattern, a relatively uniform tensile stress may be assumed along the vertical diameter of the sample. After a conditioning step (100 to 200 cycles), the permanent deformation is assumed to reach an asymptotic level, and all the strain is assumed recoverable. The elastic modulus is then defined as follows:

$$M_R = \frac{\sigma}{\varepsilon_r} \tag{4.15}$$

where

M_R = Modulus of resilience (elasticity);

σ = deviator stress; and

ε = recoverable strain.

The resilient modulus test was performed at three temperatures—5, 25, and 40°C —for all types of HMA used in this project, except the open-graded friction course used in section K. Table 4-9 illustrates test results. To define the instantaneous response of a

viscoelastic material, ABAQUS requires the definition of the elastic modulus at the temperature of interest.

Table 4-9. Measured Modulus of Resilience (MPa) in the Laboratory for Field Cores

Mix Type	Temperature = 5°C		Temperature = 25°C		Temperature = 40°C	
	Resilient Modulus	Poisson's Ratio	Resilient Modulus	Poisson's Ratio	Resilient Modulus	Poisson's Ratio
SM-9.5A	11980	0.22	3525	0.33	1595	0.36
SMA-12.5	5050	0.25	2195	0.37	1200	0.40
SM-9.5A*	12635	0.22	4880	0.35	2315	0.42
BM-25.0	9110	0.23	3530	0.30	1795	0.35

"Creep" involves the time dependent deformation properties of materials under constant stress. The basic information obtained from a creep test is the accumulation of creep strain with time at a specific load and temperature. To determine the creep properties in the lab, the diametral (indirect tensile) test was utilized to apply a constant compressive load to a cylindrical specimen for a specified period of time; 1000sec was adopted in this study. Such a loading condition creates over the central portion of the diametral plane a nearly uniform compressive-tensile stress field (Zhang et al. 1997). During the test, the applied constant stress and the resulting strains are measured over time. Creep compliance of the material is then calculated as follows:

$$D(t) = \frac{\varepsilon(t)}{\sigma_0} \tag{4.16}$$

where

D(t) = creep compliance at time t;

ε(t) = measured strain at time t; and

σ_0 = constant stress applied to the sample.

To describe the viscoelastic behavior of a material, ABAQUS assumes that a Prony series expansion adequately describes the material response with respect to time:

$$K(t) = K_0\left(1 - \sum_{i=1}^{N} K_i\left(1 - e^{-t/t_i}\right)\right) \tag{4.17}$$

where

K(t) = bulk modulus at time t; and

K_0 = instantaneous bulk moduli determined from the elastic modulus as follows:

$$K_0 = \frac{E_0}{3(1 - 2\nu_0)} \tag{4.18}$$

where

E_0 = elastic modulus; and

ν_0 = Poisson's ratio.

ABAQUS offers the option to automatically calculate Prony series parameters based on the results of the creep compliance test. In this case, experimental data are obtained by performing creep compliance tests at different temperatures, then shifting the data to a reference temperature—for this study, 5, 25, and 40°C—in order to establish one smooth curve known as the master curve. As an example, Figure 4-36 illustrates the constructed master curve for the surface mix in Section I at a reference temperature of 25°C. The construction of these curves is based on the assumption of the validity of the time-temperature superposition principle. The small graph presented in this figure indicates the required shifting for the master curve from temperature T to reference temperature T_r based on the following relation (Williams, Landel, and Ferry [WLF] equation; Ferry 1980):

$$h(T) = -\log a_T = \frac{A(T - T_r)}{B + (T - T_r)} \tag{4.19}$$

where

a_T = shift factor from temperature T to reference temperature T_r; and

A and B = numerical constants.

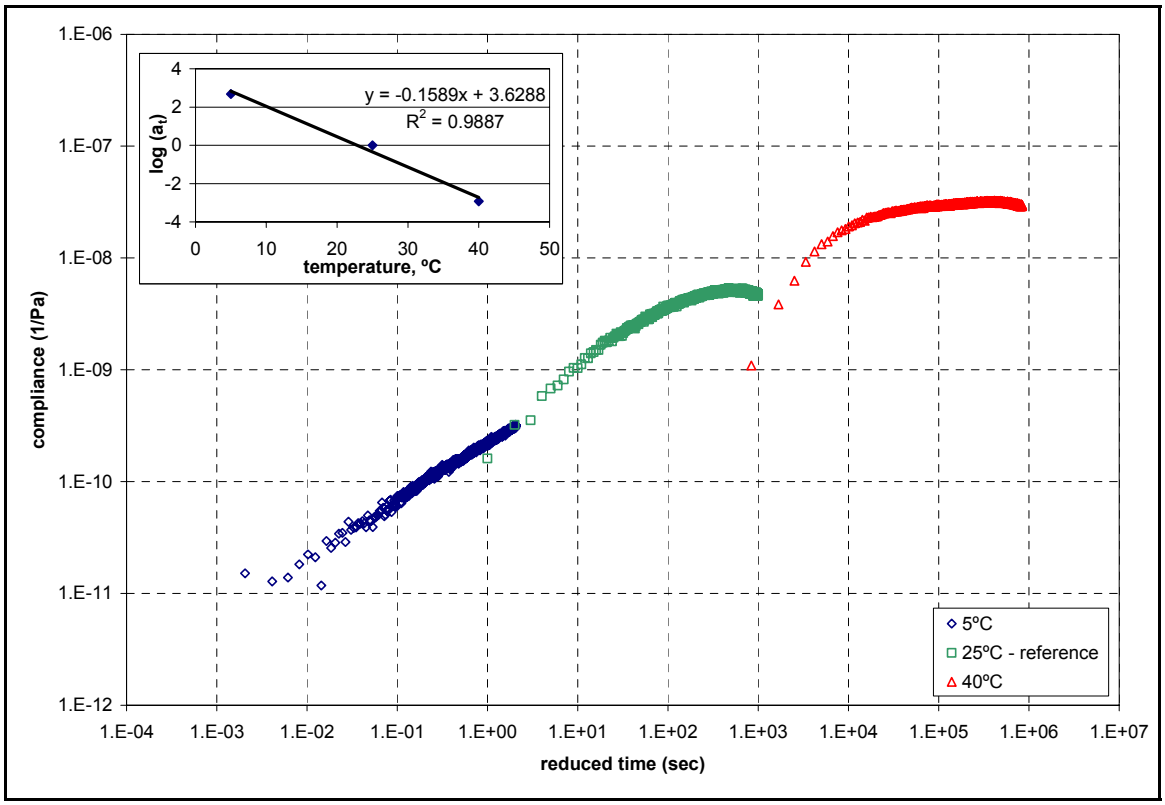

Figure 4-36. Master Curve for Surface Mix in Section I

As shown in Figure 4-36, significant variance and scattering in the creep data are observed. This makes it difficult to directly fit a Prony series model to the experimental data and results in convergence difficulties in the nonlinear regression procedure. To avoid such problems, the measured creep compliances were first fitted to a modified power law (MPL) model (Kim et al. 2002):

$$D(t) = D_0 + \frac{D_\infty - D_0}{\left(1 + \frac{\tau_0}{t}\right)^n} \quad (4.20)$$

where

D_0 = glassy creep compliance (at short loading times and/or low temperatures);

D_∞ = long loading time compliance at $t=\infty$;

$D(t)$ = creep compliance; and

τ_0 and n = positive constants.

The MPL model reportedly provided a good approximation of the creep compliance behavior, especially in the constant slope region (see Figure 4-37, for example). Normalized creep compliances were then provided to ABAQUS, from which a Prony series (see Equation 4.17) was fitted to the adjusted experimental data. This process significantly reduces the convergence difficulties in fitting the creep compliance data, resulting in a root mean square error (RMSE) of less than 10% in all cases. Appendix C presents more details about the fitting process for the mixes of interest in this study.

4.6.5.2 Backcalculation of Material Properties Using Finite Element Analysis

Not all the properties of the required materials were characterized in the laboratory, so field evaluation or backcalculation of layer moduli was necessary to obtain the missing data. Due to the general complexity of the pavement structures at the Virginia Smart Road, and given the fact that most backcalculation software (e.g. MICHBACK) can handle a maximum of five layers while the pavement structure in Section I consists of seven layers, evaluation of the pavement moduli mainly relied on backcalculation using the FE method. This method has proven very accurate and reliable for composite pavements (Shoukry et al. 1999). In this iterative procedure, the layer moduli are changed until an acceptable match between measured and calculated deflections is obtained.

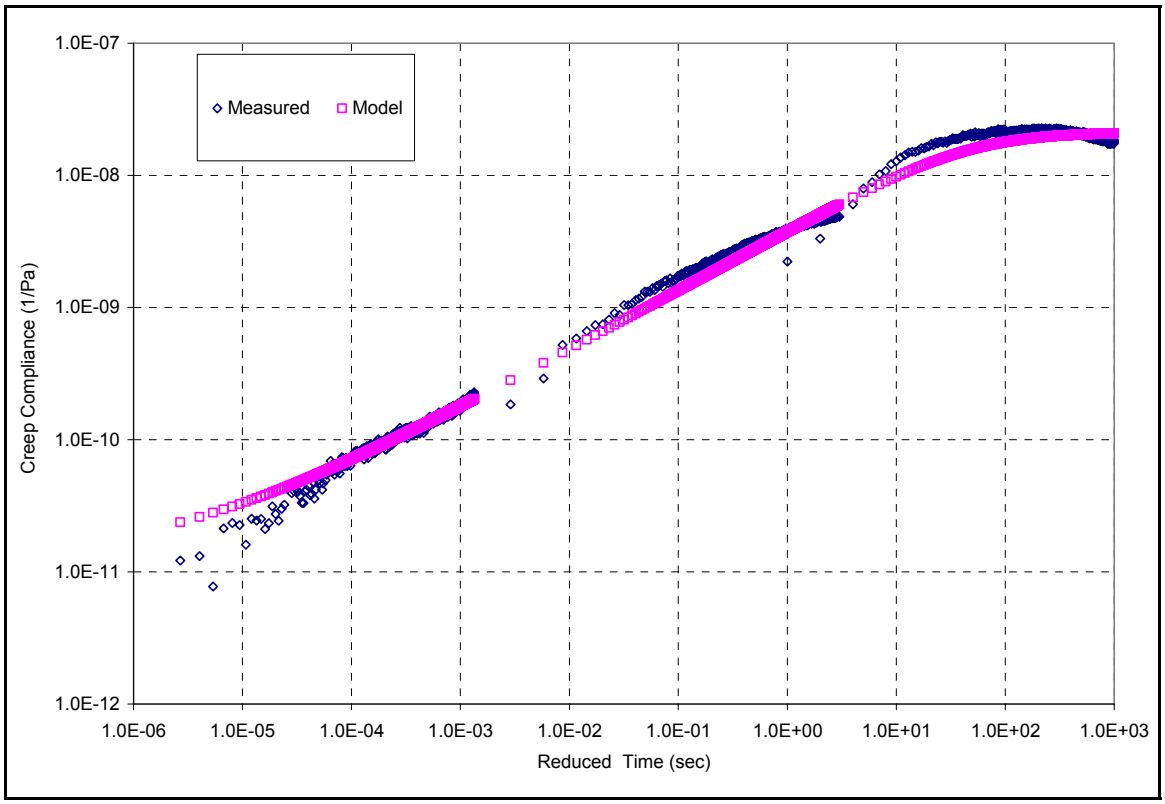

Figure 4-37. Fitted Power Law Model to the Creep Compliance at 40°C

It is important to understand that the solution for this problem is not unique and that engineering expertise is sometimes required. This procedure was performed for the non-instrumented lane in each section of interest. The major advantage of this procedure is that backcalculation can be accomplished without consideration of the interlayer system (steel reinforcement was only installed in the instrumented lane). The FE model can then be modified to incorporate the interlayer system and to evaluate its effect on the calculated vertical deflections. Since the comparison of various constitutive models with laboratory testing is outside the scope of this study, all material behaviors in the backcalculation procedure were assumed to be linear elastic. HMA was modeled as a linear viscoelastic in the FE analysis to simulate pavement responses to vehicular loading.

All the assumptions previously stated in the modeling process overview were followed in the developed model (see Section 4.6.3). However, due to symmetry in both directions (X and Y), only a quarter model was considered to increase the modeled

distance in one side of the load (see Figure 4-38). The FWD loading was simulated as an approximate quarter of a circle (symmetry of loading). Due to elements' geometry, some truncations in the actual circle perimeter were necessary but the total area was approximately equal to the actual area of the FWD loading plate (see Figure 4-39).

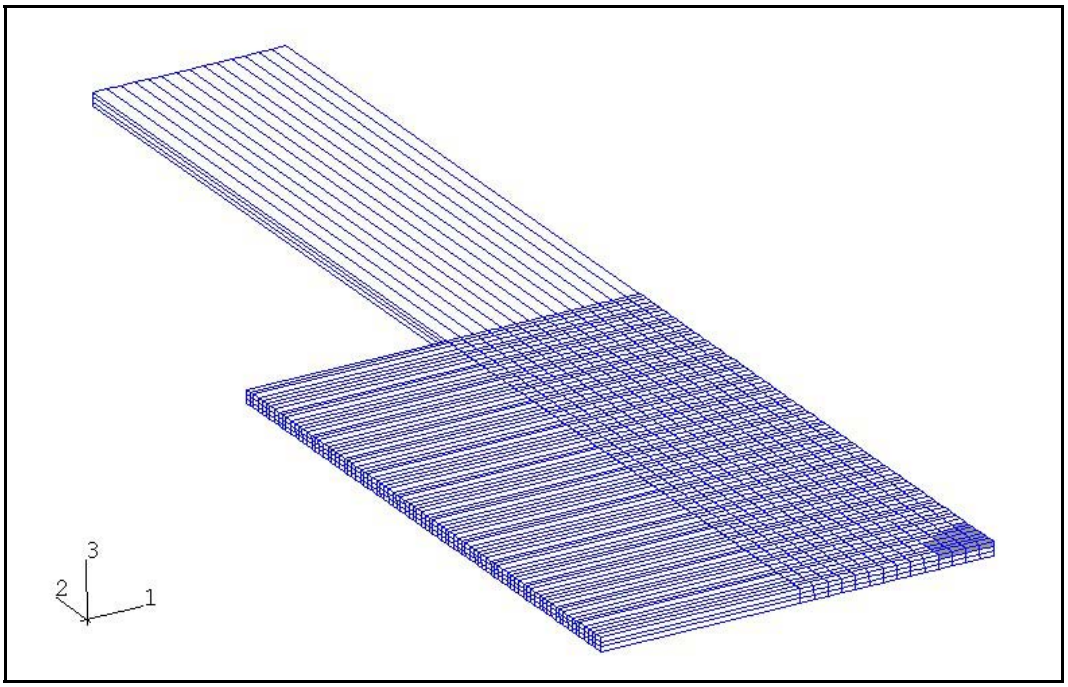

Figure 4-38. General Layout of the Developed Model for FWD Backcalculation

One set of measured deflections was used in back calculating the respective layer moduli for each section of interest (sections I and L). After discarding the transition zone (10m) from the ends of each section, each set represents the average of all measurements in the non-instrumented lane on May 30th 2000 (T=23°C). The general strategy used in the backcalculation process consisted of first assigning a subgrade resilient modulus close to the one obtained by MICHBACK. The foundation stiffness was then gradually adjusted to obtain an acceptable match for the last sensor measurements, which usually are assumed to be the function of only the subgrade condition. Finally, adjustment of the other layer moduli was accomplished to achieve an acceptable fit for the measured deflection basin. In general, at least 20 iterations were needed to accomplish this process.

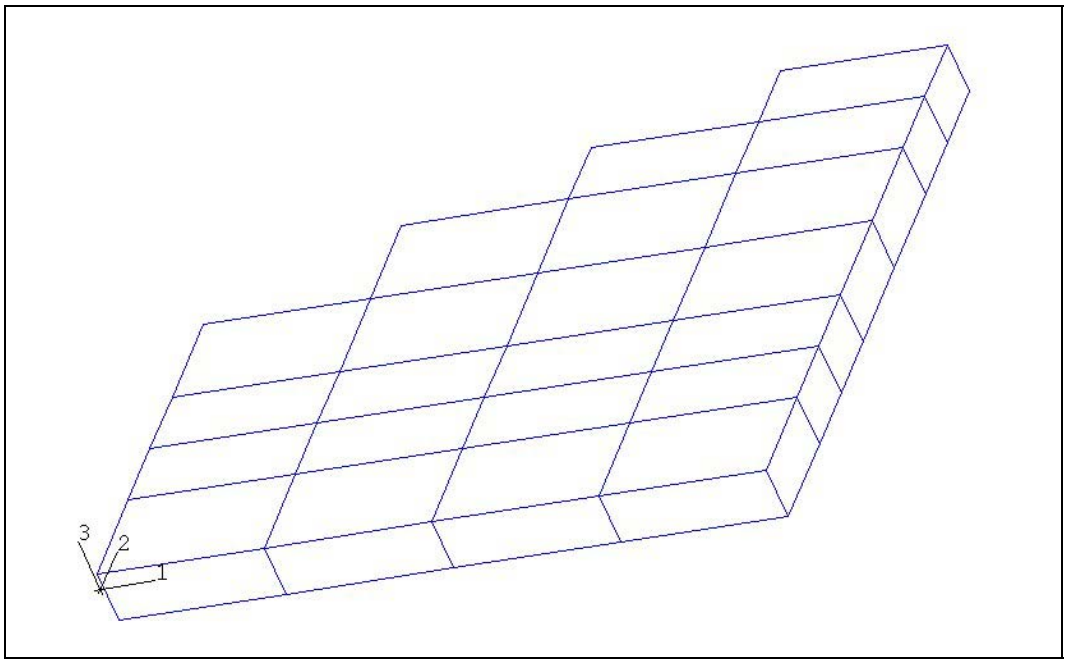

Figure 4-39. Simulation of the FWD Loading Plate

Figure 4-40 (a) and (b) illustrate the comparison between the measured and calculated surface deflections for sections I and L. This corresponds to a RMSE of 10% for Section I and 9.0% for Section L, a relatively low percentage of error given the complexity of the pavement structure. Table 4-10 illustrates the backcalculated moduli for sections I and L, as well as any reported measured resilient moduli for the HMA at the temperature of interest. Based on these results, the following observations can be made:

- The cement-treated drainage layer in Section L was substantially affected by the difficulties encountered during installation. A low modulus of 550MPa was back calculated for this layer in Section L. It should be noted that the major problem encountered during installation was the repetitive passage of heavy equipment before the material had completely set. Also, note that regular backcalculation software encounters some difficulties in accurately estimating the moduli of thin layers (less than 75mm).

- The laboratory resilient moduli at the temperature of interest (23°C) were obtained assuming an exponentional fit for the measured values previously shown in Table 4-9, as follows:

$$E = C_1 \exp(C_2 * T) \tag{4.21}$$

where

E = modulus of resilience at any temperature T (MPa);

T = temperature (°C); and

C_1 and C_2 = fitting constants.

- There was reasonably good agreement between the FE solution and the laboratory measured resilient moduli for most of the layers; however, some discrepancies can be noticed, especially in the thin (less than 75 mm) HMA layers of Section I.

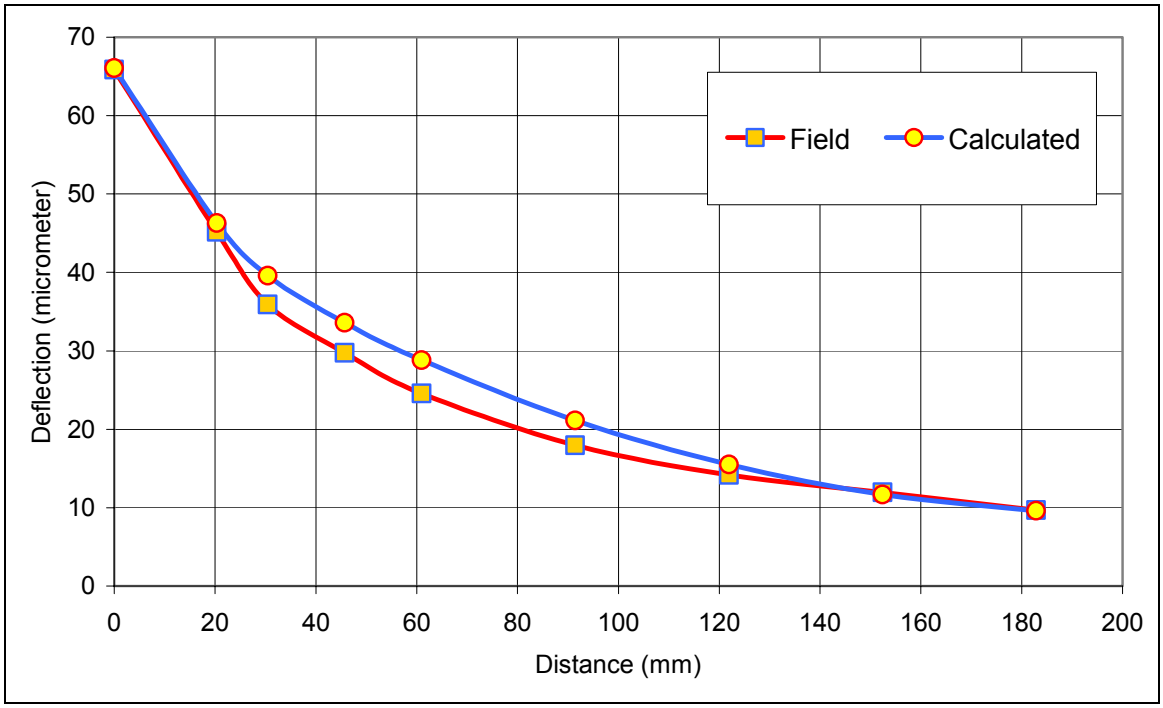

(a)

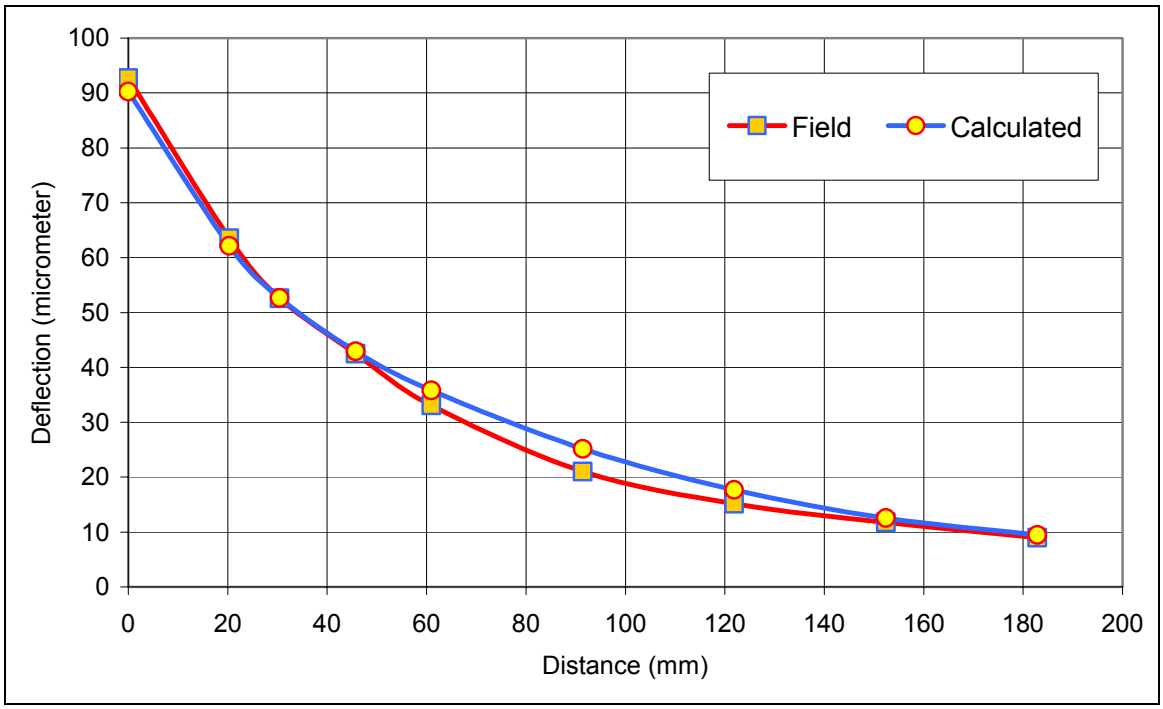

(b)

Figure 4-40. Comparison between the Measured and Calculated Vertical Deflections for (a) Section I and (b) Section L.

Table 4-10. Backcalculated Layer Moduli for Sections I, and L at the Virginia Smart Road (Temperature = 23°C)

Section	SM	BM-25.0	SM-9.5A	OGDL	21-A	21-B	Subgrade	Found. Stiff. (N/cm^3)
Backcalculated Moduli (MPa)								
I	3795	5860	3795	2415	13445	305	310 (296)	260
L	3100	4485	----	550*	10340	305	260 (231)	175
Laboratory Measured Moduli (MPa)								
I	5315	3925	4150	NA	NA	210	NA	----
L	2400	3925	----	NA	NA	210	NA	----

* Cement-treated drainage layer (see section 4.4.2)

NA: Not Available

4.6.6 Three-Dimensional Finite Element Model for Simulation of FWD Testing

Section 4.5 presented the conceptions that based on FWD measurements, mesh contribution to the vertical deflection was marginal, and that it was manifested only at high temperatures for one of the three mesh types. To investigate these experimental findings, the study incorporated steel reinforcement into the FE model previously used in the backcalculation process (see Figure 4-41).

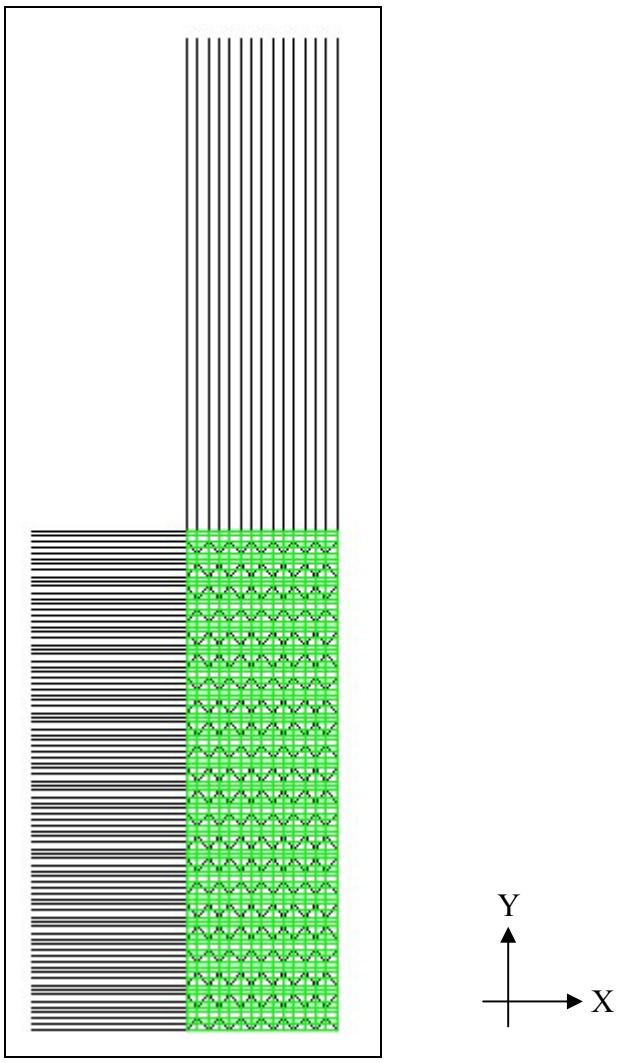

Figure 4-41. General Layout of the Developed Model (Section I)

Steel reinforcement was simulated as a non-homogeneous layer with openings. For each type of mesh, geometries of the openings were accurately simulated. Three-dimensional beam elements—2-node linear beam B31 and 3-node quadratic beam B32—were used to simulate the mesh wires with circular or rectangular cross-sections, depending on the mesh type. The reinforcement pattern and geometry for each type are different (see Figure 4-42). Both mesh types used in Section I are transversally reinforced at regular intervals with circular steel wires. In contrast, the steel mesh used in Section L is transversally reinforced at regular intervals with torsioned flat-shaped steel wires.

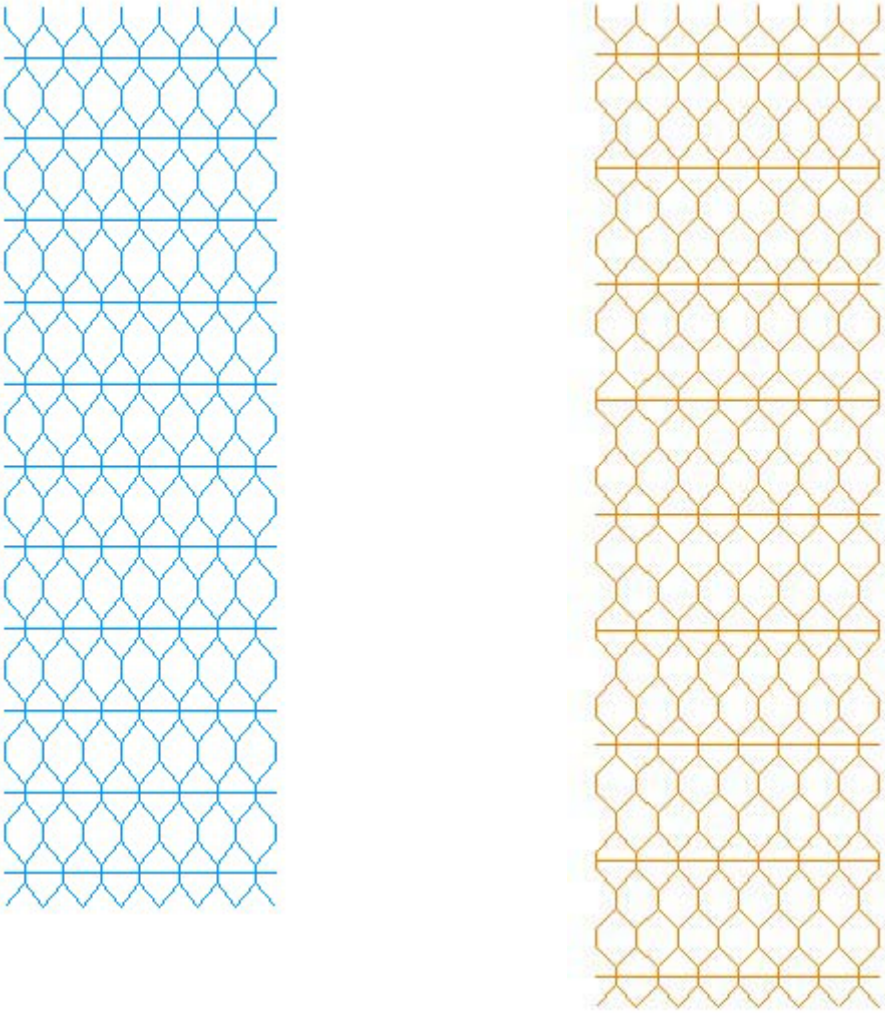

Section I Section L

Figure 4-42. Simulation of the Steel Reinforcement for Sections I and L

At the temperature of interest (23°C), previously selected material properties were adopted for both the reinforced and non-reinforced models. Table 4-11 compares such vertical deflections for reinforced and non-reinforced cases in both sections (I and L). As shown in this table, for the pavement structures under consideration and at this temperature, the steel reinforcement contribution to the vertical deflections is minimal. These findings confirm both field and statistical results.

Table 4-11. Pavement Surface Deflections for Unreinforced and Reinforced Cases

Deflections (microns) / Distance (mm)	Section I		Section L	
	Unreinforced	Reinforced	Unreinforced	Reinforced
0.00	63.9	63.8	90.2	89.9
20.32	46.3	46.2	62.1	61.9
30.48	39.6	39.6	52.6	52.5
45.72	33.3	33.3	42.9	42.9
60.96	28.4	28.4	35.8	35.7
91.44	20.6	20.6	25.1	25.1
121.92	15.0	15.0	17.6	17.6
152.40	11.2	11.2	12.5	12.5
182.88	9.2	9.2	9.5	9.5

4.6.7 Three-Dimensional Finite Element Model for Simulation of Vehicular Loading

4.6.7.1 Background

Data acquisition systems installed at the Virginia Smart Road were used to monitor the pavement-embedded instrument responses to different loading and environmental conditions. Hence, two categories of data were collected:

- **Dynamic measurements**: These represent the effect of traffic loading on the different pavement layers, which can be presented by pressure and strain. This type of data was collected as a pulse at a specific sampling frequency. Dynamic data was stored when the pressure (or strain) exceeded a predefined trigger value, dependent on the instrument type and position.
- **Static measurements**: These represent environmental effects on the different pavement layers. This type of data was collected at specific time intervals: 15min for temperature; one hr for moisture; and 6 hrs for frost depth.

Every two adjacent sections were monitored by a single data acquisition system, which was in turn controlled by a computer located inside an underground bunker. To minimize the number of files collected and then transferred for analysis, data from the two sections were combined into two categories of files: text files containing static data and binary files containing dynamic data.

Considering the data collection frequencies for dynamic measurements (500Hz) and the large number of instruments used at the Virginia Smart Road, a large amount of data was collected and stored every day. To reduce the amount of collected data, some instruments were inactivated during vehicular loading: vibrating wire strain gauges, and time domain reflectometer, for example.

The truck used for vehicular loading was an International 8200 Class 887 with an engine power of 350hp at 2100rpm. It had Michelin 11R22.5 XZA-1 for the steering axle wheels and General 11R22.5 for the tandem axle wheels. The trailer had Goodyear 10.00R15TR for its tridem axle wheels. Figure 4-43(a) is a photograph of the truck during testing, and Figure 4-43(b) is a schematic showing the axle configuration for the truck and the trailer. The experimental program consisted of three different inflation pressure levels, three different load configurations, and four different speeds. The inflation pressures were 724kPa, 655kPa, and 551.6kPa. The four different speeds were 8km/h, 24km/h, 40km/h, and 72.4km/h.

(a)

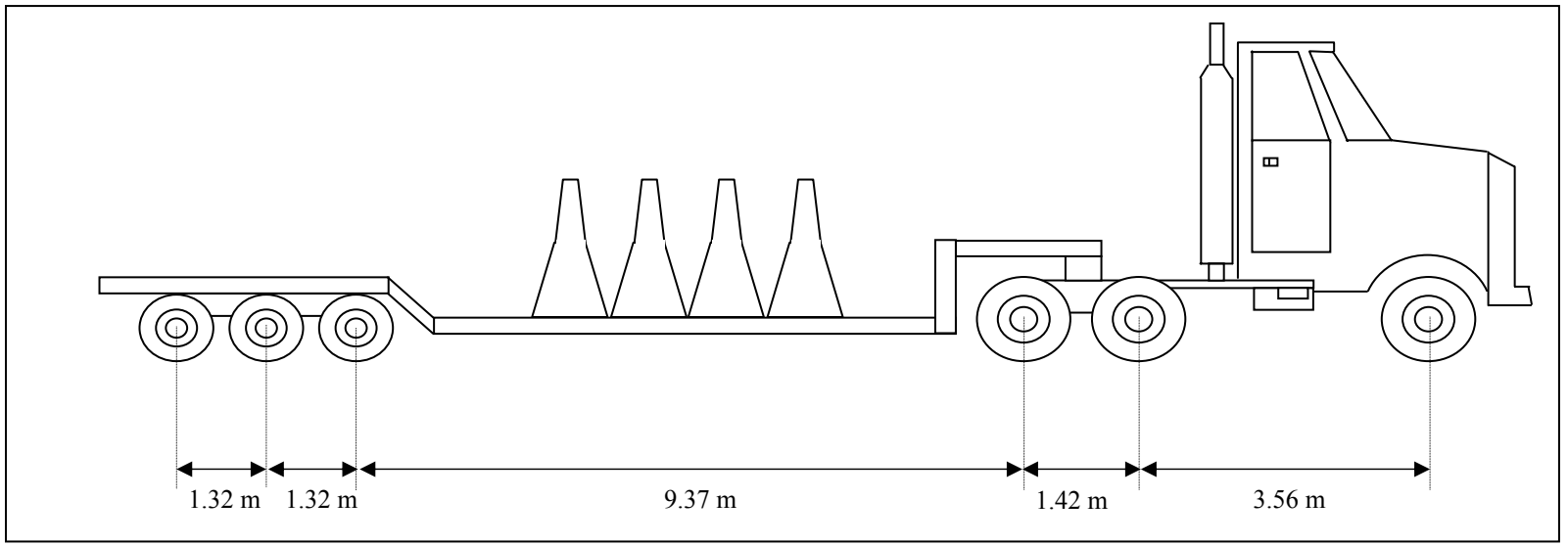

(b)

Figure 4-43. Truck Used for Testing: (a) Photograph while Testing (b) a Schematic of Wheel Configuration

Since other researchers found that the effect of lateral offset—between the center of the tire and the instrument—was very significant (e.g. Chatti et al. 1996), paint was used to mark the position of the instruments. As all dynamic instruments were placed in three lateral positions (0.5m, 1m, and 1.5m from the shoulder), a 10m line was painted at these three lateral positions. Two more 10m lines were painted between the instruments at a distance of 0.75 and 1.25m from the shoulder. Each test—same load, same pressure, and same speed—was performed ten times, twice on each lateral position in order to ensure that the maximum strains and pressures would be measured in at least one of the runs. Data from the GPS unit was saved in a laptop placed inside the truck. In addition, the position of the truck was verified with ultrasonic sensors with respect to the carefully surveyed sensors.

To investigate the effect of different loading levels, three (L1, L2, and L3) were tested (see Figure 4-44). Concrete barrier walls or jersey walls, each of which weighs around 2265kg, were used for loading the truck. Load L1 used nine barrier walls, and Load L2 used four barrier walls. For load L3, no barrier walls were used. With these three considered variables, 36 different tests were conducted. Truck tests were performed every week (Loulizi et al. 2001).

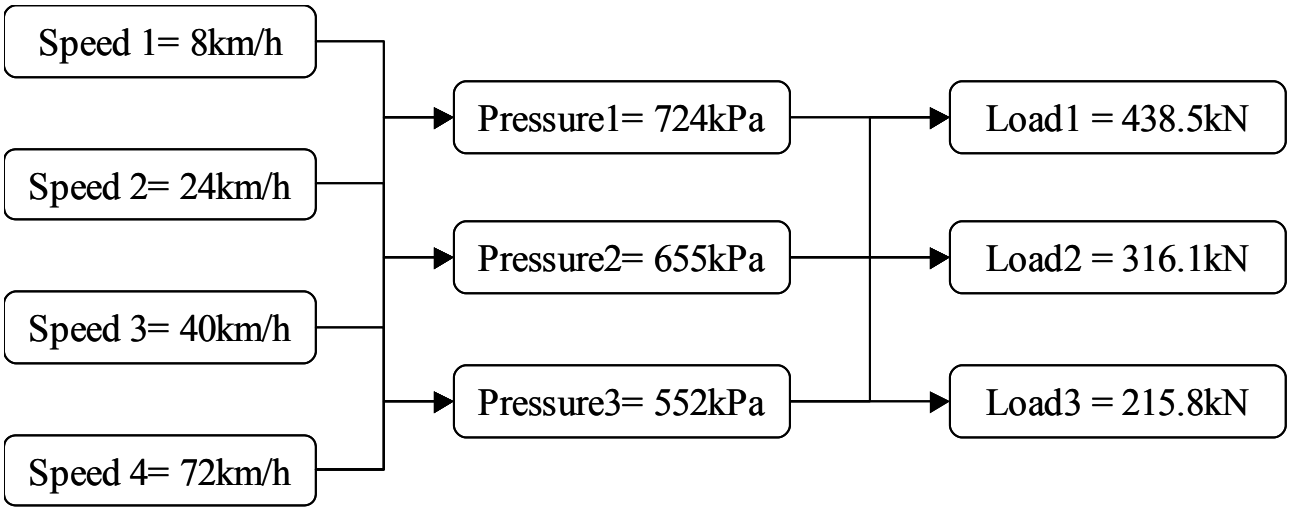

Figure 4-44. Matrix for the Truck Testing

4.6.7.2 Instrument Reponses to Vehicular Loading

Figure 4-45 represents typical strain signals measured on top of the mesh in Section I as the tire passes directly over the strain gauges (ISH2-2L and ISH1-5L). One may refer to Loulizi et al. (2001) for details on instrument identifications (Loulizi et al. 2001). It is obvious from these two typical signals that clear differences exist between the transverse and longitudinal directions, and that the classical assumptions of two-dimensional modeling of HMA responses (plane-strain conditions) do not hold true in real pavements.

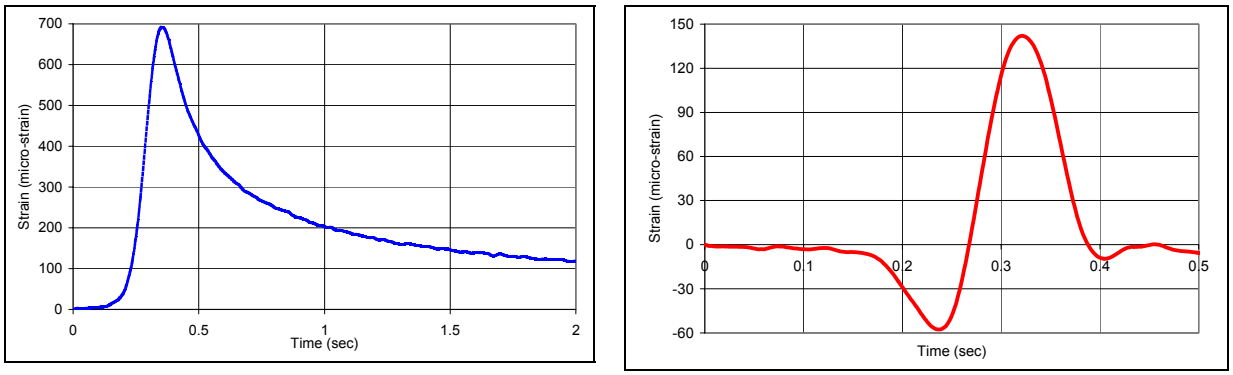

Transverse strain signal Longitudinal strain signal

Figure 4-45. Typical Transverse and Longitudinal Strain Signals in Section I

The main characteristics of the transverse and longitudinal directions can be summarized:

- These signals clearly prove the viscoelastic behavior of HMA: time retardation, relaxation with time, and asymmetry of the response.
- The longitudinal strain first shows compression, then tension, and finally compression again. The second compression peak is always lower than that of the first. As shown later, this occurs due to the friction condition at the interface. In the longitudinal direction, relaxation of the material is very fast and usually returns to zero with no permanent deformation.

- The longitudinal strain shape is not affected by the lateral position of the tire; however, the magnitude of the strain is affected by the position of the wheel. If the tire load passes directly on top of the strain gauge, the transverse strain exhibits pure tension. If a small offset between the tire and the gauge exists, the transverse gauge would exhibit pure compression. It appears that the relaxation process in the transverse direction is much slower.
- If a second load passes on top of the same gauge before complete relaxation, accumulation of strain may occur in the transverse direction due to the slow relaxation rate (resulting in permanent deformation, as shown in Figure 4-46). Relaxation becomes even slower at high temperatures, since under such conditions HMA may exhibit close to pure viscous behavior.

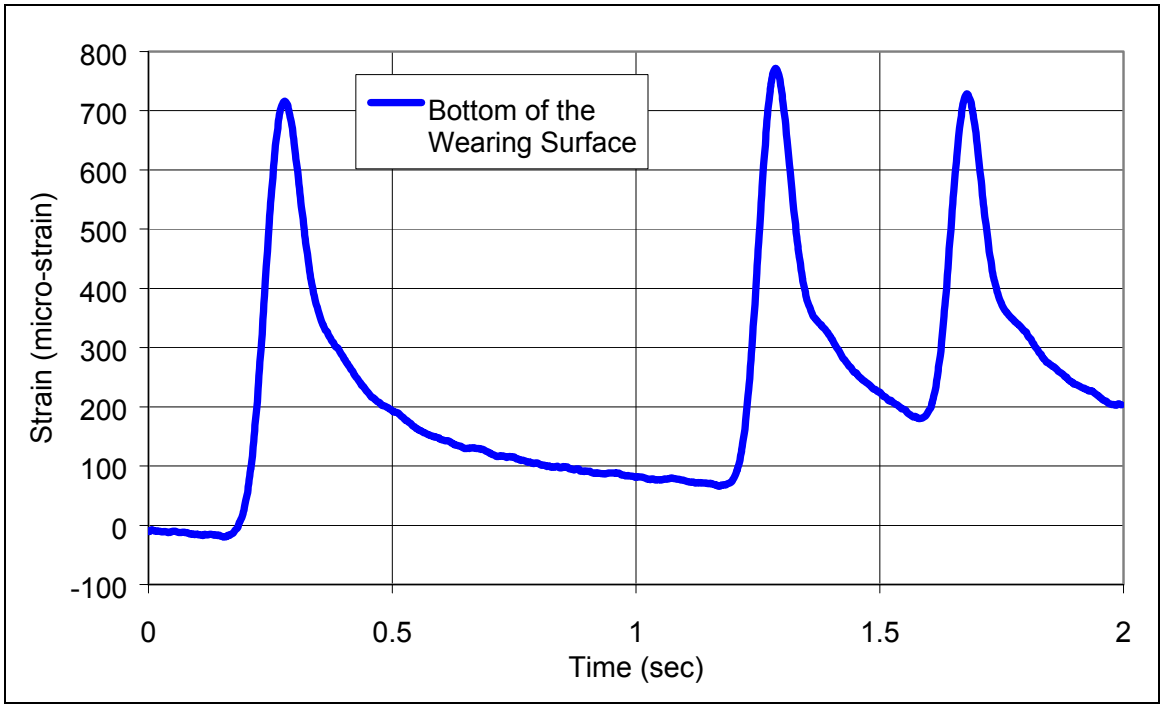

Figure 4-46. Accumulation of Strain in the Transverse Direction in Section L

- It was previously reported by Huhtala that the transverse strain is usually higher than the longitudinal strain, and, therefore, it is the most critical (Huhtala et al. 1992). The major trend in this project confirms such a conclusion.
- The difference in the material response in both directions is not directly related to the viscoelastic nature of HMA or the anisotropy of the material, but is instead due to the movement of the load in one direction rather than the other (Nilsson 1999).

A typical pressure cell response (IP5-2) is presented in Figure 4-47. This pressure cell is located at the bottom of the 21-A cement-treated layer in Section I.

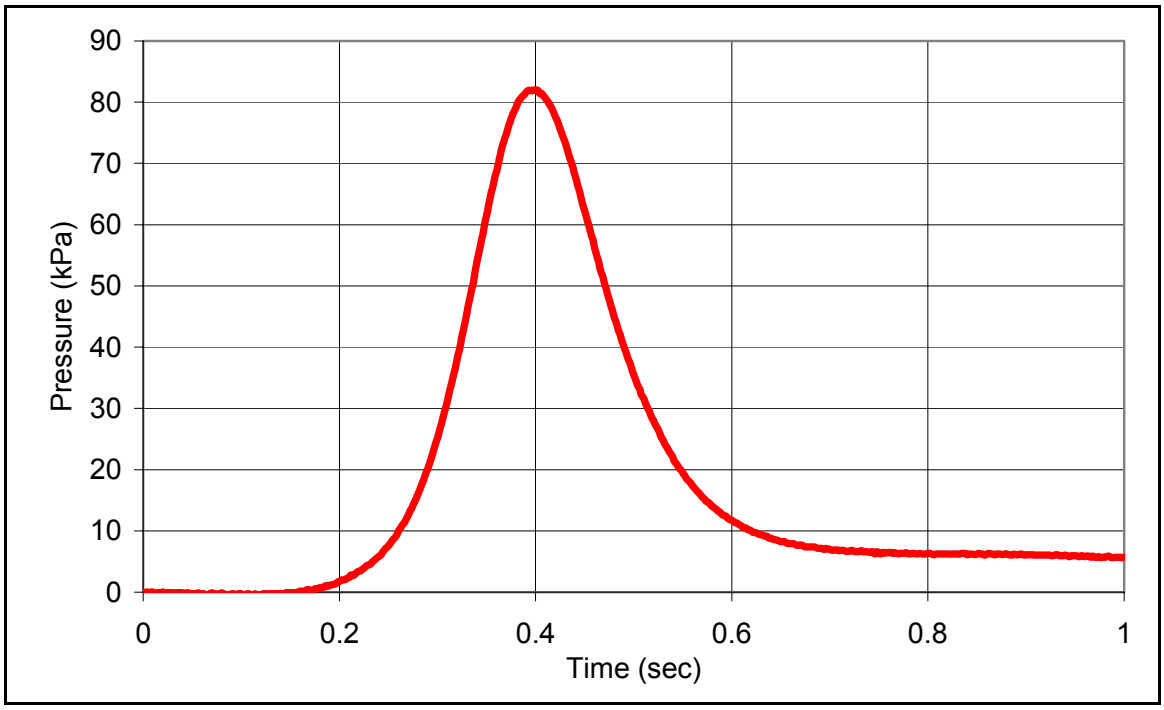

Figure 4-47. Typical Pressure Cell Response in Section I

As expected, only compression is measured in the vertical direction. The main characteristics of pressure cell signals can be summarized as follows:

- Due to the dynamic nature of the load, pressure cell response coincides with the vertical principal stress only when the wheel is exactly on top of the instrument.
- The width of the response depends mainly on the speed of the load. As shown in the strain responses, asymmetry of the signal is clearly manifested.
- The magnitude of the signal depends on the load and its lateral position. A lateral offset of more than 250mm usually results in a reduction of more than 50% in the gauge response at shallow depths.

4.6.7.3 Temperature and Speed Correction

A critical factor in strain and stress analysis is the temperature at the time of testing. As with any viscoelastic material, HMA's response to stress is dependent on both temperature and loading time. At high temperatures or under slow moving loads, the asphalt binder may exhibit close to pure viscous flow. However, at low surface temperature or under rapidly applied loading, the asphalt binder becomes progressively harder and, eventually, even brittle. Based on the collected data, effects of the temperature and speed have been quantified for all the sections at the Virginia Smart Road. For example, Figure 4-48 illustrates the variation of the measured strain with temperature in Section I.

As shown in this figure, the effect of temperature is significant, and correction of all collected data is essential if adequate comparison is sought. To adequately quantify and separate the effect of temperature from that of speed, a correction model was developed for each layer of interest. The variation of strain with temperature was found to be adequately described by an exponential relation having the following form:

$$\varepsilon = C_1 \exp(C_2 * T) \tag{4.3}$$

where

ε = strain at any temperature (micro-strain);

T = temperature (°C); and

C_1 and C_2 = constants to be determined from vehicular loading.

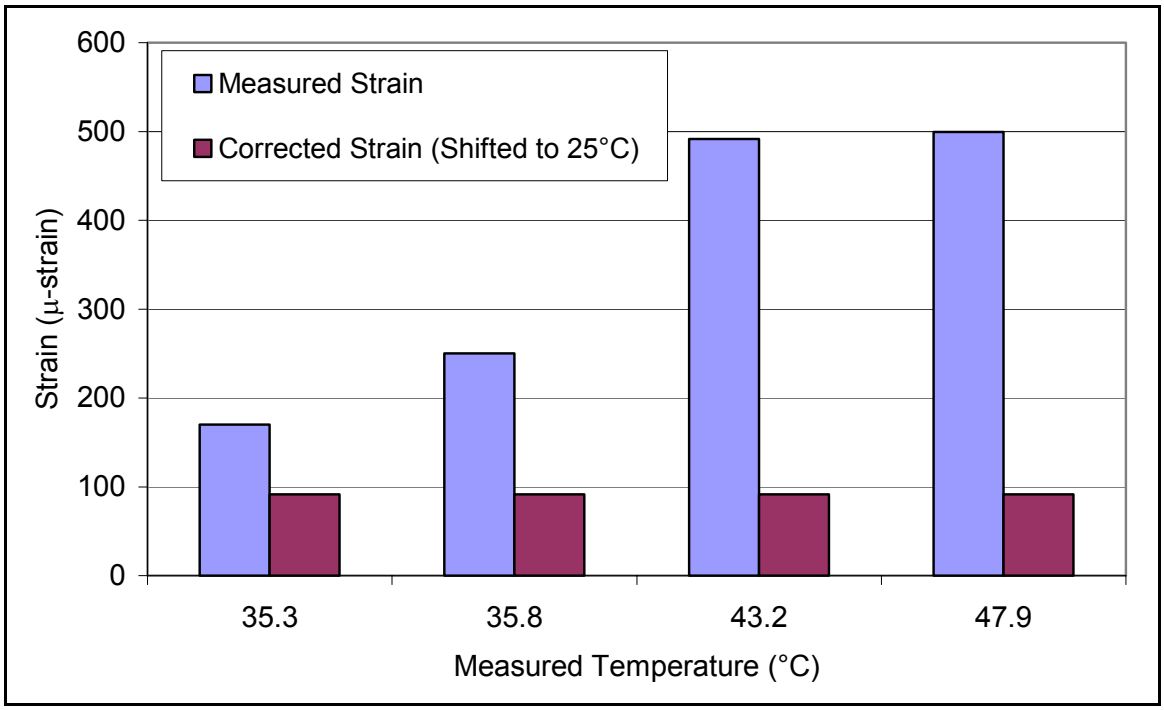

Figure 4-48. Effect of Temperature on the Strain Responses

To obtain the constants C1 and C2, a fitting regression analysis was conducted, which required a sufficient number of collected points (more details are presented in the following section). A typical outcome of this analysis is presented in Figure 4-49 (a) and (b) for sections I and L, respectively. These figures quantify speed and temperature effects on the strain measured at the bottom of the SM-9.5A layer in Section I and for the strain measured at the bottom of the wearing surface in Section L.

4.6.7.4 Model Validation and Calibration

Based on all measurements obtained during the truck testing program (from January 2000 to April 2002), various sets of instrument responses were selected to validate and calibrate the developed FE models. This step was essential for accurately calibrating the various parameters in the simulation process, so as to arrive at the best realistic

conditions with which to approach the real problem. It is important to realize that although analytical modeling allows a better handling of all variables, field performance is the only true indicator of mesh effectiveness. This truth, of course, highlights the importance of field trials to the validating and adjusting of theoretical models.

Results of the developed FE models for sections I and L were compared with actual stress and strain measurements at the Virginia Smart Road. It is important to emphasize that although an effort was made to approach real pavement conditions in the developed models, based on the available laboratory results and modeling limitations, some approximations and idealizations were inevitable.

Pavement responses to vehicular loading were compared at three temperatures (5, 25, and 40°C) at a speed of 8km/hr, with emphasis given to the upper HMA layers. Since not all the layers were instrumented for stress and strain responses, data from adjacent sections at the same depth and temperature were utilized. Although all the cases were simulated assuming viscoelastic properties for the HMA layers, a limited number of elastic cases were considered for comparison purposes.

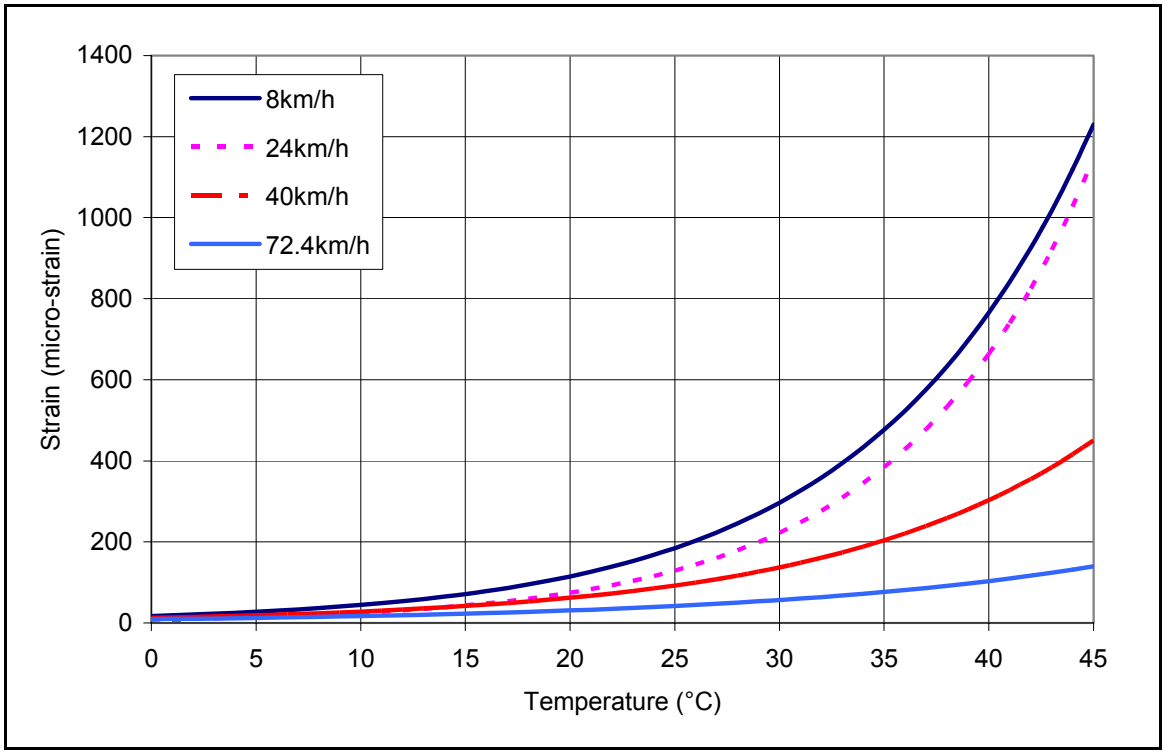

(a)

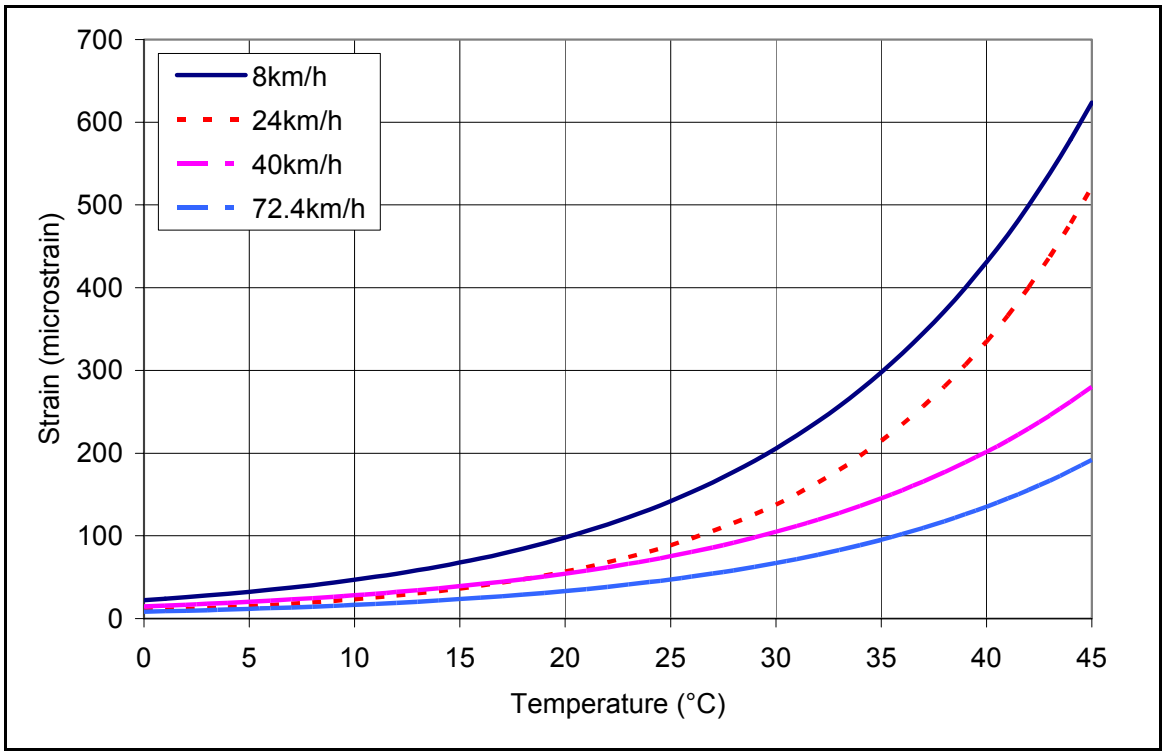

(b)

Figure 4-49. Variation of the Strain with Temperature and Speed in (a) Section I for SM-9.5A and (b) Section L for SMA-12.5

Figure 4-50 compares the measured and calculated vertical stresses at a temperature of 25°C under the wearing surface of Section L. Both the viscoelastic and elastic solutions are presented in this figure. There is a good agreement between the results of the FE models and the response of the pressure cell. Although both the elastic and viscoelastic solutions accurately fit the response in this case, the viscoelastic solution provided a slightly more accurate rendition of the pavement response.

Figure 4-51 illustrates a comparison at a temperature of 25°C between the measured and calculated vertical stresses at the bottom of the BM-25.0 in Section L. As shown in this figure, some discrepancies are observed between the measured and the calculated vertical stresses. Assuming that the measured vertical stress is the correct one, from it the viscoelastic solution deviates by 30% and the elastic solution by 63%. It should be noted, however, that other pressure cells may indicate that this response is

misleading or influenced by excessive pressure of the OGDL sharp aggregates on the sensitive side of the gauge.

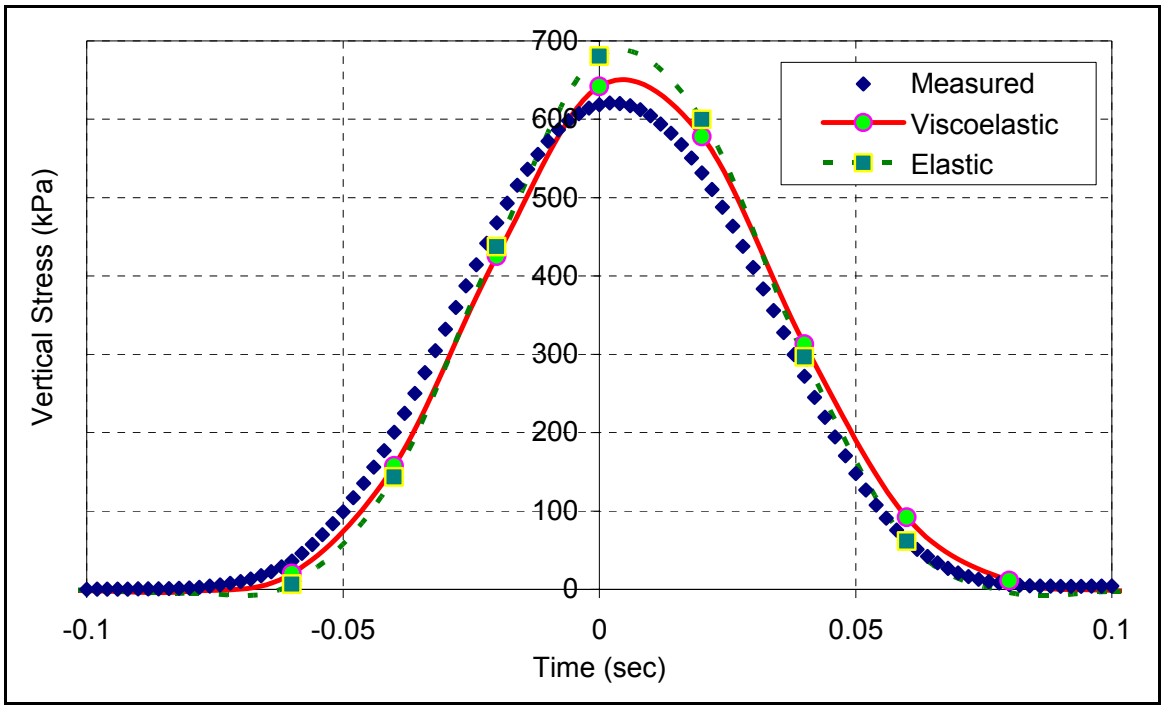

Figure 4-50. Measured and Calculated Vertical Stresses at the Bottom of the Wearing Surface (T=25°C)

Figure 4-52(a) illustrates a comparison between the measured and calculated longitudinal strains at a temperature of 25°C. As shown in this figure, only the viscoelastic solution provides an accurate simulation of the pavement responses. In this case, the elastic solution deviates from the measured strain by 56%. Figure 4-52(b) illustrates the same trend at a temperature of 40°C (no measured strains were available at the same temperature). It is clear from this analysis that the elastic solution grossly underestimates the measured strain and may lead to erroneous estimates of the pavement service lives. This finding was previously reported when measured strains were compared to the layered elastic solution (Loulizi et al. 2002).

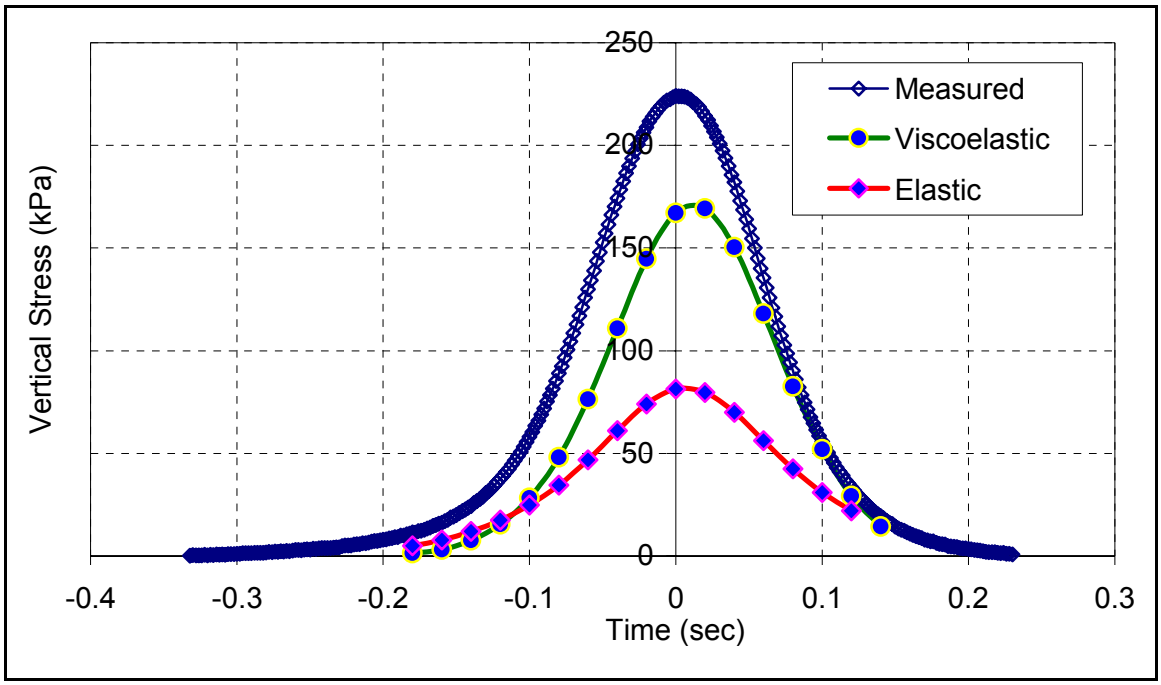

Figure 4-51. Measured and Calculated Vertical Stresses at the Bottom of the BM-25.0 (T=25°C)

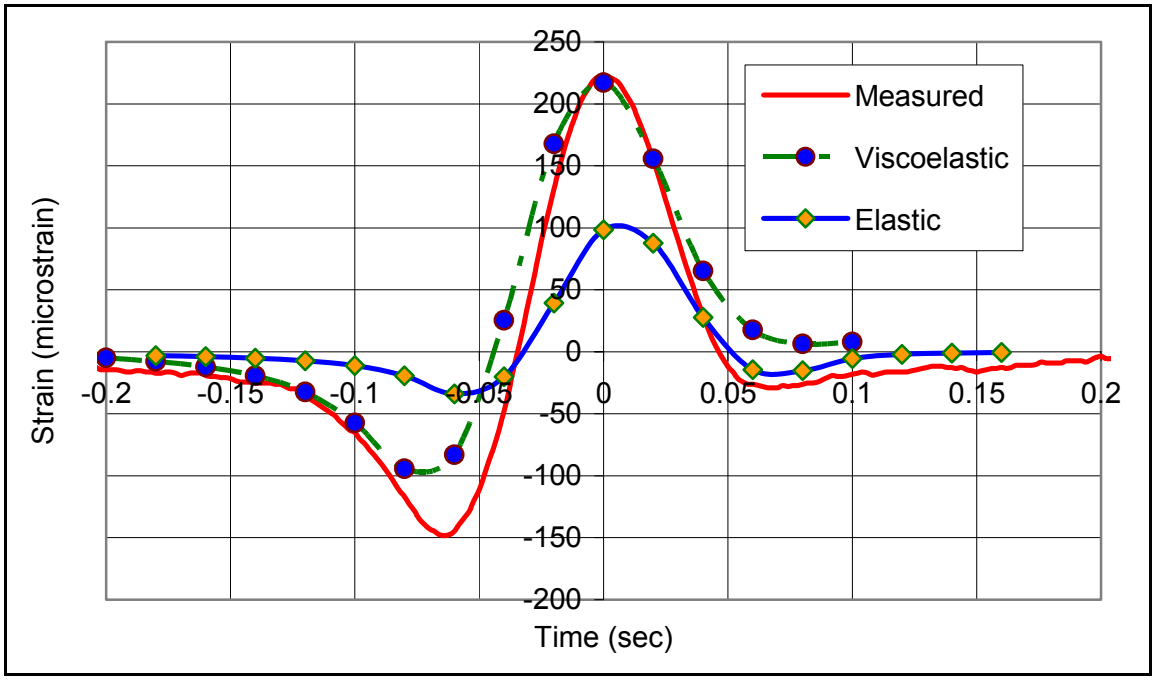

(a)

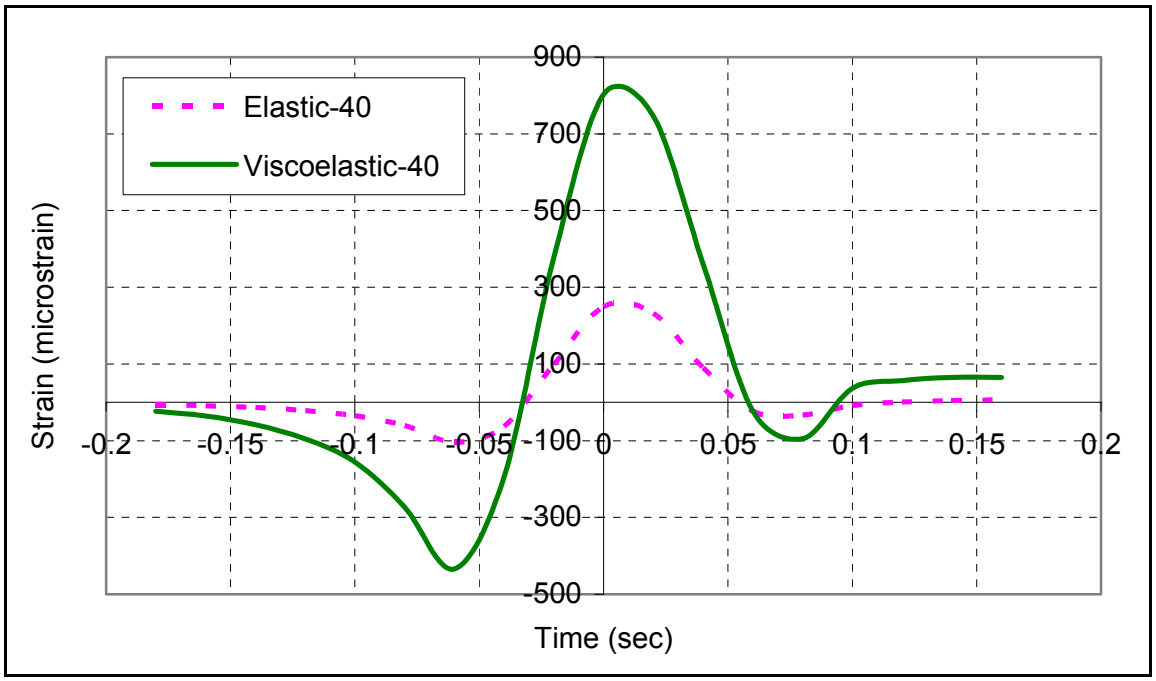

(b)

Figure 4-52. Comparison between Measured and Calculated Longitudinal Strains at the Bottom of the Wearing Surface at (a) 25°C and (b) 40°C

Figure 4-53(a) and (b) illustrate a comparison between the measured and calculated transverse strains, as well as the measured and calculated vertical stresses, at the bottom of the BM-25.0 in Section L. As this figure indicates, a better agreement is observed at low and intermediate temperatures.

4.6.7.5 Steel Reinforcement Effectiveness

The aforementioned observations suggest that the accuracy of the developed FE models in simulating vehicular loading is reasonable. Steel reinforcement effectiveness was investigated for the two types of reinforcement installed in sections I and L. The reinforcing pattern for the two mesh types is different, and may be easily identified from Table 4-2 and Figure 4-42.

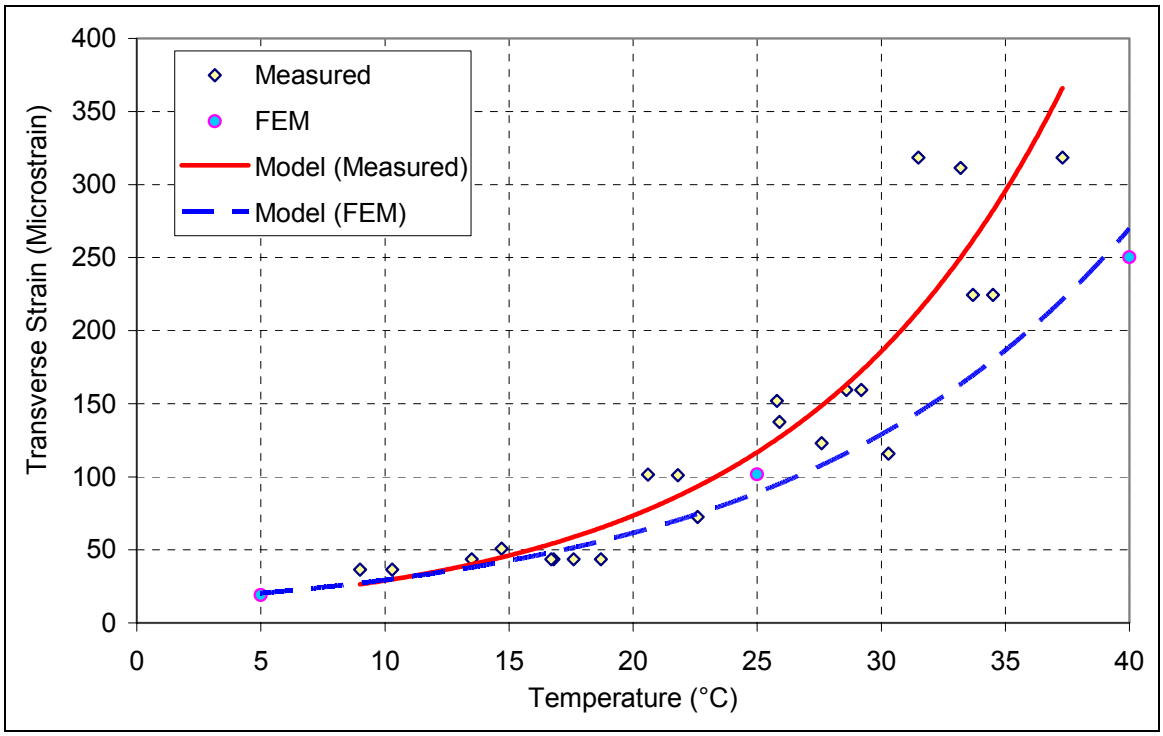

(a)

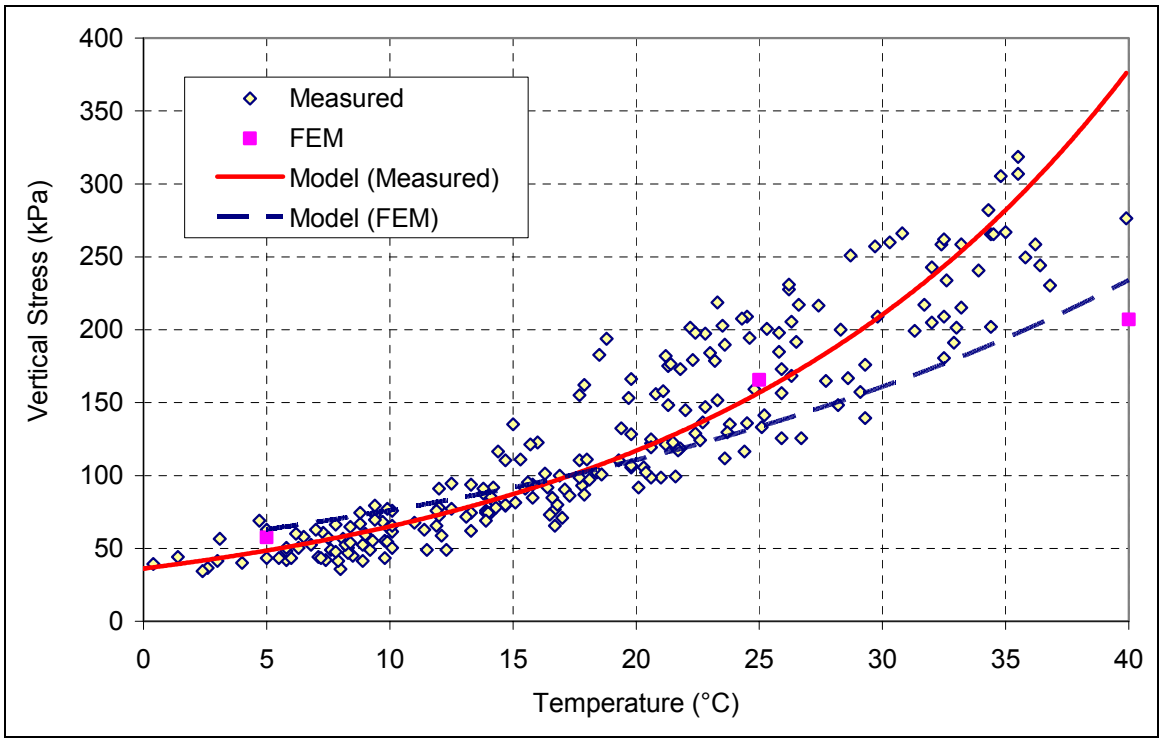

(b)

Figure 4-53. Comparison between the Measured and Calculated: (a) Transverse Strains and (b) Vertical Stresses at the Bottom of the BM-25.0 (section L)

Table 4-12 compares the reinforced and unreinforced cases at three temperatures: 5, 25, and 40°C. It should be emphasized that the material properties and loading patterns are identical in the reinforced and unreinforced cases, with the only difference between them the reinforcement.

Table 4-12. Comparison of Calculated Pavement Responses with and without Steel Reinforcement

(a) Section L

	Without Mesh				**With Mesh**			
Location	**Under SMA-12.5**				**Under SMA-12.5**			
Strain Temperature	E11	E22	E33	S33 (kPa)	E11	E22	E33	S33 (kPa)
5°C	26.6	33.5	-83.7	-601.7	26.6	33.5	-83.6	-601.8
25°C	252.7	217.1	-604.0	-641.8	252.2	215.9	-603.2	-642.1
40°C	816.4	958.8	-2536.0	-646.3	815.0	957.6	-2534.6	-646.5
Location	**Under BM-25.0**				**Under BM-25.0**			
Strain Temperature	E11	E22	E33	S33 (kPa)	E11	E22	E33	S33 (kPa)
5°C	19.5	22.1	-15.5	-55.2	19.2	20.8	-15.1	-57.5
25°C	106.7	114.4	-193.4	-167.1	101.6	97.9	-182.1	-165.6
40°C	280.5	318.7	-753.0	-213.2	250.3	272.6	-699.3	-206.9

(b) Section I

	Without Mesh				**With Mesh**			
Location	**Under SM-9.5A***				**Under SM-9.5A***			
Strain Temperature	E11	E22	E33	S33 (kPa)	E11	E22	E33	S33 (kPa)
5°C	25.1	29.3	-64.2	-606.5	25.0	29.2	-64.2	-606.4
25°C	174.5	141.4	-351.2	-620.5	173.9	141.0	-350.8	-620.7
40°C	674.3	750.8	-2059.1	-633.7	678.7	748.5	-2061.5	-634.4
Location	**Under BM-25.0**				**Under BM-25.0**			
Strain Temperature	E11	E22	E33	S33 (kPa)	E11	E22	E33	S33 (kPa)
5°C	26.7	29.3	-28.9	-220.6	26.7	29.1	-28.9	-222.2
25°C	147.6	137.1	-290.5	-308.9	145.9	135.4	-290.5	-311.4
40°C	489.1	517.9	-1192.5	-322.0	480.4	506.6	-1187.8	-325.0
Location	**Under SM-9.5A**				**Under SM-9.5A**			
Strain Temperature	E11	E22	E33	S33 (kPa)	E11	E22	E33	S33 (kPa)
5°C	13.9	15.0	-20.8	-177.0	13.3	14.5	-20.5	-176.8
25°C	94.5	88.6	-278.1	-282.9	75.7	70.8	-257.1	-280.5
40°C	282.9	299.0	-871.8	-287.2	203.1	213.9	-745.5	-281.5

Based on these results, the following observations can be made:

- Steel reinforcement causes a significant reduction in the calculated transverse and longitudinal strains. This reduction is quantified in terms of the number of cycles to initiate fatigue cracking at the bottom of the HMA layers.

- Steel reinforcement effectiveness in the early stage of the pavement service life (up to crack initiation phase) is pronounced at a shallow depth from the interlayer's location. In sections I and L, steel reinforcement was placed at the bottom of the base mix (BM-25.0). This means that if, due to poor bonding between the base and surface mixes, a crack starts at the bottom of the wearing surface, steel reinforcement will not be effective. Also, this improvement will not help in the case of top-down cracking.
- In Section L, steel reinforcement effectiveness appears more pronounced in the longitudinal (E22) than in the transverse strain (E11). Although the reinforcing bars are placed perpendicular to the traffic direction, the double wires are placed parallel to it; therefore, a more pronounced reduction is caused in the longitudinal strain. The frequency of the double wires per area is higher than the frequency of the reinforcing bars.
- In Section I, steel reinforcement effectiveness is equally pronounced in both longitudinal and transverse directions. The reinforcing bars for this product have a larger area and a more frequent pattern than the mesh used in Section L.
- The improvement provided by steel reinforcement is manifested primarily at intermediate and high temperatures. As previously explained, at high temperatures, HMA is weak and exhibits a viscous-like behavior. It is thought, however, that steel reinforcement effectiveness is not directly related to temperature, but rather to the actual stiffness of the pavement structure at a given temperature. The weaker the pavement structure, the more pronounced the steel reinforcement benefits to its performance.

To quantify the contribution of steel reinforcement to the early stages of a pavement's service life, as predicted by the results of the FE models, a classical fatigue law was adopted in this study (Mamlouk et al. 1991):

$$N = 9.33 \times 10^{-7} \varepsilon_t^{-3.84} \tag{4.22}$$

where

N = Number of cycles for crack initiation; and

ε_t = tensile strain at the bottom of the HMA layers.

This equation, which was adopted by the Arizona Department of Transportation (ADOT), was calibrated by the fatigue behavior of 20 selected experimental sites. It should be noted that although there is a large variation among fatigue equations for HMA materials, the previous equation was used relatively between the reinforced and the unreinforced cases. Figure 4-54 and Figure 4-55 illustrate the percentage of increase in the number of cycles needed to initiate fatigue cracks at the bottom of the HMA layers.

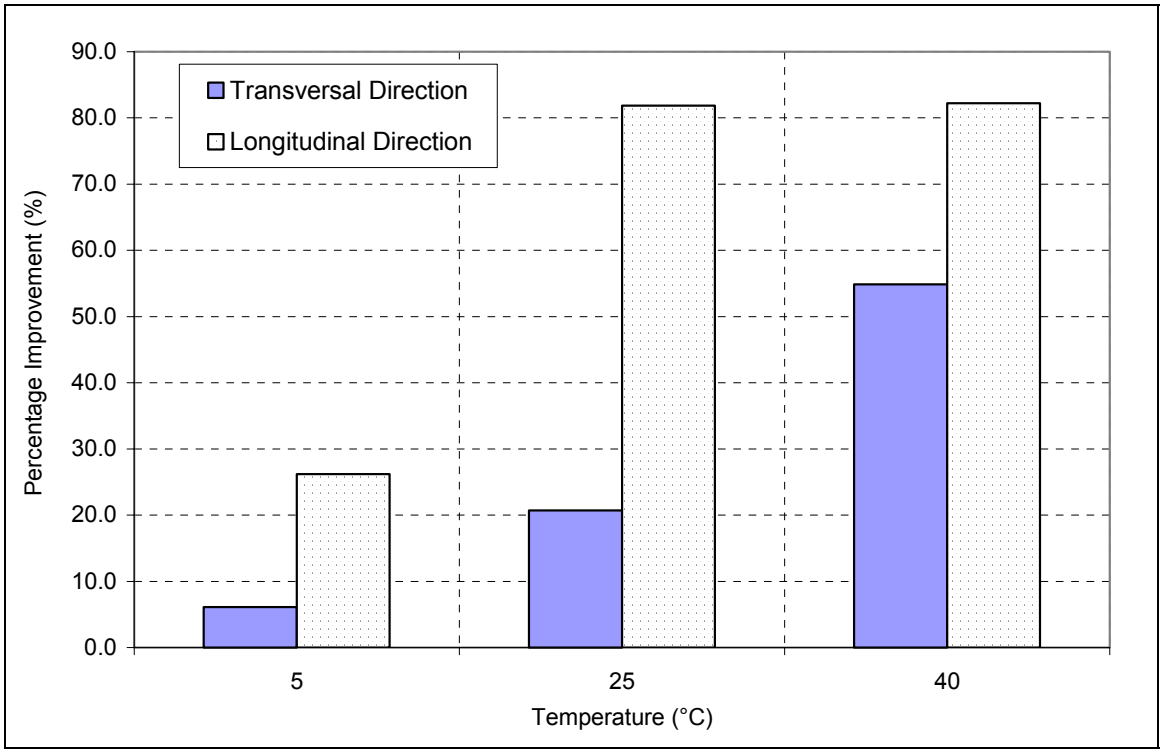

Figure 4-54. Percentage Improvement due to Steel Reinforcement (Section L)

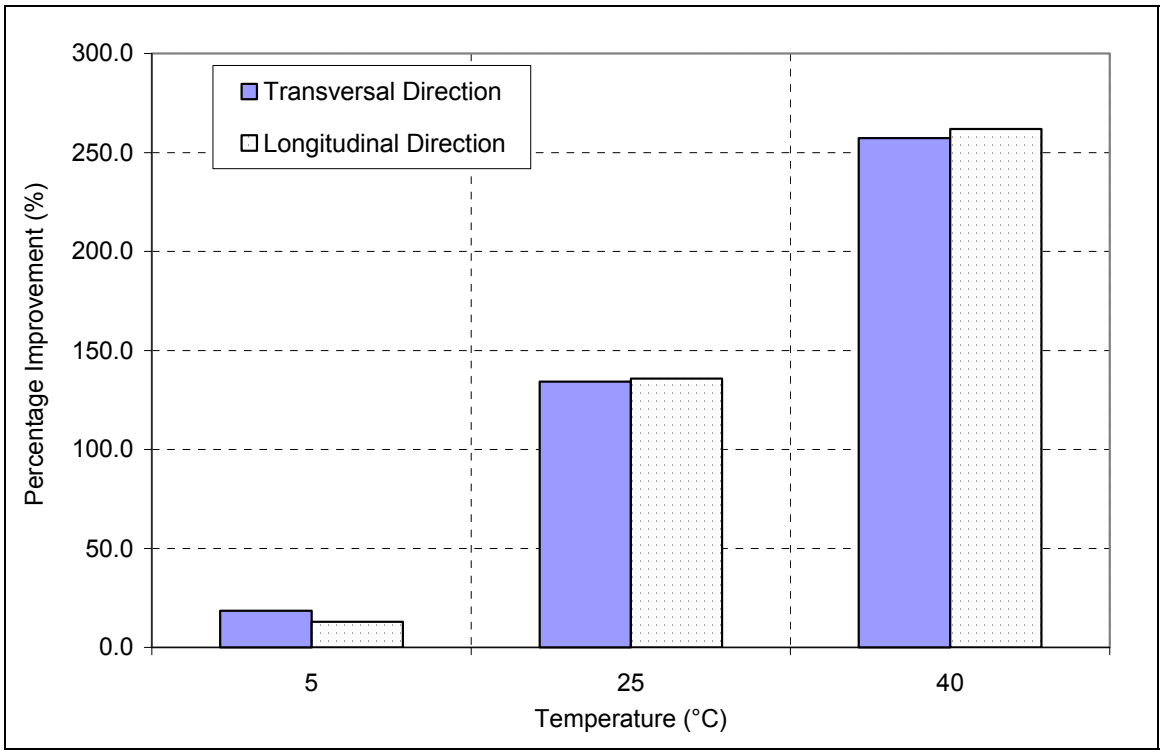

Figure 4-55. Percentage Improvement due to Steel Reinforcement (Section I)

As shown in these figures, steel reinforcement is pronounced at intermediate and high temperatures. In Section L, the percentage of improvement for the considered pavement structure ranges between 6 and 55% in the transverse direction, and between 25 and 82% in the longitudinal direction. In Section I, the percentage of improvement for the considered pavement structure ranges between 15 and 257% in the transverse direction, and between 12 and 261% in the longitudinal direction. The use of a viscoelastic approach in the modeling process provided a range of contribution, depending on the considered temperature. Although this permitted some insight into the effect of temperature on the mesh contributing mechanism, the exact percentage of improvement can be easily obtained if one assumes a representative temperature for the considered project location.

4.7 DISCUSSION

Results of FE analysis may be used to explain the mechanisms by which steel reinforcement contributes to new pavement systems. Based on these results, the contribution of steel reinforcement to new pavement systems can be divided into three distinct phases (see Figure 4-56):

- **Stage 1**: This is the phase investigated by this study, which is currently experienced at the Virginia Smart Road (point A in Figure 4-56). As shown in this study, the contribution of steel reinforcement to this phase is significant, and the interlayer will cause a reduction in the rate of fatigue of the HMA materials.
- **Stage 2**: In this phase, after sufficient load repetitions, HMA is fatigued and can no longer withstand applied loads without initiating a crack or cracks at the bottom of the layer (point B in Figure 4-56). This is the area of maximum tensile stresses; it is, therefore, the location with the highest probability of crack initiation. This hypothetical phase is expected to occur in any pavement structure. It is virtually impossible, however, to accurately determine if steel reinforcement can prevent the crack initiation mechanism in HMA. However and as previously shown, the contribution of steel reinforcement was quantified through an increase in the number of cycles for crack initiation as defined by classical fatigue equations. It was shown that for the considered pavement structures, the percentage of improvement ranges between 6 and 257% in the transverse direction and between 12 and 261% in the longitudinal direction. This contribution was more pronounced at intermediate and high temperatures.
- **Stage 3**: In this phase, the HMA is fractured and unable to withstand applied loading repetitions without further propagation of the crack. This problem becomes similar to a reflective cracking situation, in which a crack is established in a layer, and excessive energy at the crack tip causes its propagation. It should be noted, however, that the location of the interlayer system with respect to the crack is different, since in this case the crack will initiate on top of it. In this stage, steel reinforcement delays the propagation of the crack, similar to the

effects of steel-reinforced concrete. Hot-mix asphalt and steel reinforcement will then act together to prevent further deterioration of the pavement layer.

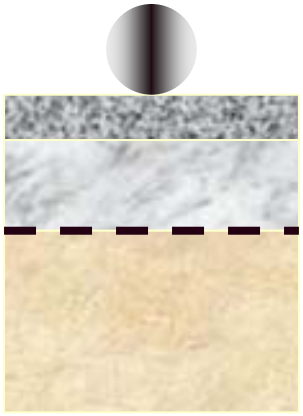

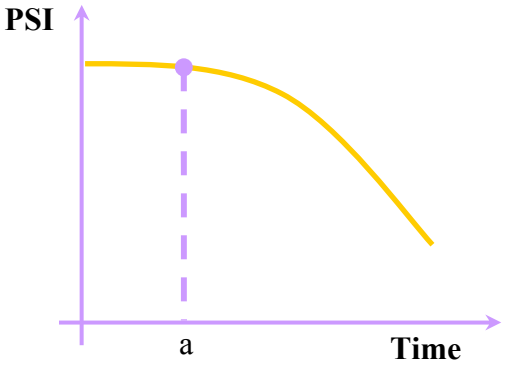

STAGE 1

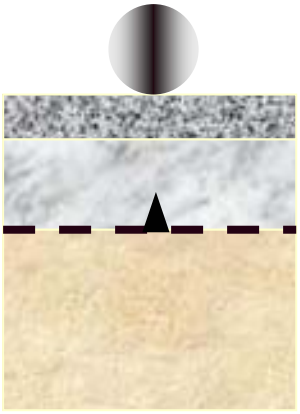

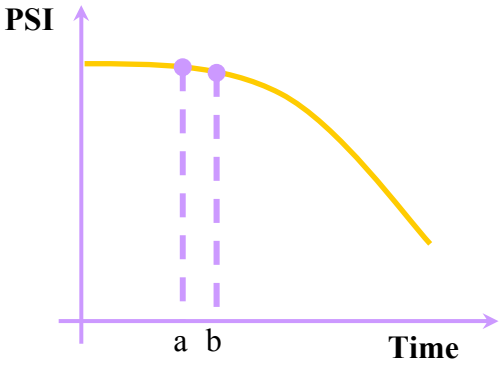

STAGE 2: Crack Initiation

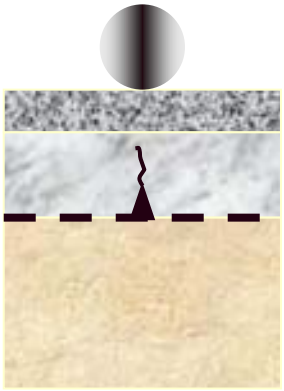

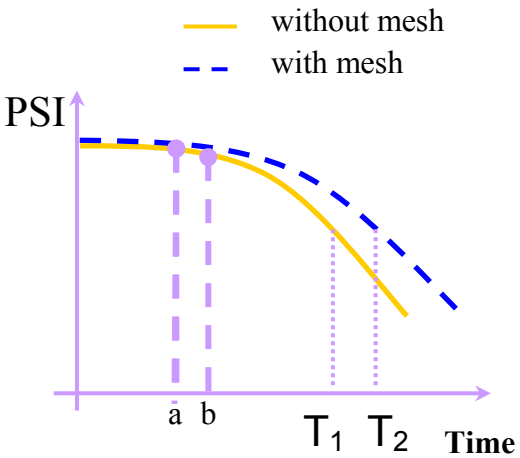

STAGE 3: Crack Propagation

Figure 4-56. Phases of Pavement Deterioration

4.8 FINDINGS AND CONCLUSIONS

Based on experimental and theoretical evaluations, the use of steel reinforcement in new flexible pavement systems was found effective. As a result of this study, the following conclusions can be drawn:

- Installation of steel reinforcement is crucial for achieving adequate performance. For successful installation, mesh should be laid perfectly flat and folds or wrinkles should be avoided. Strong bonding of the interlayer to the upper layer is the key to good performance, since the effectiveness of the reinforcement mainly depends on whether the straining actions in the HMA can be transferred to the steel reinforcement. Installation of steel reinforcement in this project was successful and is thought to be more easily accomplished than with other interlayer systems. The reinforcing mesh may be fixed using two approaches: nailing or slurry sealing. In general, based on the reviewed literature and the experience gleaned from this project, applying an intermediate layer has proven more reliable than nailing.
- Based on FWD and FE simulation of this testing, it can be concluded that for the considered pavement structures the contribution of steel reinforcement to surface vertical deflections is minimal.
- Finite element models were successfully developed to simulate the pavement designs in sections I and L at the Virginia Smart Road. After successful calibration of these models based on instrument responses to vehicular loading, a theoretical comparison was established between unreinforced and reinforced cases. In Section L, the percentage of improvement for the considered pavement structure ranges between 6 and 55% in the transverse direction and between 25 and 82% in the longitudinal direction. In Section I, the percentage of improvement for the considered pavement structure ranges between 15 and 257% in the transverse direction and between 12 and 261% in the longitudinal direction. It is important to emphasize that, since two different pavement designs were used

at different locations in the systems, no comparison was established between the two types of steel reinforcement.

- After initiation of cracking, the contribution of steel reinforcement to the pavement structure is significant. Similar to steel-reinforced concrete, it delays the rate at which the crack is propagated in the pavement surface. This phase is discussed in detail in the following chapter, which focuses on the use of steel reinforcement in pavement rehabilitation applications.

4.9 REFERENCES

"ABAQUS, Finite Element Computer Program." (1998). Version 5.8, Hibbitt, Karlsson and Sorensen, Inc, MI.

Boussinesq, J. (1885). "Application des potentials a l'etude de l'equilibre et du movement des solids elastiques." Gauthier-Villars, Paris.

Brademeyer, B. (1988). "VESYS modification." Final Report DTFH61-87-P00441 to FHWA.

Brownridge, F. C. (1964). "An evaluation of continuous wire mesh reinforcement in bituminous resurfacing." *Proc., Annual Meeting of the Association of Asphalt Paving Technologists*, Vol. 33, Dallas, TX, 459-501.

Burmister, D. M. (1943). "The theory of stresses and displacements in layered systems and applications to the design of airport runways." *Highway Research Board*, Vol. 23, 126-144.

Burmister, D. M. (1945). "The general theory of stresses and displacements in layered soil systems." *Journal of Applied Physics*, Vol. 16, 84-94, 126-127, 296-302.

Chatti, K., Kim, H. B., Yun, K. K., Mahoney, J. P., and Monismith, C. L. (1996). "Field investigation into effects of vehicle speed and tire pressure on asphalt concrete pavement strains." *Transportation Research Record 1539*, Transportation Research Board, Washington, D.C., 66-71.

Cho, Y., McCullough, B. F., and Weissmann, J. (1996). "Considerations on finite-element method application in pavement structural analysis." *Transportation Research Record 1539*, Transportation Research Board, Washington, D.C., 96-101.

De Beer, M., Fisher, C., and Jooste, F. J. (1997). "Determination of pneumatic tyre/pavement interface contact stresses under moving loads and some effects on pavements with thin asphalt surfacing layers." *Proc., Eighth International Conference on Asphalt Pavements*, Seattle, WA, Vol. 1, 179-227.

De Jong, D. L., Peatz, M. G. F., and Korswagen, A. R. (1973). "Computer program Bisar layered systems under normal and tangential loads." Konin Klijke Shell-Laboratorium, Amsterdam, External Report AMSR.0006.73.

Desai, C. S. (1979). *Elementary finite element method*, Prentice-Hall, N.J.

Harichandran, R. S., C. M. Ramon, T. Mahmood, and Baladi, G. Y. (1994). "MICHBACK User's Manual." *Michigan Department of Transportation*, MI, Lansing.

Hua, J. (2000). "Finite element modeling and analysis of accelerated pavement testing devices and rutting phenomenon." PhD thesis, Purdue University, West Lafayette, IN.

Huang, Y. H. (1993). *Pavement analysis and design*, 1st ed., Prentice Hall, NJ.

Huang, B., Mohammad, L. N., and Rasoulian, M. (2001). "Three-dimensional numerical simulation of asphalt pavement at Louisiana accelerated loading facility." *Journal of the Transportation Research Board 1764*, Transportation Research Board, Washington, D.C., 44-58.

Hugo, F., and Schreuder, W. J. (1993). "Effect of sample length on indirect tensile test parameters." *Proc., Annual Meeting of the Association of Asphalt Paving Technologists*, Vol. 62, 422-449.

Huhtala, M., and Pihlajamaki, J. (1992). "Strain and stress measurements in pavements." *Proc., Conference Sponsored by the U.S. Army Cold Regions Research and*

Engineering Laboratory - Road and airport pavement response monitoring systems, Federal Aviation Administration, West Lebanon, New Hampshire, American Society of Civil Engineers, 229-243.

Kennepohl, G., Kamel, N., Walls, J., and Hass, R. C. (1985). "Geogrid reinforcement of flexible pavements design basis and field trials." *Proc., Annual Meeting of the Association of Asphalt Paving Technologists*, Vol. 54, San Antonio, TX, 45-75.

Kim, J., and Hjelmstad, K. (2000). "Three-dimensional finite element analysis of multi-layered systems: Compressive nonlinear analysis of rigid airport pavement systems." *Center of Excellence for Airport Pavement Research*, COE Report No. 10, Department of Civil Engineering, University of Illinois at Urban-Champaign, Urbana, IL.

Kim, Y. R., Daniel, J. S., and Wen, H. (2002). "Fatigue performance evaluation of WesTrack asphalt mixtures using viscoelastic continuum damage approach." Final Report No. FHWA/NC/2002-004, North Carolina Department of Transportation.

Kopperman, S., Tiller, G., and Tseng, M. (1986). "ELSYM5, Interactive microcomputer version." User's Manual, Report No. FHWA-TS-87-206, Federal Highway Administration.

Loulizi, A., Al-Qadi, I. L., Lahouar, S., Flinstch, G. W., and Freeman, T. E. (2001). "Data collection and management of the instrumented Smart Road flexible pavement sections." *Journal of the Transportation Research Record 1769*, Transportation Research Board, Washington, D.C., 142-151.

Loulizi, A., Al-Qadi, I. L., Flintsch, G. W., and Freeman, T. E. (2002). "Using field measured stresses and strains to quantify flexible pavement responses to loading." *Proc., Ninth International Conference on Asphalt Pavements*, Copenhagen, Denmark, Vol. 1, 179-227.

Mamlouk, S. M., Zaniewski, J. P., and Houston, S. L. (1991). "Overlay design method for flexible pavements in Arizona." *Transportation Research Record 1286*, Transportation Research Board, Washington, D.C., 112-122.

Nilsson, R. (1999). "A viscoelastic approach to flexible pavement design." PhD thesis, Dept. of Infrastructure and Planning, Royal Institute of Technology, Sweden.

"MSC/PATRAN, Analysis Software System." (2001). Version 2001, MacNeal-Schwendler Corporation, Santa Ana, CA.

Raad, G., and Figueroa, J. L. (1980). "Load response of transportation support systems." *Journal of Transportation Engineering*, ASCE, Vol. 106, 111-128.

Rada, G. R., Richter, C. A., and Jordahl, P. (1994). "SHRP's layer moduli backcalculation procedure." *Nondestructive Testing of Pavements and Backcalculation of Moduli*, ASTM STP 1198, Harold L. Von Qunitas, Albert J. Bush, III, and Gilbert Y. Baladi, Eds, American Society for Testing and Materials, Philadelphia, 38-52.

Rigo, J. M. (1993). "General introduction, main conclusions of 1989 conference on reflective cracking in pavements, and future prospects." *Proc., 2nd International RILEM Conference – Reflective Cracking in Pavements*, E & FN Spon, Liege, Belgium, 3-20.

Romanoschi, S. A., and Metcalf, J. B. (2001). "Characterization of asphalt concrete layer interfaces." *Journal of the Transportation Research Board 1778*, Transportation Research Board, Washington, D.C., 132-139.

Shoukry, S. N., and William, G. W. (1999). "Performance evaluation of backcalculation algorithms through three-dimensional finite-element modeling of pavement

structures." *Transportation Research Record 1655*, Transportation Research Board, Washington, D.C., 152-160.

Tons, E., Bone, A. J., and Roggeveen, V. J. (1961). "Five-year performance of welded wire fabric in bituminous resurfacing." *Highway Research Board Bulletin 290*, Washington, D.C., 43 -80.

Uddin, W., Zhang, D., and Fernandez, F. (1994). "Finite element simulation of pavement discontinuities and dynamic load response." *Transportation Research Record 1448*, Transportation Research Board, Washington, D.C., 100-106.

Ullidtz, P. (1987). *Pavement analysis*, Elsevier Science, New York, NY.

Vanelstraete, A., and Francken, L. (2000). "On site behavior of interface systems." *Proc., 4th International RILEM Conference – Reflective Cracking in Pavements*, E & FN Spon, Ontario, Canada, 517-526.

Wardle, L. J., and Rodway, B. (1998). "Layered-elastic pavement design-recent developments." *Proc., Transport 1998, 19th ARRB Conference*, Sydney, Australia.

White, T. D. (1998). "Application of finite element analysis to pavement problems." *Proc., First National Symposium on 3D Finite Element Modeling for Pavement Analysis and Design*, Charleston, WV, 52-84.

Zaghloul, S. and White, T. (1993). "Use of a three-dimensional, dynamic finite element program for analysis of flexible pavement." *Transportation Research Record 1388*, Transportation Research Board, Washington, D.C., 60-69.

Zhang, W., Drescher, A., and Newcomb, D. E. (1997). “Viscoelastic behavior of asphalt concrete in diametral compression.” *Journal of Transportation Engineering*, American Society of Civil Engineers, Vol. 123, No. 6, 495-502.